NASA
TP
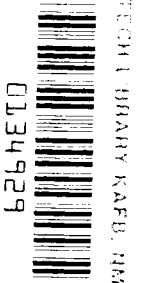2103
c.1

Calculations of Inviscid Flow Over Shuttle-Like Vehicles at High Angles of Attack and Comparisons With Experimental Data

K. James Weilmuenster
and H. Harris Hamilton II
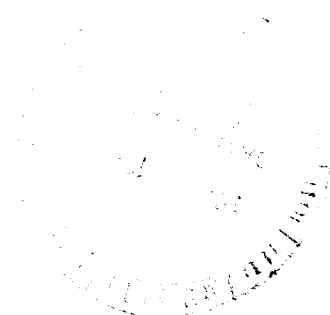
Calculations of Inviscid Flow Over Shuttle-Like Vehicles at High Angles of Attack and Comparisons With Experimental Data

K. James Weilmuenster
and H. Harris Hamilton II
Langley Research Center
Hampton, Virginia

CONTENTS

INTRODUCTION

Advances in computational techniques and computers in the past few years make it practical to compute the steady inviscid flow field about complex three-dimensional bodies, such as the Space Shuttle orbiter or other advanced entry vehicles, in their actual supersonic or hypersonic flight environment. The inviscid flow field provides surface pressures, which can be integrated to obtain aerodynamic loads, and other flow properties which are required to calculate surface heating rates (ref. 1) needed to define the thermal environment.

These vehicles enter the atmosphere at relatively large angles of attack which will lead to one of two classes of problems. (See fig. 1.) If the angle of attack is moderate (25° to 35° for Shuttle-like vehicles), the subsonic portion of the flow field is generally confined to the vehicle nose. Several papers (refs. 2 to 5) have presented time-asymptotic methods of efficiently solving the three-dimensional invis-cid flow over blunt-nosed bodies at moderate angle of attack where the subsonic region is relatively small. These solutions provide a data surface, downstream of the subsonic region, on which the local flow velocity is supersonic. Several papers (refs. 6 to 9) have presented methods for continuing the solution downstream in the supersonic region by using spatial marching techniques. Since these techniques use spatial marching, they require relatively low computer storage. These methods have been shown to provide good results unless additional embedded pockets of subsonic flow are encountered (such as near the leading edge of wings) where the spatial marching techniques break down.

When the angle of attack is large (greater than 35°), the subsonic region is no longer confined to the nose but extends much farther downstream and can envelop much of the lower surface. (See fig. 1.) Since the entire subsonic region must be com-puted simultaneously, the time-asymptotic portion of the solution will require many more grid points than required for the moderate angle-of-attack case discussed pre-viously. Therefore, codes must be structured for computers that have the storage and computational speed required to solve this type of problem (which may require 90 000 or more grid points). Thus, existing time-asymptotic methods (refs. 2 to 5), either because they are constructed for scalar computation or because of the coordinate system used in the code, are not suited to solve the flow over complete vehicles with complex three-dimensional geometries at high angle of attack. In reference 10, it is shown that a vector-processing computer is ideally suited for solving this type of large flow-field problem.

The present paper presents a time-asymptotic method that is being developed for the CDC® CYBER 203 vector-processing computer which will be able to solve the flow over complex three-dimensional bodies (Shuttle-like geometries at large angle of attack) where large embedded subsonic regions occur. Results are presented in this paper which demonstrate the capability of the code HALIS (High Alpha Inviscid Solution) to compute the flow field over the Space Shuttle orbiter at large angles of attack. Additional applications of the HALIS code may be found in reference 11 for comparisons with Shuttle tunnel data and reference 12 for comparison with Shuttle flight data. The components of the Euler equations as well as the development of the transformed equations in both the spherical and cylindrical coordinate systems are presented in appendix A. The Euler equations in the spherical coordinate system along the ray $\theta = \pi$ are given in appendix B. A stability analysis is presented in

appendix C by M. J. Hamilton. The method for determining the shock velocity and other flow properties at the shock wave is outlined in appendix D.

SYMBOLS

a	local speed of sound, $\tilde{a}/U_\infty$
C_p	pressure coefficient
E	total energy, $\tilde{E}/U_\infty^2$
e	internal energy, $\tilde{e}/U_\infty^2$
f	dummy variable used in generalized description of derivative forms
H	total enthalpy, $\tilde{H}/U_\infty^2$
h	static enthalpy, $\tilde{h}/U_\infty^2$
L	total length of vehicle, 1290 inches to hinge line
L_o	reference length, ft
M	Mach number
n_b	outer unit normal to body
n_s	outer unit normal to shock
p	pressure, $\tilde{p}/\tilde{\rho}_\infty U_\infty^2$
R	gas constant, ft^2/sec^2-°R
r	cylindrical coordinate, in.
$\bar{r}$	spherical coordinate, in.
S	entropy, $\tilde{S}/R$
$\bar{\bar{T}}$	vector defined by equation (11)
t	time, $\tilde{t}/(L_o/U_\infty)$
U	velocity, ft/sec
u_r	r-velocity component, $\tilde{u}_r/U_\infty$
$u_{\bar{r}}$	$\bar{r}$-velocity component, $\tilde{u}_{\bar{r}}/U_\infty$
u_z	z-velocity component, $\tilde{u}_z/U_\infty$
u_θ	θ-velocity component, $\tilde{u}_\theta/U_\infty$
u_ϕ	ϕ-velocity component, $\tilde{u}_\phi/U_\infty$

2

$u_{\bar{\phi}}$	$\bar{\phi}$-velocity component, $\tilde{u}_{\bar{\phi}}/U_\infty$

$u_{\bar{\phi}}$ $\bar{\phi}$-velocity component, $\tilde{u}_{\bar{\phi}}/U_\infty$

v total velocity vector, $\tilde{v}/U_\infty$

v_s shock velocity, $\tilde{v}_s/U_\infty$

W,F,G,H,Q vectors defined in equations (A8)

$\bar{W},\bar{F},\bar{G},\bar{H},\bar{Q}$ vectors defined in equations (A2)

$\bar{\bar{W}},\bar{\bar{F}},\bar{\bar{G}},\bar{\bar{S}},\bar{\bar{Q}}$ vectors defined in equations (B4)

z cylindrical coordinate

α angle of attack, deg

Γ distance between body and shock, defined in figure 7

γ ratio of specific heats

ε smoothing coefficient

η transformed cylindrical coordinate, equations (A9)

$\bar{\eta}$ transformed spherical coordinate, equations (A3)

θ spherical coordinate

ξ transformed cylindrical coordinate, equations (A9)

ρ density, $\tilde{\rho}/\tilde{\rho}_\infty$

ϕ cylindrical coordinate

$\bar{\phi}$ spherical coordinate

ψ transformed cylindrical coordinate, equations (A9)

$\bar{\psi}$ transformed spherical coordinate, equations (A3)

ω transformed spherical coordinate, equations (A3)

Subscripts:

b body surface

max   maximum

s shock surface

w wall surface

∞ free-stream conditions

3

Notation over symbols:

~   dimensional variable

→   vector

^   unit vector

−   spherical coordinate system

= $\bar{\phi} = \pi$ plane in spherical coordinate system

COORDINATE SYSTEMS

The method of solution presented in this report requires that the outer boundary of the solution space correspond to the bow shock which envelops the entire vehicle and that the inner boundary correspond to the vehicle surface. Also, it is required that all coordinate lines extending between the body surface and the shock intersect the body surface only one time. When the vehicle to be represented is a short blunt body, a spherical coordinate system naturally satisfies these requirements. However, when the body is blunt and many nose radii in length, the use of a spherical coordinate system would result in a highly skewed physical grid. In order to avoid this problem and still satisfy these grid requirements, the physical grid is constructed by combining a spherical with a cylindrical coordinate system. Such a combined coordinate system is shown in figure 2. In this right-hand system, the spherical and cylindrical coordinate system are coupled at the plane $\theta = \pi/2$, $z = 0$ where the two systems are coincident.

In the physical domain, computations are made in the spherical system over

$$\left. \begin{array}{c} \bar{r}_b < \bar{r} < \bar{r}_s \\[2mm] \dfrac{-\pi}{2} < \bar{\phi} < \dfrac{\pi}{2} \\[2mm] \dfrac{\pi}{2} < \theta < \pi \end{array} \right\} \tag{1}$$

and in the cylindrical system over

$$\left. \begin{array}{c} r_b < r < r_s \\[2mm] \dfrac{-\pi}{2} < \phi < \dfrac{\pi}{2} \\[2mm] 0 < z < z_{max} \end{array} \right\} \tag{2}$$

A typical representation of this physical grid system is shown in figure 3(a), a symmetry-plane view, and in figure 3(b), a cross-flow-plane view which corresponds to

4

the exit plane of figure 3(a). In order to improve the clarity of these two figures, a number of grid lines have been removed. As can be seen, the physical coordinate system is skewed and nonorthogonal.

GEOMETRY DESCRIPTION

The vehicle configurations used for making flow-field calculations with the present code are first modeled with QUICK - a geometry program described in reference 13. This model provides a smooth analytic description of the vehicle geometry in a "local polar coordinate system," $r_b = r_b(z, \phi)$, with continuous surface derivatives over the vehicle. The appropriate subroutines from QUICK have been included in the present flow-field code so that the geometry models generated by QUICK can be used in the present code for making flow-field calculations.

Two versions of the geometry of the Space Shuttle orbiter (shown in fig. 4) have been modeled with QUICK as shown in figure 5. The first (fig. 5(a)) is a reasonably accurate model of the actual vehicle with the canopy, vertical tail, and orbital maneuverable system (OMS) pod removed. The second (fig. 5(b)) has the same lower surface shape and the same profile for the upper symmetry plane as the first, but the region between the leading edge of the strake or wing and the upper symmetry plane have been replaced with elliptical segments as shown by dashed lines in section A-A of figure 4. This process simplifies the leeside geometry and makes calculations in this region easier but does not affect the results obtained on the windward side since the cross-flow velocity goes supersonic near the wing tip. Since the flow in the lower part of the shock layer on the leeside of a vehicle at large angle of attack is viscous dominated (ref. 14) and cannot be accurately modeled with the inviscid equations of motion, alteration of the inviscid solution on the leeside (due to the modification of the leeside geometry) is of little consequence. Thus, all the results for the flow field over the Space Shuttle orbiter presented in the present paper were obtained with the modified geometry shown in figure 5(b).

METHOD OF SOLUTION

Flow-Field Equations

The flow field of interest in this paper, will contain one or more internal shock waves. Specifically, a cross-flow shock will be located on the leeside of the vehicle near the upper symmetry plane, and under certain conditions a strake/wing shock may appear. These shock waves must be properly resolved; thus, we have chosen to "capture" these shocks since this technique is compatible with the vector-processing characteristics of the CYBER 203 computer. Thus, in this paper, the time-dependent, three-dimensional, compressible Euler equations are integrated in the weak conservation form. These equations can be written in the general form in the spherical coordinate system as

$$\frac{\partial \bar{W}}{\partial t} + \frac{\partial \bar{F}}{\partial r} + \frac{\partial \bar{G}}{\partial \theta} + \frac{\partial \bar{H}}{\partial \phi} + \bar{Q} = 0 \tag{3}$$

where the vectors $\bar{W}$, $\bar{F}$, $\bar{G}$, and $\bar{H}$ represent the usual conserved quantities in the spherical coordinate system and the vector $\bar{Q}$ contains all the terms that arise from

the use of a non-Cartesian coordinate system. In appendix A, the form of these vectors is given for spherical coordinates in equations (A2). Likewise, the equations can be written in the cylindrical coordinate system as

$$\frac{\partial W}{\partial t} + \frac{\partial F}{\partial r} + \frac{\partial H}{\partial \phi} + \frac{\partial G}{\partial z} + Q = 0 \tag{4}$$

where the vectors W, F, H, G, and Q are given in equations (A8).

The flow equations (eqs. (3) and (4)) are transformed from the physical domain to separate computational cubes, one corresponding to each coordinate system, by the following equations which allow the description of a general body in terms of its radius. For the spherical system,

$$\left.\begin{aligned}
\bar{\eta} &= \frac{\bar{r} - \bar{r}_b(\bar{\phi}, \theta)}{\bar{r}_s(t, \bar{\phi}, \theta) - \bar{r}_b(\bar{\phi}, \theta)} \quad && (0 < \eta < 1) \\[2em]
\bar{\phi} &= \frac{\bar{\phi} + \pi/2}{\pi} \quad && (0 < \bar{\phi} < 1) \\[2em]
\omega &= \frac{\pi - \theta}{\pi/2} \quad && (0 < \omega < 1)
\end{aligned}\right\} \tag{5}$$

and for the cylindrical system,

$$\left.\begin{aligned}
\eta &= \frac{r - r_b(\phi, z)}{r_s(t, \phi, z) - r_b(\phi, z)} \quad && (0 < \eta < 1) \\[2em]
\psi &= \frac{\phi + \pi/2}{\pi} \quad && (0 < \psi < 1) \\[2em]
\xi &= \frac{z}{z_{max}} \quad && (0 < \xi < 1)
\end{aligned}\right\} \tag{6}$$

Details of the transformation are outlined in appendix A. Although the physical domain is transformed to a computational domain, the velocity components are not transformed, and they retain the same magnitude and direction in the computational mesh as they did in the physical grid. In this paper, all computations are made by using equally spaced meshes.

6

Numerical Procedure

The computational data base is arranged as shown in figure 6. The data base is arranged in an interleaved manner (ref. 15). Interleaving, the sequential storage of the data base associated with each computational plane, allows the efficient use of the virtual memory system of the computer should the size of the code ever exceed the available central memory.

Interior grid points.- The following discussion applies to all interior points in the computational space except for those lying in the plane $\theta = \pi$, which will be treated in a separate section. The governing equations (eqs. (A6) (spherical) and (A12) (cylindrical)) are integrated in time with an unsplit MacCormack differencing scheme (ref. 16). In the predictor step, the plane-by-plane integration is carried out from the plane $\theta = \pi$ to the plane $z = z_{max}$ with forward differences in each direction. (See fig. 6.)

The plane where the two coordinate systems are coincident is treated as part of the spherical system when integrating the governing equations. To construct the forward streamwise derivatives in the predictor step at the plane requires that a plane of data be established at $\theta = \frac{\pi}{2} - \Delta\theta$. This temporary plane of information is obtained by interpolation from the planes of data in the cylindrical system immediately downstream of the plane $z = 0$. The thermodynamic properties transfer directly from one coordinate system to the next; however, the interpolated velocity components in the cylindrical system must be mapped back to the appropriate velocity components in the spherical system.

To preserve the interleaving concept, the corrector step is begun in the plane $z = z_{max}$ and sweeps back to the plane $\theta = \pi$ by using backward differences. Since backward differences are used, no interpolation is needed when computing at the plane $\theta = \pi/2$ in the spherical system. Also, backward derivatives for use in the first computed plane in cylindrical system can be constructed directly from information in the plane $\theta = \pi/2$ since it is part of both coordinate systems. This construction must take into account that in the plane $\theta = \pi/2$,

$$u_z = -u_\theta$$

Differencing at boundaries.- The governing equations must be integrated at both the vehicle surface and the bow shock. To preserve the second-order spatial accuracy of the η derivatives at these boundaries, the method of Abbett (ref. 17) is followed and these derivatives in the spherical system are defined in the predictor step as

$$\left.\frac{\partial f}{\partial \bar{\eta}}\right|_w = \frac{1}{\Delta\bar{\eta}}(f_{w+1} - f_w)$$

$$\left.\frac{\partial f}{\partial \bar{\eta}}\right|_s = \frac{1}{\Delta\bar{\eta}}(f_s - f_{s-1})$$

\begin{equation}\tag{7a}\end{equation}

and in the corrector step as

$$\left.\frac{\partial f}{\partial \bar{\eta}}\right|_w = \frac{1}{\Delta \bar{\eta}}(-2f_w + 3f_{w+1} - f_{w+2})$$

$$\left.\frac{\partial f}{\partial \bar{\eta}}\right|_s = \frac{1}{\Delta \bar{\eta}}(2f_s - 3f_{s-1} + f_{s-2})$$

(7b)

Similar equations are used in the cylindrical system by replacing $\bar{\eta}$ with η. As shown by Abbett, the net effect of using these derivatives in the MacCormack differencing scheme is to have applied a second-order accurate, three-point backward difference at the boundary.

Shock derivatives.- Derivatives on the shock surface are necessary to update the physical grid and to determine post-shock properties. When evaluating the streamwise shock derivatives $\partial \bar{r}_s/\partial \theta$ and $\partial r_s/\partial z$, it is necessary to use noncentered four-point derivatives of the form

$$f'_i = \frac{1}{6 \Delta}(f_{i-2} - 6f_{i-1} + 3f_i + 2f_{i+1})$$

to prevent downstream disturbances from moving upstream along the shock and causing oscillations in the shock about the stagnation point. At the outflow boundary a three-point backward difference derivative is used for $\partial r_s/\partial z$. In the plane $\theta = \pi$, which at the shock is really a point and not a surface, best results are obtained when a centered two-point derivative is used for $\partial \bar{r}_s/\partial \theta$. Formulation of the streamwise shock derivatives by using noncentered four-point derivatives about the juncture of the two coordinate systems requires that interpolated values of the shock position be determined in both coordinate systems for both the predictor and corrector steps.

In the cross-flow planes, $\partial \bar{r}_s/\partial \bar{\phi}$ and $\partial r_s/\partial \phi$ are approximated by two-point centered derivatives.

Plane $\theta = \pi$.- The governing equations in the spherical coordinate system (eq. (A1)) are singular at $\theta = \pi$. In appendix B, a reduced set of equations, valid at $\theta = \pi$, are developed. The desire is to integrate these equations in a manner that is consistent with the integration scheme, that is, unsplit MacCormack scheme,

used in the rest of the symmetry plane. (See appendix B.) The equation to be integrated is equation (B6), which is restated below in the computational coordinates:

$$\frac{\partial \bar{\bar{W}}}{\partial t} + \frac{\partial \bar{\eta}}{\partial t}\frac{\partial \bar{\bar{W}}}{\partial \bar{\eta}} + \frac{\partial \bar{\eta}}{\partial \bar{r}}\frac{\partial \bar{\bar{F}}}{\partial \bar{\eta}} + \frac{\partial \bar{\eta}}{\partial \theta}\frac{\partial \bar{\bar{G}}}{\partial \bar{\eta}} + \frac{\partial \omega}{\partial \theta}\frac{\partial \bar{\bar{G}}}{\partial \omega} + \bar{\bar{Q}} + \frac{\partial \omega}{\partial \theta}\frac{\partial}{\partial \omega}\left(\frac{\partial \bar{\psi}}{\partial \bar{\phi}}\frac{\partial \bar{\bar{S}}}{\partial \bar{\psi}}\right) + \frac{\partial \bar{\eta}}{\partial \theta}\frac{\partial}{\partial \bar{\eta}}\left(\frac{\partial \bar{\psi}}{\partial \bar{\phi}}\frac{\partial \bar{\bar{S}}}{\partial \bar{\psi}}\right) = 0 \qquad (8)$$

The integration of equation (8) requires information from the first two data planes shown in figure 6. These two planes are shown in greater detail in the following sketch:
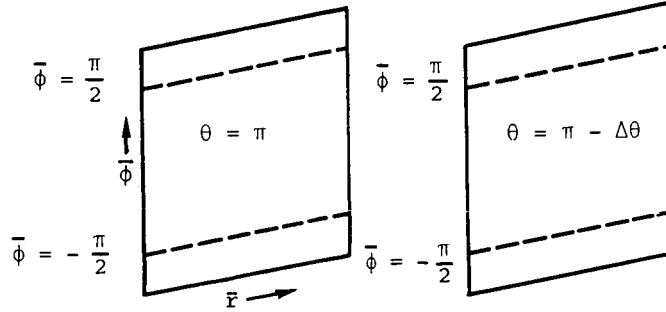
In appendix B, the number of equations represented by equation (8) was reduced from five to four (at $\theta = \pi$) by restricting the integration of equation (8) to points in the symmetry plane. To further simplify the integration, computations are done in the windward symmetry plane, $\bar{\phi} = -\pi/2$. In equation (8), the integration with respect to t is identical to that used in the rest of the flow field. In the predictor step, the derivative $\partial \bar{\bar{G}}/\partial \omega$ is taken to be

$$\frac{1}{\Delta \omega}\left[\bar{\bar{G}}\left(\theta = \pi - \Delta\theta, \bar{\phi} = -\frac{\pi}{2}, \bar{r}\right) - \bar{\bar{G}}\left(\theta = \pi, \bar{\phi} = -\frac{\pi}{2}, \bar{r}\right)\right] \qquad (9a)$$

and in the corrector step, the derivative $\partial \bar{\bar{G}}/\partial \omega$ is approximated by

$$\frac{1}{\Delta \omega}\left[\bar{\bar{G}}\left(\theta = \pi, \bar{\phi} = -\frac{\pi}{2}, \bar{r}\right) - \bar{\bar{G}}\left(\theta = \pi - \Delta\theta, \bar{\phi} = \frac{\pi}{2}, \bar{r}\right)\right] \qquad (9b)$$

When forming the quantities $\bar{\bar{G}}\left(\theta = \pi - \Delta\theta, \bar{\phi} = \frac{\pi}{2}, \bar{r}\right)$, the change in sign of u_θ must be taken into account when going from $\bar{\phi} = -\pi/2$ to $\bar{\phi} = \pi/2$. (See eq. (B2a).)

The formation of the second derivatives in equation (8) can be simplified by examining the behavior of derivatives with respect to $\bar{\phi}$ in the physical plane. First take $\partial\bar{\bar{S}}/\partial\bar{\phi}$ with $\bar{\bar{S}} = f u_{\bar{\phi}}$ so that

$$\frac{\partial(f u_{\bar{\phi}})}{\partial\bar{\phi}} = u_{\bar{\phi}}\frac{\partial f}{\partial\bar{\phi}} + f\frac{\partial u_{\bar{\phi}}}{\partial\bar{\phi}}$$

In the definition of $u_{\bar{\phi}}$ on $\theta = \pi$ (eq. (B2b)),

$$\frac{\partial u_{\bar{\phi}}}{\partial\bar{\phi}} = -u_\theta\Big|_{\bar{\phi}=-\pi/2}\sin\bar{\phi}$$

or

$$\frac{\partial u_{\bar{\phi}}}{\partial\bar{\phi}}\Big|_{\bar{\phi}=-\pi/2} = u\Big|_{\bar{\phi}=-\pi/2}$$

along the line $\bar{\phi} = -\pi/2$. Finally,

$$\frac{\partial\bar{\bar{S}}}{\partial\bar{\phi}} = u_\theta\Big|_{\bar{\phi}=-\pi/2}f + u_{\bar{\phi}}\frac{\partial f}{\partial\bar{\phi}} \tag{10}$$

Now $\bar{\bar{S}}$ (eq. (B4d)) can be written as

$$\bar{\bar{S}} = u_{\bar{\phi}}\bar{\bar{T}}$$

where

$$\bar{\bar{T}} = \begin{bmatrix} \bar{r}\rho \\ \bar{r}\rho u_{\bar{r}} \\ \bar{r}\rho u_\theta \\ \bar{r}(E + p) \end{bmatrix} \tag{11}$$

10

The substitution of $\bar{\bar{T}}$ for the dummy function f in equation (10), along with the fact that $\bar{\bar{T}}$ is an even function about the symmetry plane, leads to the expression

$$\frac{\partial \bar{\bar{S}}}{\partial \bar{\phi}} = u_\theta \bigg|_{\bar{\phi}=-\pi/2} \bar{\bar{T}}$$

From equations (A4),

$$\frac{\partial}{\partial \bar{\phi}} = \frac{\partial \bar{\eta}}{\partial \bar{\phi}} \frac{\partial}{\partial \bar{\eta}} + \frac{\partial \bar{\psi}}{\partial \bar{\phi}} \frac{\partial}{\partial \bar{\psi}}$$

and it has been established that $\dfrac{\partial \bar{\eta}}{\partial \bar{\phi}} = 0$ on $\theta = \pi$; thus,

$$\frac{\partial \bar{\bar{S}}}{\partial \bar{\phi}} = \frac{\partial \bar{\psi}}{\partial \bar{\phi}} \frac{\partial \bar{\bar{S}}}{\partial \bar{\psi}} = u_\theta \bigg|_{\bar{\phi}=-\pi/2} \bar{\bar{T}}$$

This allows us to write the term

$$\frac{\partial \bar{\eta}}{\partial \theta} \frac{\partial}{\partial \bar{\eta}} \left(\frac{\partial \bar{\psi}}{\partial \bar{\phi}} \frac{\partial \bar{\bar{S}}}{\partial \bar{\psi}} \right)$$

found in equation (8) as

$$\frac{\partial \bar{\eta}}{\partial \theta} \frac{\partial}{\partial \bar{\eta}} \left(u_\theta \bigg|_{\bar{\phi}=-\pi/2} \bar{\bar{T}} \right)$$

Thus, the differentiation can be handled the same as for the other $\bar{\eta}$ derivatives. In a similar manner, in the predictor step,

$$\frac{\partial \omega}{\partial \theta} \frac{\partial}{\partial \omega} \left(\frac{\partial \bar{\psi}}{\partial \bar{\phi}} \frac{\partial \bar{\bar{S}}}{\partial \bar{\psi}} \right) = \frac{1}{\Delta \omega} \frac{\partial \omega}{\partial \theta} \left[\left(\frac{\partial \bar{\psi}}{\partial \bar{\phi}} \bar{\bar{T}} \frac{\partial u_\phi}{\partial \bar{\psi}} \right) \bigg|_{\substack{\theta=\pi-\Delta\theta \\ \bar{\phi}=-\pi/2}} - \left(\bar{\bar{T}} u_\theta \right) \bigg|_{\substack{\theta=\pi \\ \bar{\phi}=-\pi/2}} \right] \tag{12a}$$

11

and in the corrector step,

$$\frac{\partial \omega}{\partial \theta} \frac{\partial}{\partial \omega}\left(\frac{\partial \bar{\phi}}{\partial \bar{\phi}} \frac{\partial \bar{\bar{S}}}{\partial \bar{\phi}}\right) = \frac{1}{\Delta \omega} \frac{\partial \omega}{\partial \theta}\left[\left.(\bar{\bar{T}} u\right)_{\theta}\right|_{\substack{\theta=\pi \\ \bar{\phi}=-\pi/2}} - \left.\left(\frac{\partial \bar{\phi}}{\partial \bar{\phi}} \bar{\bar{T}} \frac{\partial u_{\bar{\phi}}}{\partial \bar{\phi}}\right)\right|_{\substack{\theta=\pi-\Delta\theta \\ \bar{\phi}=\pi/2}}\right] \qquad (12b)$$

Again, care must be taken to properly account for the change in sign of u_θ in the symmetry plane $\bar{\phi} = \pi/2$.

The wall boundary conditions, in the plane $\theta = \pi$ are handled as in the rest of the flow field. Procedures for computations on the shock boundary are the same as those used in the rest of the field although some terms in the equations must be altered because of the coordinate singularity. These changes are included in the discussion of the shock computations in appendix D.

Boundary Conditions

Wall boundary.- For inviscid flow, the wall boundary condition requires that the velocity component normal to the wall be zero and that the surface entropy be constant at the post-normal-shock condition. In addition, in the steady state, the total enthalpy at every point in the flow field must be a constant.

The following procedure is used to satisfy these boundary conditions. The continuity and momentum equations are integrated along the surface. The computed wall density and the constant wall entropy condition are used to determine the internal energy and the pressure at the surface. Since, in general, the physical grid is not normal to the body surface nor the cross-flow and axial components of the velocity tangent to the body surface, the surface velocity boundary condition becomes $\vec{V}_b \cdot \hat{n}_b = 0$, where in the spherical system,

$$\vec{V}_b = u_{\bar{r},b} \hat{e}_{\bar{r}} + u_{\bar{\phi},b} \hat{e}_{\bar{\phi}} + u_{\theta,b} \hat{e}_\theta \qquad (13)$$

is the total velocity vector at the surface and $\hat{n}_b$ is the outer unit normal at the wall. In general, the velocity vector $\vec{V}_b$ formed from the velocities determined by integrating the momentum equations at the wall does not satisfy the tangency condition $\vec{V}_b \cdot \hat{n}_b = 0$ and lies outside the surface tangent plane. To correct the total velocity vector at the wall so that it lies in the surface tangency plane, a scheme similar to that outlined by Kutler (ref. 18) for use in a three-dimensional marching code is used. Unlike Kutler, the computed thermodynamic properties at the wall are assumed to be correct, and a set of surface velocities are sought which are consistent with those thermodynamic properties and the specified wall velocity condition. Although the resulting wall properties are inconsistent at any instant in

time, the solution at the wall converges as the global solution converges. For the general case,

$$\vec{V}_{b,N} = q_b \hat{n}_t \tag{14}$$

where

$$q_b = [2(H_w - h)]^{1/2} \tag{15}$$

is the total velocity at the surface, $\vec{V}_{b,N}$ is the corrected velocity vector on the body surface which lies in the surface tangent plane and

$$\hat{n}_t = \frac{\vec{V}_{b,o} - (\vec{V}_{b,o} \cdot \hat{n}_b)\hat{n}_b}{\left|\vec{V}_{b,o} - (\vec{V}_{b,o} \cdot \hat{n}_b)\hat{n}_b\right|} \tag{16}$$

is the unit vector in the surface tangency plane where $\vec{V}_{b,o}$ is the computed velocity vector at the wall.

In the spherical system, the outer unit normal at the wall is given by

$$\hat{n}_b = \frac{\hat{e}_{\bar{r}} - \dfrac{1}{\bar{r}_b}\dfrac{\partial \bar{r}_b}{\partial \theta}\hat{e}_\theta - \dfrac{1}{\bar{r}\sin\theta}\dfrac{\partial \bar{r}_b}{\partial \phi}\hat{e}_{\bar{\phi}}}{\left[1 + \left(\dfrac{1}{\bar{r}_b}\dfrac{\partial \bar{r}_b}{\partial \theta}\right)^2 + \left(\dfrac{1}{\bar{r}\sin\theta}\dfrac{\partial \bar{r}_b}{\partial \bar{\phi}}\right)^2\right]^{1/2}} \tag{17}$$

By combining equations (13) to (17), the following expressions can be determined for the velocity components at the surface:

$$u_{\bar{r},N} = q_b\left(u_{\bar{r},o} - \frac{D_1}{D_2}\right)\bigg/ D_3 \tag{18a}$$

$$u_{\theta,N} = q_b\left(u_{\theta,o} + \frac{D_1}{\bar{r}_b D_2}\frac{\partial \bar{r}_b}{\partial \theta}\right)\bigg/ D_3 \tag{18b}$$

$$u_{\bar{\phi},N} = q_b\left(u_{\bar{\phi},o} + \frac{D_1}{\bar{r}_b D_2 \sin\theta}\right)\frac{\partial \bar{r}_b}{\partial \bar{\phi}}\bigg/ D_3 \tag{18c}$$

where

$$D_1 = u_{\bar{r},o} - \frac{u_{\theta,o}}{\bar{r}_b} \frac{\partial \bar{r}_b}{\partial \theta} - \frac{u_{\bar{\phi},o}}{\bar{r} \sin \theta} \frac{\partial \bar{r}_b}{\partial \bar{\phi}}$$

$$D_2 = 1 + \left(\frac{1}{\bar{r}_b} \frac{\partial \bar{r}_b}{\partial \theta}\right)^2 + \left[\frac{\partial \bar{r}_b}{\partial \bar{\phi}} \middle/ (\bar{r}_b \sin \theta)\right]^2$$

$$D_3 = \left\{ \left(u_{\bar{r},o} - \frac{D_1}{D_2}\right)^2 + \left[u_{\theta,o} + D_1 \frac{\partial \bar{r}_b}{\partial \theta} \middle/ (\bar{r}_b D_2)\right]^2 \right.$$
$$\left. + \left[u_{\bar{\phi},o} + D_1 \frac{\partial \bar{r}_b}{\partial \bar{\phi}} \middle/ (\bar{r}_b D_2 \sin \theta)\right]^2 \right\}^{1/2}$$

In the cylindrical system, a similar analysis leads to the following expressions for the surface velocity components:

$$u_{r,N} = q_b \left(u_{r,o} - \frac{D_1}{D_2}\right) \middle/ D_3 \tag{19a}$$

$$u_{\phi,N} = q_b \left[u_{\phi,o} + D_1 \frac{\partial r_b}{\partial \phi} \middle/ (r_b D_2)\right] \middle/ D_3 \tag{19b}$$

$$u_{z,N} = q_b \left(u_{z,o} + D_1 \frac{\partial r_b}{\partial z} \middle/ D_2\right) \middle/ D_3 \tag{19c}$$

where

$$D_1 = u_{r,o} - u_{\phi,o}\left(\frac{\partial r_b}{\partial \phi} \middle/ r_b\right) - u_z \frac{\partial r_b}{\partial z}$$

$$D_2 = 1 + \left(\frac{\partial r_b}{\partial \phi} \middle/ r_b\right)^2 + \frac{\partial r_b}{\partial z}$$

$$D_3 = \left\{ \left(u_{r,o} - \frac{D_1}{D_2} \right)^2 + \left[u_{\phi,o} + D_1 \frac{\partial r_b}{\partial \phi} \middle/ (r_b D_2) \right]^2 + \left(u_{z,o} + D_1 \frac{\partial r_b}{\partial z} \middle/ D_2 \right)^2 \right\}^{1/2}$$

Shock boundary.- The bow shock, which is the outer boundary of the flow field, requires a time-dependent boundary condition, since the post-shock properties and shock location are a function of the computational time increment. The details of how the bow-shock boundary is handled in both coordinate systems are given in appendix C. Briefly, the post-shock properties are determined by the post-shock pressure and the local inclination of the shock to the free-stream velocity vector. The post-shock pressure is taken to be the pressure at the shock location determined by the integration of the flow-field equations. From this pressure and the shock geometry, new post-shock conditions and a shock velocity can be determined. If incremental movements of the shock are assumed to be small, then the change in radial location of the shock can be written in the spherical system as

$$d\bar{r}_s (\hat{n}_s \cdot \hat{e}_{\bar{r}}) = V_s \, dt \qquad (20a)$$

and in the cylindrical system as

$$dr_s (\hat{n}_s \cdot \hat{e}_r) = V_s \, dt \qquad (20b)$$

A MacCormack scheme is used to integrate these equations to update the position of the shock. At convergence, the computed post-shock pressure will give a zero shock speed and thus a stationary shock wave.

Outflow boundary.- Computations are always carried to a point where the axial flow at all grid points in the cross-flow plane is supersonic. We then integrate the regular interior point equations in the outflow plane by approximating axial derivatives with two-point backward differences in both the predictor and corrector steps.

Smoothing function.- Historically, flow-field calculations, with the MacCormack integration scheme, have required the addition of some damping to maintain numerical stability; the HALIS code is no exception. We have chosen to use the fourth-order smoother proposed by Barnwell (ref. 19). The smoothing is done on data in the computational plane and is applied at each time step after completion of the corrector step. Because of CPU (central processing unit) storage considerations, the primitive rather than conserved variables are smoothed; this has proven to be satisfactory. The smoothing is formulated as follows in the spherical system:

$$f^{t+\Delta t}_{\bar{\eta}, \bar{\psi}, \omega} = f^{t+\Delta t}_{\bar{\eta}, \bar{\psi}, \omega} - \varepsilon \left[(\Delta \omega)^4 \frac{\partial^4 f^t}{\partial \omega^4} + (\Delta \bar{\psi})^4 \frac{\partial^4 f^t}{\partial \bar{\psi}^4} + (\Delta \bar{\eta})^4 \frac{\partial^4 f^t}{\partial \bar{\eta}^4} \right] \qquad (21)$$

The same equation holds in the cylindrical system when ξ is substituted for ω, ψ for $\bar{\psi}$, and η for $\bar{\eta}$.

The fourth-order derivatives are formulated by using regular five-point central differences. In the η and $\bar{\eta}$ directions, at one point off the wall or shock, third-order derivatives using four-point differences are substituted for the fourth-order derivatives in equation (21). No damping is used in the η or $\bar{\eta}$ directions at the wall or the shock. A third-order derivative is substituted for the fourth-order ξ derivative in the next to the last plane in the cylindrical system whereas no smoothing is applied in the ξ direction on the outflow plane. Barnwell (ref. 19) has shown that $0 < \epsilon < 1/24$. A value of ϵ of 0.025 has been found to provide adequate damping without distorting the computed flow field.

Stability analysis.- A closed-form solution for the MacCormack differencing scheme when applied to the three-dimensional Euler equations is very difficult, if not impossible, to obtain. In appendix C, a rigorous derivation of the stability criterion for the Brailovskaya differencing scheme is given. It is further shown that under "worst-case" assumptions, stability for the MacCormack scheme reduces to that of Brailovskaya. Thus, the stability criterion used in this work is based on equation (C24).

At each point in the computational grid, the time integration is allowed to advance at its own local allowable time step. However, the streamwise distribution of time step should be smooth at the juncture of the two coordinate systems. To guarantee this smoothness, the magnitude of the local time steps in the spherical system is adjusted within the limits of the stability criterion.

The following usual definition of the limiting time step is used:

$$\Delta t = \frac{1}{\left| \lambda_{max} \right|} \tag{22}$$

where λ_{max} is the maximum eigenvalue occurring in the stability matrix. In the spherical coordinate system,

$$\left| \lambda_{max} \right| = g + a \left\{ \left(\frac{h}{\bar{r}} \right)^2 + \left(\frac{f}{\bar{r} \sin \theta} \right)^2 + \left[\frac{1}{(\bar{r}_s - \bar{r}_b) \Delta\bar{\eta}} \right]^2 \right\}^{1/2} \tag{23}$$

where a is the local speed of sound and

$$g = \left| \frac{1}{(\bar{r}_s - \bar{r}_b)\, \Delta\bar{\eta}} \left\{ u_{\bar{r}} - \bar{\eta}\frac{\partial \bar{r}_s}{\partial t} - \left[(1 - \bar{\eta})\frac{\partial \bar{r}_b}{\partial \theta} + \bar{\eta}\frac{\partial \bar{r}_s}{\partial \theta} \right]\frac{u_\theta}{\bar{r}} \right. \right.$$

$$\left. \left. - \left[(1 - \bar{\eta})\frac{\partial \bar{r}_b}{\partial \phi} + \bar{\eta}\frac{\partial \bar{r}_s}{\partial \phi} \right]\frac{u_{\bar{\phi}}}{\bar{r}\,\sin\theta} \right\} \right| + \left| \frac{2u_\theta}{\pi\bar{r}\,\Delta\omega} \right| + \left| \frac{u_{\bar{\phi}}}{\pi\bar{r}\,\sin\bar{\phi}\,\Delta\bar{\psi}} \right|$$

$$h = \frac{2}{\pi\,\Delta\omega} + \frac{1}{(\bar{r}_s - \bar{r}_b)\,\Delta\bar{\eta}}\left[(1 - \bar{\eta})\frac{\partial \bar{r}_b}{\partial \theta} + \bar{\eta}\frac{\partial \bar{r}_s}{\partial \theta} \right]$$

$$f = \frac{1}{(\bar{r}_s - \bar{r}_b)\,\Delta\bar{\eta}}\left[(1 - \bar{\eta})\frac{\partial \bar{r}_b}{\partial \phi} + \bar{\eta}\frac{\partial \bar{r}_s}{\partial \phi} \right] - \frac{1}{\pi\,\Delta\bar{\psi}}$$

In the cylindrical coordinate system,

$$\left| \lambda_{max} \right| = g + a\left\{ \left(\frac{h}{r}\right)^2 + f^2 + \left[\frac{1}{(r_s - r_b)\,\Delta\eta} \right]^2 \right\}^{1/2}$$

where again a is the speed of sound and

$$g = \left| \frac{1}{(r_s - r_b)\,\Delta\eta} \left\{ u_r - \eta\frac{\partial r_s}{\partial t} - \left[(1 - \eta)\frac{\partial r_b}{\partial \phi} + \eta\frac{\partial r_s}{\partial \phi} \right]\frac{u_\phi}{r} \right. \right.$$

$$\left. \left. - \left[(1 - \eta)\frac{\partial r_b}{\partial z} + \eta\frac{\partial r_s}{\partial z} \right]u_z \right\} \right| + \left| \frac{u_\phi}{\pi r\,\Delta\psi} \right| + \left| \frac{u_z}{z_{max}\,\Delta\xi} \right|$$

$$h = \frac{1}{(r_s - r_b)\,\Delta\eta}\left[(1 - \eta)\frac{\partial r_b}{\partial\phi} + \eta\,\frac{\partial r_s}{\partial\phi}\right] - \frac{1}{\pi\,\Delta\psi}$$

$$f = \frac{1}{(r_s - r_b)\,\Delta\eta}\left[(1 - \eta)\frac{\partial r_b}{\partial z} + \eta\,\frac{\partial r_s}{\partial z}\right] - \frac{1}{z_{max}\,\Delta\xi}$$

Further analysis indicates that the value of the smoothing coefficient used will affect the magnitude of the allowable time step size. From this analysis, equation (22) is replaced with the following equation when determining the maximum allowable local time step:

$$\Delta t < \frac{\left[1 - 96\varepsilon + (1 + 192\varepsilon)^{1/2}\right]^{1/2}}{\sqrt{2}\,\left|\lambda_{max}\right|}$$

Thermodynamics.- For perfect gas computations, the pressure is computed by using the state equation $p = (\gamma - 1)\rho e$ and the speed of sound from the equation $a^2 = \gamma(\gamma - 1)e$. A modified HALIS code has been written which incorporates equilibrium-air chemistry. This version uses the equilibrium-air curve fits of $p = p(\rho,e)$ and $a = a(\rho,e)$ done by Tannehill and Mugge (ref. 20). Some difficulty with convergence can be experienced when using these curve fits because of slight differences in thermodynamic properties at the juncture of fitted-curve segments. This problem has been overcome by checking for discontinuities in the thermodynamic properties at the juncture of fitted-curve segments and, where they exist, generating a smooth transition from one curve segment to the next. To reduce computation time when running this code, the nonvectorized chemistry code is called every 25th iteration. In the interim, a local effective γ is used in computing the pressure. This procedure keeps the time for equilibrium chemistry computations to approximately 20 percent greater than for a perfect gas.

Initialization

This method of solution, which is posed as an initial value problem, has required the development of an initialization procedure for the flow field about a complex three-dimensional geometry. In the following text, the flow initialization procedure as currently used in the HALIS code is described and is the result of the investigation of numerous initialization procedures for different parts of the flow field.

Surface properties.- Starting from the stagnation point, the Newtonian pressure on the surface is determined in the symmetry plane. On the leeside, the pressure is only allowed to drop to six times the free-stream pressure. The multiple six has no physical significance, but, using smaller values has, in some cases, led to negative pressures on the leeside. Then, the meridional pressure distribution is set in each plane by a sine function. Once the pressure distribution is set, an isentropic

expansion from the stagnation point gives the density and internal energy on the surface. The total velocity on the surface is then computed by assuming that the total enthalpy remains constant throughout the flow. To split the total velocity vector into its three components, the simplified streamline method of DeJarnette (ref. 21) is used to determine the direction cosines of the streamline at a point on the surface. Each component of velocity is then determined from the local total velocity and the appropriate direction cosine. In addition, this procedure auto-matically satisfies the surface boundary condition $\vec{V} \cdot \hat{n}_b = 0$.

Shock configuration and properties.- As described previously, the bow shock serves as the outer boundary of the coordinate system. We have found that it is imperative that a reasonable guess be made of the initial shock shape, that is, that the shock not be required to make large spatial adjustments. Initially, rotated paraboloids were used as initial shock shapes; this works well for short bodies at moderate angles of attack. However, this procedure breaks down for long bodies at high angles of attack as the shock on the windward side of the body will intersect the body surface.

Currently, a segmented approach is used to determine an initial shock shape. In reference to figure 7, the shock shape in the symmetry plane is broken into four separate curve segments, A-B, B-C, C-D, and D-E. Curve B-C is the locus of points which are equidistant from the body surface when measured along a body normal. The separation distance is the shock standoff distance, determined from the relation (ref. 22)

$$\delta_s = \frac{0.78}{\rho_s/\rho_\infty} \bar{r}_n$$

Curve C-D is a parabola which matches the slope and position of curve B-C at $\theta = \pi$. The point of intersection of the curve C-D and the ray $\theta = \pi/2$, $\bar{\phi} = \pi/2$ is a variable Γ, which depends on the angle of attack. Curve D-E is a straight line that matches the slope and position of curve C-D at Γ; thus, the choice of Γ determines the shape of the leeside shock. Curve A-B is a second-order curve which matches the slope and position of curve B-C at $\theta = \pi/2$, $\bar{\phi} = -\pi/2$ and has a slope equal to the body slope at $z = z_{max}$. In cross section, the shock shape is taken to be a circle whose diameter is the distance between the shock in lower and upper symmetry planes. Typical initial shock-shape cross sections are shown in figure 8 for several loca-tions of z. At first glance, this procedure appears very cumbersome. However, it is easily automated and is only dependent on picking a reasonable value of Γ, which for the specific geometry used in this paper varied from 85 inches to 140 inches over angles of attack from 25° to 45°. Once the shock geometry is established, the same procedure as outlined in appendix D for handling the unsteady shock wave can be used to find the initial post-shock properties by using steady-state shock relationships obtained by setting the shock velocity to zero in the relations of equations (D21), (D22), and (D23).

Interior grid points.- The interior grid points are initialized by first forming the conserved quantities W, $\bar{W}$, and $\bar{\bar{W}}$, as defined in appendixes A and B, along the shock and wall and then determining the values at the interior nodes by linear inter-

polation. The primitive variables are then separated from the conserved quantities and the pressure at each node is defined from the thermodynamic relation

$$p = p(\rho, e) \tag{26}$$

HALIS configuration and operational statistics.- The requirements on grid resolution and the CYBER 203 CPU memory size limit the extent of the modified Space Shuttle geometry (fig. 5(b)), which can be modeled in the present HALIS code. These restraints limit the modeling to the first 650 inches, which represents approximately 50 percent of the vehicle length measured from the nose to the body flap hinge line. In figure 6, each plane has 11 points in the η direction (distance between body and shock) and 32 points in the ϕ (meridional) direction. There are a total of 90 planes in the streamwise direction, the first 15 in the ω (or θ) direction in the spherical system and the rest in the ξ (or z) direction in the cylindrical system. Thus, the computational grid contains 31 680 grid points. The code requires that 22 variables be stored at each grid point. These variables include the old and new values of the flow-field variables, the physical coordinates, the local time step, and the smoothing variables. These storage requirements along with other storage needs and the associated computer code require all the CYBER 203 central memory of 10^6 64-bit words. In its present form, the code will generate converged solutions in 700 to 1500 global iterations for angles of attack from 20° to 45°. This corresponds to CPU time ranging from 2200 to 4500 seconds. A solution is considered to be converged when every point in the flow field meets the following criterion:

$$\frac{\rho^{t+\Delta t} - \rho^t}{\rho^t} < 10^{-4} \tag{27}$$

The HALIS code has a built-in restart capability which allows unconverged solutions to be continued or new solutions to be started from previously converged solutions. Using an old, converged solution to start a new one reduces by 10 to 15 percent the number of iterations required for convergence.

RESULTS AND DISCUSSION

Surface Boundary Conditions

The surface boundary condition plays an important role in the development of the subsonic axial flow along the windward surface. Some authors (refs. 3 and 9) have avoided the subsonic flow problem by using solution techniques which do not directly impose one of the surface boundary conditions, namely that of constant surface entropy. Allowing the surface entropy to take on a value determined by integration of the flow-field equations, in general, leads to a surface entropy lower than that required by the constant entropy condition. This effect is illustrated in figure 9(a) where center-line surface entropy is plotted as a function of Shuttle vehicle length for a constant and variable surface entropy condition. The lower surface entropy values in turn produce higher values of axial Mach number (fig. 9(b)) but leave the surface pressure distribution unaltered (fig. 9(c)). Thus, it would appear that, if surface pressures are the only required product, computations may be

20

made by using a variable surface entropy. However, not imposing the constant wall entropy boundary condition will alter the distribution of flow variables through the shock layer. These altered distributions make such computed flow fields incompatible with three-dimensional and quasi-three-dimensional boundary-layer codes which rely on the solutions from inviscid flow-field codes for boundary-layer edge conditions. The extent to which these distributions are altered is shown in figure 10 where variable distributions through the shock layer at $z/L = 0.1$, 0.25, and 0.45 on the windward symmetry plane center line are shown for a HALIS computation of a flow field about the Shuttle vehicle at $M_\infty = 10.3$ and $\alpha = 25°$. Figure 10(a) is an entropy plot for both the case of a constant and variable wall entropy. Differences between the two solutions increase with increasing z/L, with these differences confined to the lower third of the shock layer. In fact, at $z/L = 0.1$ the solutions are virtually the same. Figures 10(b) and 10(c) show plots of u_z, the axial component of velocity, and the density. The results are similar to those seen in the entropy plot. Figure 10(d) is a pressure plot which shows that the different entropy boundary conditions have no effect on the pressure distribution through the shock layer at all three axial locations. In figure 11, plots similar to those shown in figure 10 are presented for HALIS computations of flow over the Shuttle vehicle at $M_\infty = 10.3$ and $\alpha = 45°$. Figures 10 and 11 show that differences between constant wall entropy and variable wall entropy are more pronounced at the higher angle of attack. These differences between the two solutions extend to the lower one-half of the shock layer at $z/L = 0.45$ for all three variables: S (fig. 11(a)), u_z (fig. 11(b)), and ρ (fig. 11(c)). However, in figure 11(d) the pressure distribution through the shock layer is unaltered by the choice of wall entropy boundary condition.

Surface Axial Mach Number

When the proper surface boundary conditions are applied, the area of the windward surface having a subsonic axial velocity component should increase with angle of attack until the axial velocity component over the entire windward surface is subsonic as illustrated in figure 1 for the high-angle-of-attack case. Since the HALIS code requires a supersonic outflow boundary, it was necessary to alter the modified Shuttle geometry to include a slight expansion region aft of the 650-inch plane to raise the surface axial Mach number to a supersonic value.

In figure 12, the windward-surface center-line axial Mach number distributions are shown for angles of attack between 25° and 45° and a free-stream Mach number of 10.3. According to these results, if an initial data plane were established at $z = 150$ inches, then a spatial marching code such as STEIN (ref. 7) should be able to compute the flow over the vehicle at angles of attack up to 40°. However, practical experience with the STEIN code has shown that it is impractical and/or impossible to march into flows where M_z approaches 1. To determine, for this body and free-stream Mach number, what the limiting angle of attack for a STEIN solution would be, the HALIS code was used to establish an initial data plane at $z = 150$ inches. Complete STEIN solutions over the first 650 inches of the vehicle were obtained for angles of attack of 25°, 30°, and 35°. Center-line axial Mach numbers from STEIN solutions at $\alpha = 25°$, 30°, and 35° are plotted at 100-inch increments in figure 12 and agree with the complete HALIS solutions at the same angles of attack. For $\alpha = 40°$, the STEIN solution failed after the first step away from the initial supersonic data plane. A broader view of how the subsonic axial Mach number region spreads over the windward surface with increasing angle of attack can be found by comparing the parts of figure 13, which is a three-dimensional representation of the vehicle geometry being used with the physical grid superimposed on a black body. The white part of the vehicle surface represents the area of subsonic surface axial flow

21

and the black part represents the supersonic surface axial flow. The expansion region appended to the geometry can be seen at the aft end of the vehicle. At an angle of attack of 40°, a region of subsonic axial flow appears along the strake of the unmodified vehicle (fig. 5(a)), which appears as a chine along the modified vehicle. This subsonic axial flow is the result of the large expansion about this region at the higher angles of attack and the turning of the flow toward the upper symmetry plane which accompanies the expansion. At $\alpha = 42.5°$, there are three regions of subsonic flow: the region from the stagnation point aft, the region about the strake, and the region near the aft end of the vehicle. This last region near the aft end of the vehicle is the result of the flow recompressing after it has expanded down the vehicle from the stagnation point. At an angle of attack of 45°, the axial flow over the entire windward surface is subsonic.

Code Validation

To validate the HALIS code for flow about complex three-dimensional shapes, flow about a modified Shuttle vehicle at angle of attack has been computed at a condition for which there exist experimental data as well as numerical results from a different computer code. The numerical results were generated using the STEIN code (ref. 7), whereas the experimental data (ref. 23) were obtained in the Ames 3.5-Foot Hypersonic Wind Tunnel. In figure 14(a), a comparison is shown of numerical and experimental surface pressure coefficients on the windward center line plotted against nondimensional body length for an angle of attack of 25° and a free-stream Mach number of 10.29. The comparison between all four sets of data is excellent. In fact, the two numerical methods give almost the same results. This is interesting since both methods have the same resolution in the radial and meridional directions but the STEIN code has an axial resolution approximately eight times greater than the HALIS code. A further comparison of the experimental and numerical results for this case is shown in figure 14(b) where meridional distributions of surface pressure coefficients are plotted for three different axial locations on the vehicle. The numerical data are only plotted to approximately the tip of the vehicle strake since the geometry used in the computations has been modified (fig. 5(b)). There is good agreement between experimental data and both sets of numerical results for off-axis points. Figures 15 to 18 are similar plots of HALIS and wind-tunnel data for angles of attack from 30° to 45°. In all figures, there is very good agreement between the experimental data and the HALIS results.

Real Gas Computation

A comparison of perfect-gas ($\gamma = 1.4$) and real-gas computations for a $M_\infty = 18$ point on a typical Shuttle entry trajectory is shown in figures 19 and 20. A plot of center-line pressure coefficients is shown in figure 19. Real-gas effects are most prominent in the stagnation region and downstream, where the recompression is weaker than that shown for the perfect-gas case. Meridional pressure coefficient distributions for both the real- and perfect-gas cases at increasing values of z/L are shown in figure 20.

CONCLUDING REMARKS

In this paper, a computer code HALIS, designed to compute the three-dimensional flow about Shuttle-like configurations at angles of attack greater than 25°, has been described in detail. Results from HALIS have been compared where possible with an

existing flow-field code; such comparisons have shown excellent agreement. Also, HALIS results have been compared with experimental pressure distributions on Shuttle models over a wide range of angle of attack. These comparisons have again been excellent. It has also been demonstrated that the HALIS code can incorporate equilibrium air chemistry in flow-field computations.

Langley Research Center
National Aeronautics and Space Administration
Hampton, VA 23665
February 10, 1983

GENERAL TRANSFORMED EULER EQUATIONS

In this appendix the components of the Euler equations in both the spherical and cylindrical coordinate systems are identified. As well, the development of the transformed equations in the respective coordinate systems is presented.

Spherical System

In reference 24, the viscous compressible three-dimensional Navier-Stokes equations in conservative form are listed for a set of generalized coordinates. From these equations with the appropriate coordinates, metric coefficients, and zero viscosity, the compressible three-dimensional Euler equations in spherical coordinates can be written in vector form as

$$\frac{\partial \bar{W}}{\partial t} + \frac{\partial \bar{F}}{\partial \bar{r}} + \frac{\partial \bar{G}}{\partial \theta} + \frac{\partial \bar{H}}{\partial \bar{\phi}} + \bar{Q} = 0 \tag{A1}$$

where $\bar{W}$, $\bar{F}$, $\bar{G}$, $\bar{H}$, and $\bar{Q}$ are defined as

$$\bar{W} = \begin{bmatrix} \bar{r}^2 \rho \sin\theta \\[2mm] \bar{r}^2 \rho u_{\bar{r}} \sin\theta \\[2mm] \bar{r}^2 \rho u_\theta \sin\theta \\[2mm] \bar{r}^2 \rho u_{\bar{\phi}} \sin\theta \\[2mm] \bar{r}^2 E \sin\theta \end{bmatrix} \tag{A2a}$$

$$\bar{F} = \begin{bmatrix} \bar{r}^2 \rho u_{\bar{r}} \sin \theta \\ \bar{r}^2 \sin \theta \, (\rho u_{\bar{r}} + p) \\ \bar{r}^2 \rho u_{\bar{r}} \, u_\theta \sin \theta \\ \bar{r}^2 \rho u_{\bar{r}} \, u_{\bar{\phi}} \sin \theta \\ \bar{r}^2 u_{\bar{r}} \sin \theta \, (E + p) \end{bmatrix} \tag{A2b}$$

$$\bar{G} = \begin{bmatrix} \bar{r} \rho u_\theta \sin \theta \\ \bar{r} \rho u_{\bar{r}} \, u_\theta \sin \theta \\ \bar{r} \sin \theta \, (\rho u_\theta^2 + p) \\ \bar{r} \rho u_{\bar{\phi}} \, u_\theta \sin \theta \\ \bar{r} u_\theta \sin \theta \, (E + p) \end{bmatrix} \tag{A2c}$$

$$\bar{H} = \begin{bmatrix} \bar{r} \rho u_{\bar{\phi}} \\ \bar{r} \rho u_{\bar{r}} \, u_{\bar{\phi}} \\ \bar{r} \rho u_{\bar{\phi}} \, u_\theta \\ \bar{r} \, (\rho u_{\bar{\phi}}^2 + p) \\ \bar{r} u_{\bar{\phi}} \, (E + p) \end{bmatrix} \tag{A2d}$$

25

$$\bar{Q} = \begin{bmatrix} 0 \\ -\bar{r} \sin\theta \left[2p + \rho \left(u_{\bar{\phi}}^2 + u_{\theta}^2 \right) \right] \\ \bar{r}\rho u_{\bar{r}} u_{\theta} \sin\theta - \bar{r} \cos\theta \left(\rho u_{\bar{\phi}}^2 + p \right) \\ \bar{r}\rho u_{\bar{\phi}} \left(u_{\theta} \cos\theta + u_{\bar{r}} \sin\theta \right) \\ 0 \end{bmatrix}$$

(A2e)

Here, E is defined as $\rho \left[e + \dfrac{1}{2} \left(u_{\bar{r}}^2 + u_{\bar{\phi}}^2 + u_{\theta}^2 \right) \right]$, and $p = p(\rho, e)$.

The transformation from spherical to computational coordinates

$$(t, \bar{r}, \bar{\phi}, \theta) \rightarrow (\bar{t}, \bar{\eta}, \bar{\psi}, \omega)$$

is based on the following definitions:

$$\bar{t} = t$$

$$\bar{\eta} = \frac{\bar{r} - \bar{r}_b(\bar{\phi}, \theta)}{\bar{r}_s(t, \bar{\phi}, \theta) - \bar{r}_b(\bar{\phi}, \theta)} \qquad (0 \leqslant \bar{\eta} \leqslant 1)$$

$$\bar{\psi} = \frac{\bar{\phi} + \pi/2}{\pi} \qquad (0 \leqslant \bar{\psi} \leqslant 1)$$

$$\omega = \frac{\pi - \theta}{\pi/2} \qquad (0 \leqslant \omega \leqslant 1)$$

(A3)

with equations (A3) and the chain rule of partial differentiation, the derivative terms in the governing equations can be written in terms of derivatives in the computational space as

$$
\left.
\begin{aligned}
\frac{\partial}{\partial \bar{r}} &= \frac{\partial \bar{\eta}}{\partial \bar{r}} \frac{\partial}{\partial \bar{\eta}} \\[2em]
\frac{\partial \bar{\eta}}{\partial \bar{\phi}} &= \frac{\partial \bar{\eta}}{\partial \bar{\phi}} \frac{\partial}{\partial \bar{\eta}} + \frac{\partial \bar{\phi}}{\partial \bar{\phi}} \frac{\partial}{\partial \bar{\phi}} \\[2em]
\frac{\partial}{\partial \theta} &= \frac{\partial \bar{\eta}}{\partial \theta} \frac{\partial}{\partial \bar{\eta}} + \frac{\partial \omega}{\partial \theta} \frac{\partial}{\partial \omega} \\[2em]
\frac{\partial}{\partial t} &= \frac{\partial \bar{\eta}}{\partial t} \frac{\partial}{\partial \bar{\eta}} + \frac{\partial}{\partial \bar{t}}
\end{aligned}
\right\} \tag{A4}
$$

The derivatives, found in equations (A4), of the computational coordinates with respect to the physical coordinates are determined by using equations (A3) and are given as follows:

$$
\left.
\begin{aligned}
\frac{\partial \bar{\eta}}{\partial \bar{r}} &= \frac{1}{\bar{r}_s - \bar{r}_b} \\[2em]
\frac{\partial \bar{\eta}}{\partial \bar{\phi}} &= -\left[(\bar{r}_s - \bar{r})\frac{\partial \bar{r}_b}{\partial \bar{\phi}} + (\bar{r} - \bar{r}_b)\frac{\partial \bar{r}_s}{\partial \bar{\phi}}\right] \bigg/ (\bar{r}_s - \bar{r}_b)^2 \\[2em]
\frac{\partial \bar{\eta}}{\partial \theta} &= -\left[(\bar{r}_s - \bar{r})\frac{\partial \bar{r}_b}{\partial \theta} + (\bar{r} - \bar{r}_b)\frac{\partial \bar{r}_s}{\partial \theta}\right] \bigg/ (\bar{r}_s - \bar{r}_b)^2 \\[2em]
\frac{\partial}{\partial t} &= \left[\frac{\partial}{\partial \bar{t}} - (\bar{r} - \bar{r}_b)\frac{\partial \bar{r}_s}{\partial t}\right] \bigg/ (\bar{r}_s - \bar{r}_b)^2 \\[2em]
\frac{\partial \bar{\phi}}{\partial \bar{\phi}} &= \frac{1}{\pi} \\[2em]
\frac{\partial \omega}{\partial \theta} &= -\frac{2}{\pi}
\end{aligned}
\right\} \tag{A5}
$$

By replacing the partial derivatives in equation (A1) by their respective representation in the transformed space equations (eqs. (A4)), the equations to be solved on the computational grid can be written as follows:

$$\frac{\partial \bar{W}}{\partial \bar{t}} + \frac{\partial \bar{\eta}}{\partial t} \frac{\partial \bar{W}}{\partial \bar{\eta}} + \frac{\partial \bar{\eta}}{\partial \bar{r}} \frac{\partial \bar{F}}{\partial \bar{\eta}} + \frac{\partial \bar{\eta}}{\partial \theta} \frac{\partial \bar{G}}{\partial \bar{\eta}} + \frac{\partial \bar{\eta}}{\partial \phi} \frac{\partial \bar{H}}{\partial \bar{\eta}} + \frac{\partial \omega}{\partial \theta} \frac{\partial \bar{G}}{\partial \omega} + \frac{\partial \psi}{\partial \phi} \frac{\partial \bar{H}}{\partial \psi} + \bar{Q} = 0 \tag{A6}$$

The vectors $\bar{W}$, $\bar{F}$, $\bar{G}$, $\bar{H}$, and $\bar{Q}$ are unaffected by the transformation and the velocities are still defined in the spherical coordinate system which means that they are not necessarily aligned with any grid lines in the computational space.

Cylindrical System

From reference 24, the inviscid compressible three-dimensional Euler equations in cylindrical coordinates are written as

$$\frac{\partial W}{\partial t} + \frac{\partial F}{\partial r} + \frac{\partial H}{\partial \phi} + \frac{\partial G}{\partial z} + Q = 0 \tag{A7}$$

where W, F, H, G, and Q are defined as

$$W = \begin{bmatrix} r\rho \\ r\rho u_r \\ r\rho u_\phi \\ r\rho u_z \\ rE \end{bmatrix} \tag{A8a}$$

$$F = \begin{bmatrix} r\rho u_r \\ r\left(\rho u_r^2 + p\right) \\ r\rho u_r u_\phi \\ r\rho u_r u_z \\ ru_r(E + p) \end{bmatrix} \tag{A8b}$$

$$H = \begin{bmatrix} \rho u_\phi \\[1.5em] \rho u_r u_\phi \\[1.5em] \rho u_\phi^2 + p \\[1.5em] \rho u_\phi u_z \\[1.5em] \rho u_\phi(E + p) \end{bmatrix}$$

(A8c)

$$G = \begin{bmatrix} r\rho u_z \\[1.5em] r\rho u_r u_z \\[1.5em] r\rho u_\phi u_z \\[1.5em] r\left(\rho u_z^2 + p\right) \\[1.5em] ru_z(E + p) \end{bmatrix}$$

(A8d)

$$Q = \begin{bmatrix} 0 \\[1.5em] -\left(\rho u_\phi^2 + p\right) \\[1.5em] \rho u_r u_\phi \\[1.5em] 0 \\[1.5em] 0 \end{bmatrix}$$

(A8e)

Again, $E = \rho\left[e + \frac{1}{2}\left(u_r^2 + u_\phi^2 + u_z^2\right)\right]$, and $p = p(\rho, e)$. The transformation in the cylindrical system is similar to that in the spherical system where now we have

$$(t, r, \phi, z) \rightarrow (\bar{t}, \eta, \psi, \xi)$$

along with the definitions

$$\left.\begin{array}{ll}
\bar{t} = t & \\[2em]
\eta = \dfrac{r - r_b}{r_s(t, \phi, \theta) - r_b(\phi, z)} & (0 \leqslant \eta \leqslant 1) \\[2em]
\psi = \dfrac{\phi + \pi/2}{\pi} & (0 \leqslant \psi \leqslant 1) \\[2em]
\xi = \dfrac{z}{z_{max}} & (0 \leqslant \xi \leqslant 1)
\end{array}\right\} \tag{A9}$$

Again, the derivatives in the governing equations can be written as follows in terms of the derivatives in the computational space:

$$\left.\begin{array}{l}
\dfrac{\partial}{\partial r} = \dfrac{\partial \eta}{\partial r}\dfrac{\partial}{\partial \eta} \\[2em]
\dfrac{\partial}{\partial \phi} = \dfrac{\partial \eta}{\partial \phi}\dfrac{\partial}{\partial \eta} + \dfrac{\partial \psi}{\partial \phi}\dfrac{\partial}{\partial \psi} \\[2em]
\dfrac{\partial}{\partial z} = \dfrac{\partial \eta}{\partial z}\dfrac{\partial}{\partial \eta} + \dfrac{\partial \xi}{\partial z}\dfrac{\partial}{\partial \xi} \\[2em]
\dfrac{\partial}{\partial t} = \dfrac{\partial}{\partial \bar{t}} + \dfrac{\partial \eta}{\partial t}\dfrac{\partial}{\partial \eta}
\end{array}\right\} \tag{A10}$$

As before, the derivatives in equations (A10) can be determined from equations (A9) and are listed as follows:

$$
\left.
\begin{aligned}
\frac{\partial \eta}{\partial r} &= \frac{1}{r_s - r_b} \\[2ex]
\frac{\partial \eta}{\partial \phi} &= -\left[(r_s - r)\frac{\partial r_b}{\partial \phi} + (r - r_b)\frac{\partial r_s}{\partial \phi} \right] \Big/ (r_s - r_b)^2 \\[2ex]
\frac{\partial \eta}{\partial z} &= -\left[(r_s - r)\frac{\partial r_b}{\partial z} + (r - r_b)\frac{\partial r_s}{\partial z} \right] \Big/ (r_s - r_b)^2 \\[2ex]
\frac{\partial \psi}{\partial \phi} &= \frac{1}{\pi} \\[2ex]
\frac{\partial \xi}{\partial z} &= \frac{1}{z_{max}}
\end{aligned}
\right\}
\qquad \text{(A11)}
$$

Equation (A7) can be transformed to computational space by replacing the partial derivatives with equations (A10) to take on the following form:

$$
\frac{\partial W}{\partial \bar{t}} + \frac{\partial \eta}{\partial t}\frac{\partial W}{\partial \eta} + \frac{\partial \eta}{\partial r}\frac{\partial F}{\partial \eta} + \frac{\partial \eta}{\partial \phi}\frac{\partial H}{\partial \eta} + \frac{\partial \eta}{\partial z}\frac{\partial G}{\partial \eta} + \frac{\partial \psi}{\partial \phi}\frac{\partial H}{\partial \psi} + \frac{\partial \xi}{\partial z}\frac{\partial G}{\partial \xi} + Q = 0
\qquad \text{(A12)}
$$

Again, as in the spherical system, the vectors W, F, H, G, and Q are unaffected by the transformation to computational space, and the velocity components are still defined in the cylindrical system.

EULER EQUATIONS FOR $\theta = \pi$

The Euler equations in the spherical coordinate system, as defined by equation (A1), are singular along the ray $\theta = \pi$. To obtain a set of equations valid along this ray, the following procedure has been used. First, equation (A1) is differentiated with respect to θ and then $\lim \theta \to \pi$ is taken which results in the following set of equations:

Continuity:

$$\frac{\partial}{\partial t}\left(\bar{r}^2 \rho\right) + \frac{\partial}{\partial \bar{r}}(\bar{r}^2 \rho u_{\bar{r}}) + 2\frac{\partial}{\partial \theta}(\bar{r}\rho u_\theta) - \frac{\partial^2}{\partial \theta \, \partial \bar{\phi}}(\bar{r}\rho u_{\bar{\phi}}) = 0 \qquad \text{(B1a)}$$

$\bar{r}$ momentum:

$$\frac{\partial}{\partial t}\left(\bar{r}^2 \rho u_{\bar{r}}\right) + \frac{\partial}{\partial \bar{r}}\left[\bar{r}^2\left(\rho u_{\bar{r}}^2 + p\right)\right] + 2\frac{\partial}{\partial \theta}\left(\bar{r}\rho u_{\bar{r}} u_\theta\right)$$

$$- \frac{\partial^2}{\partial \theta \, \partial \bar{\phi}}\left(\bar{r}\rho \, u_{\bar{r}} \, u_{\bar{\phi}}\right) - \bar{r}\left[2p + \rho\left(u_{\bar{\phi}}^2 + u_\theta^2\right)\right] = 0 \qquad \text{(B1b)}$$

$\bar{\phi}$ momentum:

$$\frac{\partial}{\partial t}\left(\bar{r}^2 \rho u_{\bar{\phi}}\right) + \frac{\partial}{\partial \bar{r}}\left(\bar{r}^2 \rho u_{\bar{r}} u_{\bar{\phi}}\right) + 3\frac{\partial}{\partial \theta}\left(\bar{r}\rho u_{\bar{\phi}} u_\theta\right)$$

$$- \frac{\partial^2}{\partial \theta \, \partial \bar{\phi}}\left[\bar{r}\left(\rho u_{\bar{\phi}}^2 + p\right)\right] + \bar{r}\rho u_{\bar{r}} u_{\bar{\phi}} = 0 \qquad \text{(B1c)}$$

θ momentum:

$$\frac{\partial}{\partial t}\left(\bar{r}^2 \rho u_\theta\right) + \frac{\partial}{\partial \bar{r}}\left(\bar{r}^2 \rho u_{\bar{r}}\, u_\theta\right) + 2\,\frac{\partial}{\partial \theta}\left[\bar{r}\left(\rho u_\theta^2 + p\right)\right]$$

$$-\frac{\partial}{\partial \theta}\left[\bar{r}\left(\rho u_{\bar{\phi}}^2 + p\right)\right] - \frac{\partial^2}{\partial \theta\, \partial \bar{\phi}}\left(\bar{r}\rho u_{\bar{\phi}}\, u_\theta\right) + \bar{r}\rho u_{\bar{r}}\, u_\theta = 0 \qquad \text{(B1d)}$$

Energy:

$$\frac{\partial}{\partial t}\left(\bar{r}^2 E\right) + \frac{\partial}{\partial \bar{r}}\left[\bar{r}^2 u_{\bar{r}}\,(E + p)\right] + 2\,\frac{\partial}{\partial \theta}\left[\bar{r}u_\theta(E + p)\right] - \frac{\partial^2}{\partial \theta\, \partial \bar{\phi}}\left[\bar{r}u_{\bar{\phi}}\,(E + p)\right] \qquad \text{(B1e)}$$

Also, $E = \rho\left[e + \frac{1}{2}\left(u_{\bar{r}}^2 + u_{\bar{\phi}}^2 + u_\theta^2\right)\right]$ and $p = p(\rho, e)$.

Equations (B1) are valid along a line in space defined by $\theta = \pi$. However, this line actually represents a spatial plane. In dealing with the flow about $\theta = \pi$, the procedures outlined by Barnwell (ref. 19) are followed. For each value of $\bar{r}$ along the line, the thermodynamic properties are constant for all values of $\bar{\phi}$ as is the $\bar{r}$ component of velocity. However, the θ and $\bar{\phi}$ components of velocity will have to exhibit some dependence on $\bar{\phi}$ as illustrated in the following sketch:

33
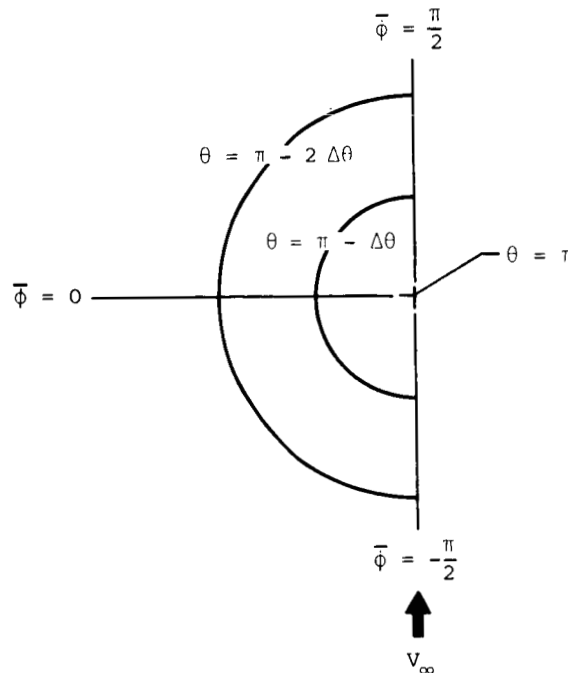
In the sketch, we show a $\bar{\phi}, \theta$ surface in the spherical coordinate system with a superimposed uniform positive velocity V_∞. Then for any line of constant θ the following conditions apply:

$$u_\theta = V_\infty \quad \text{and} \quad u_{\bar{\phi}} = 0 \qquad \left(\bar{\phi} = -\frac{\pi}{2} \right)$$

$$u_\theta = 0 \quad \text{and} \quad u_{\bar{\phi}} = V_\infty \qquad \left(\bar{\phi} = 0 \right)$$

$$u_\theta = -V_\infty \quad \text{and} \quad u_{\bar{\phi}} = 0 \qquad \left(\bar{\phi} = \frac{\pi}{2} \right)$$

These conditions will always apply along $\theta = \pi$ since $\bar{r}$ is not a function of $\bar{\phi}$ at this location and lead to the following expressions for u_θ and $u_{\bar{\phi}}$ as a function of $\bar{\phi}$:

$$u_\theta = -u_\theta \Big|_{\bar{\phi}=-\pi/2} \sin \bar{\phi} \qquad \text{(B2a)}$$

$$u_{\bar{\phi}} = u_\theta \Big|_{\bar{\phi}=-\pi/2} \cos \bar{\phi} \qquad \text{(B2b)}$$

The form of equations (B1) can be simplified if we choose to solve the equations only in the symmetry plane and then distribute the properties about the line $\theta = \pi$ as a function of $\bar{\phi}$. In the symmetry plane, the velocity component $u_{\bar{\phi}}$ is zero; this eliminates the need to integrate equation (B1c). We can then write the remaining equations in the vector form

$$\frac{\partial \bar{\bar{W}}}{\partial t} + \frac{\partial \bar{\bar{F}}}{\partial \bar{r}} + \frac{\partial \bar{\bar{G}}}{\partial \theta} + \frac{\partial^2 \bar{\bar{S}}}{\partial \theta \, \partial \bar{\phi}} + \bar{\bar{Q}} = 0 \qquad \text{(B3)}$$

where

$$\bar{\bar{W}} = \begin{bmatrix} \bar{r}^2 \rho \\ \bar{r}^2 \rho u_{\bar{r}} \\ \bar{r}^2 \rho u_\theta \\ \bar{r}^2 E \end{bmatrix} \qquad \text{(B4a)}$$

34

$$\bar{\bar{F}} = \begin{bmatrix} \bar{r}^2 \rho u_{\bar{r}} \\[2ex] \bar{r}^2 \left(\rho u_{\bar{r}}^2 + p\right) \\[2ex] \bar{r}^2 \rho u_{\bar{r}} u_\theta \\[2ex] \bar{r}^2 u_{\bar{r}} (E + p) \end{bmatrix} \tag{B4b}$$

$$\bar{\bar{G}} = \begin{bmatrix} 2\bar{r}\rho u_\theta \\[2ex] 2\bar{r}\rho u_{\bar{r}} u_\theta \\[2ex] 2\bar{r}\left(\rho u_\theta^2 + p\right) - \bar{r}\left(\rho u_{\bar{\phi}}^2 + p\right) \\[2ex] 2\bar{r} u_\theta (E + p) \end{bmatrix} \tag{B4c}$$

$$\bar{\bar{S}} = \begin{bmatrix} \bar{r}\rho u_{\bar{\phi}} \\[2ex] \bar{r}\rho u_{\bar{r}} u_{\bar{\phi}} \\[2ex] \bar{r}\rho u_\theta u_{\bar{\phi}} \\[2ex] \bar{r} u_{\bar{\phi}} (E + p) \end{bmatrix} \tag{B4d}$$

$$\bar{Q} = \begin{bmatrix} 0 \\[2ex] -\bar{r}\left[2p + \rho\left(u_{\bar{\phi}}^2 + u_\theta^2\right)\right] \\[2ex] \bar{r}\rho u_{\bar{r}} u_\theta \\[2ex] 0 \end{bmatrix} \tag{B4e}$$

When the derivative definitions (eqs. (A4)) are substituted into equation (B3), the following equation, valid in the computational space, is generated:

$$
\frac{\partial \bar{\bar{W}}}{\partial \bar{t}} + \frac{\partial \bar{\eta}}{\partial t} \frac{\partial \bar{\bar{W}}}{\partial \bar{\eta}} + \frac{\partial \bar{\eta}}{\partial \bar{r}} \frac{\partial \bar{\bar{F}}}{\partial \bar{\eta}} + \frac{\partial \bar{\eta}}{\partial \theta} \frac{\partial \bar{\bar{G}}}{\partial \bar{\eta}} + \frac{\partial \omega}{\partial \theta} \frac{\partial \bar{\bar{G}}}{\partial \omega}
$$

$$
+ \left(\frac{\partial \bar{\eta}}{\partial \theta} \frac{\partial}{\partial \bar{\eta}} + \frac{\partial \omega}{\partial \theta} \frac{\partial}{\partial \omega} \right) \left(\frac{\partial \bar{\eta}}{\partial \bar{\phi}} \frac{\partial}{\partial \bar{\eta}} + \frac{\partial \bar{\psi}}{\partial \bar{\phi}} \frac{\partial}{\partial \bar{\psi}} \right) \bar{\bar{S}} + \bar{\bar{Q}} = 0 \tag{B5}
$$

Now $\bar{r}_s$ and $\bar{r}_b$ are not functions of $\bar{\phi}$ on $\theta = \pi$. Therefore, $\partial \bar{\eta}/\partial \bar{\phi}$ is zero on $\theta = \pi$; this simplifies equation (B5) to

$$
\frac{\partial \bar{\bar{W}}}{\partial \bar{t}} + \frac{\partial \bar{\eta}}{\partial t} \frac{\partial \bar{\bar{W}}}{\partial \bar{\eta}} + \frac{\partial \bar{\eta}}{\partial \bar{r}} \frac{\partial \bar{\bar{F}}}{\partial \bar{\eta}} + \frac{\partial \bar{\eta}}{\partial \theta} \frac{\partial \bar{\bar{G}}}{\partial \bar{\eta}} + \frac{\partial \omega}{\partial \theta} \frac{\partial \bar{\bar{G}}}{\partial \omega} + \frac{\partial \omega}{\partial \theta} \frac{\partial}{\partial \omega} \left(\frac{\partial \bar{\psi}}{\partial \bar{\phi}} \frac{\partial \bar{\bar{S}}}{\partial \bar{\psi}} \right)
$$

$$
+ \frac{\partial \bar{\eta}}{\partial \theta} \frac{\partial}{\partial \bar{\eta}} \left(\frac{\partial \bar{\psi}}{\partial \bar{\phi}} \frac{\partial \bar{\bar{S}}}{\partial \bar{\psi}} \right) + \bar{\bar{Q}} = 0 \tag{B6}
$$

APPENDIX C

STABILITY ANALYSIS

M. J. Hamilton
Sperry Systems Management
Hampton, Virginia

Symbols

A	matrix of linearized coefficients of hyperbolic system
a	local speed of sound
B	coefficient matrixes for Euler equations in general coordinates
c_p	specific heat at constant pressure
c_v	specific heat at constant volume
D	weighted superposition of A matrixes used to simplify form of G
D_m	superposition of A matrixes used to simplify form of G_m
e	specific internal energy
F	coefficient functions of hyperbolic system
$\tilde{F}$	F evaluated at mesh nodes using $\tilde{U}$
G	amplification matrix for Brailovskaya's scheme
G_m	amplification matrix for MacCormack's scheme
g, β	abbreviations for quantities appearing frequently in amplification matrix for Euler equations in general coordinates
I	identity matrix
i,j,n,ℓ,k	indices
k	independent variable in frequency domain
P	similarity transform for Euler equations
q	arbitrary positive integer
S	set of all eigenvalues of D
t	time
U	dependent variable of hyperbolic system

$\tilde{U}$ approximation to U at mesh nodes from predictor step of Brailovskaya's scheme

u,v,w   Cartesian velocities for perfect gas

V   amplitude of Fourier transform component

x_i Cartesian coordinates

y_j independent variables of hyperbolic system

α wavelength associated with given wave number and mesh spacing, $\alpha_j = k_j \, \Delta y_j$

γ ratio of specific heats, c_p/c_v

Λ abbreviation used for terms in amplification matrix

λ arbitrary eigenvalue of D

ρ density of perfect gas

τ right-hand limit of time interval within which entries of G are uniformly bounded

General Analysis

    In this appendix the Von Neumann type stability criterion for hyperbolic equations in general coordinates is discussed. An explicit linearized stability criterion is given for application of Brailovskaya's finite-difference method (ref. C1) to the Euler equations. The resultant criterion is also shown to be necessary for MacCormack's method (ref. C2). Finally, the effect of "artificial viscosity" terms on the stability is computed.

    Consider the hyperbolic system

$$\frac{\partial U}{\partial t} + \sum_{i=1}^{n} \frac{\partial F_i}{\partial y_i} = 0 \tag{C1}$$

where $U(y_1,\ldots,y_n,t)$ and $F_i(U)$ are q-dimensional vectors, and $(y_1,\ldots,y_n)$ represents the chosen nonsingular coordinates. Brailovskaya's finite-difference scheme for equation (C1) is a two-step predictor-corrector method with centered differences. Applied to equation (C1), the predictor step is

$$\tilde{U}^{n+1}_{j_1,\ldots,j_n} = \tilde{U}^n_{j_1,\ldots,j_n} - \frac{\Delta t}{2} \sum_{\ell=1}^{n} \frac{F^n_{\ell,j_1,\ldots,j_{\ell+1},\ldots,j_n} - F^n_{\ell,j_1,\ldots,j_{\ell-1},\ldots,j_n}}{\Delta y_\ell} \tag{C2}$$

and the corrector step is

$$U^{n+1}_{j_1,\ldots,j_n} = U^n_{j_1,\ldots,j_n} - \frac{\Delta t}{2} \sum_{\ell=1}^{n} \frac{\tilde{F}^{n+1}_{\ell,j_1,\ldots,j_{\ell+1},\ldots,j_n} - \tilde{F}^{n-1}_{\ell,j_1,\ldots,j_{\ell-1},\ldots,j_n}}{\Delta y_\ell} \tag{C3}$$

As usual,

$$U^n_{j_1,\ldots,j_n} = U(j_1 \Delta y_1,\ldots,j_n \Delta y_n, n\Delta t)$$

Let

$$A_j = \frac{\partial F_j}{\partial U}$$

be treated as constant at each time level. We then apply the usual Von Neumann analysis (ref. C3) to the linearized system

$$\frac{\partial U}{\partial t} + \sum_{j=1}^{n} A_j \frac{\partial U}{\partial y_j} = 0 \tag{C4}$$

Let $U(k,t)$ denote the Fourier transform of $U(y,t)$, and let $\alpha_j = k_j \, \Delta y_j$. Set

$$U^n_{j_1,\ldots,j_n} = V^n \exp\left(i \sum_{\ell=1}^{n} j_\ell \alpha_\ell\right) \qquad (C5)$$

Together, equations (C2) through (C5) give

$$V^{n+1} = GV^n \qquad (C6)$$

with the amplification matrix

$$G = I - D^2 - iD \qquad (C7)$$

where

$$D = \Delta t \sum_{j=1}^{n} \frac{A_j \sin \alpha_j}{\Delta y_j} \qquad (C8)$$

Let the set of eigenvalues of D be denoted by S. From equation (C7), the Von Neumann criterion becomes

$$|\lambda| \leq 1 \quad \text{for all} \quad \lambda \in S \qquad (C9)$$

The scheme of MacCormack does not have the symmetry of the method of Brailovskaya. Because of this, the expression for the amplification matrix of MacCormack's scheme

analogous to equation (C7) is not simple. The MacCormack amplification matrix G_m becomes

$$G_m = I + \sum_{k=1}^{n} \left(\frac{A_k \, \Delta t}{\Delta y_k} \right)^2 (\cos \alpha_k - 1) - \sum_{k,j=1}^{n} \frac{A_k A_j (\Delta t)^2}{2 \, \Delta y_k \, \Delta y_j} \left[(\cos \alpha_k - 1)(\cos \alpha_j - 1) \right.$$

$$\left. + \sin \alpha_k \, \sin \alpha_j \right] + \sum_{\substack{k,j=1 \\ k<j}}^{n} \frac{(A_k A_j - A_j A_k)(\Delta t)^2}{2 \, \Delta y_k \, \Delta y_j} \left[\sin \alpha_k (\cos \alpha_j - 1) \right.$$

$$\left. - \sin \alpha_j (\cos \alpha_k - 1) \right] (1 + i) - i \, \Delta t \sum_{k=1}^{n} \frac{A_k \, \sin \alpha_k}{\Delta y_k} \qquad (C10)$$

If we assume $\alpha_k = \pi$, with $k = 1, 2, \ldots, n$, the MacCormack problem becomes tractable; this is equivalent to assuming alternating signs for the perturbation terms at adjacent mesh nodes. In this case, we find

$$G_m = I - 2(D_m)^2 \qquad (C11)$$

where

$$D_m = \Delta t \sum_{k=1}^{n} \frac{A_k}{\Delta y_k} \qquad (C12)$$

If S now denotes the eigenvalues of D_m, we again find our Von Neumann criterion as in equation (C9).

Application to Euler Equations

In Cartesian coordinates, with $U = (\rho, u, v, w, e)^T$, the linearized Euler equations for a perfect gas may be written in the form of equation (C4), where

$$A_1 = \begin{bmatrix} u & \rho & 0 & 0 & 0 \\ (\gamma - 1)e/\rho & u & 0 & 0 & \gamma - 1 \\ 0 & 0 & u & 0 & 0 \\ 0 & 0 & 0 & u & 0 \\ 0 & (\gamma - 1)e & 0 & 0 & u \end{bmatrix} \qquad \text{(C13a)}$$

$$A_2 = \begin{bmatrix} v & 0 & \rho & 0 & 0 \\ 0 & v & 0 & 0 & 0 \\ (\gamma - 1)e/\rho & 0 & v & 0 & \gamma - 1 \\ 0 & 0 & 0 & v & 0 \\ 0 & 0 & (\gamma - 1)e & 0 & v \end{bmatrix} \qquad \text{(C13b)}$$

$$A_3 = \begin{bmatrix} w & 0 & 0 & \rho & 0 \\ 0 & w & 0 & 0 & 0 \\ 0 & 0 & w & 0 & 0 \\ (\gamma - 1)e/\rho & 0 & 0 & w & \gamma - 1 \\ 0 & 0 & 0 & (\gamma - 1)e & w \end{bmatrix} \qquad \text{(C13c)}$$

Here ρ, (u,v,w), and e denote the density, Cartesian velocity, and internal energy, respectively. For computational tractability, we diagonalize A_2. Let a denote the local speed of sound, and define P as

$$P = \begin{bmatrix} -\rho/e & 0 & 0 & \rho\gamma/a^2 & -\rho\gamma/a^2 \\ 0 & 1 & 0 & 0 & 0 \\ 0 & 0 & 0 & \gamma/a & \gamma/a \\ 0 & 0 & 1 & 0 & 0 \\ 1 & 0 & 0 & 1 & -1 \end{bmatrix} \tag{C14}$$

Then the similarity transform $\bar{A}_2 = P^{-1} A_2 P$ gives

$$\bar{A}_2 = \text{diag}(v,v,v,v+a,v-a) \tag{C15}$$

For this transformation,

$$\bar{A}_1 = \begin{bmatrix} u & 0 & 0 & 0 & 0 \\ 0 & u & 0 & \gamma & -\gamma \\ 0 & 0 & u & 0 & 0 \\ 0 & a^2/2\gamma & 0 & u & 0 \\ 0 & -a^2/2\gamma & 0 & 0 & u \end{bmatrix} \tag{C16a}$$

$$\bar{A}_3 = \begin{bmatrix} w & 0 & 0 & 0 & 0 \\ 0 & w & 0 & 0 & 0 \\ 0 & 0 & w & \gamma & \gamma \\ 0 & 0 & a^2/2\gamma & w & 0 \\ 0 & 0 & -a^2/2\gamma & 0 & w \end{bmatrix} \tag{C16b}$$

Now transform to general coordinates. Let (x_1, x_2, x_3) be Cartesian; $y_\ell = y_\ell(x_j, t)$, a nonsingular transformation. In the new coordinates, the linearized Euler equation becomes

$$\frac{\partial U}{\partial t} + \sum_{j=1}^{3} B_j \frac{\partial U}{\partial y_j} = 0 \tag{C17}$$

with

$$B_j = \sum_{\ell=1}^{3} A_\ell \frac{\partial y_j}{\partial x_\ell} + I \frac{\partial y_j}{\partial t} \tag{C18}$$

The results of the section "General Analysis" then hold for equation (C17), with

$$D = \Delta t \sum_{j=1}^{3} \frac{B_j \sin \alpha_j}{\Delta y_j} \tag{C19}$$

Let $\alpha_{j\ell}$ denote the Jacobian matrix $\partial y_j / \partial x_\ell$, and perform the similarity transformation $\bar{D} = P^{-1} D P$. Make the further definitions

$$g = \Delta t \sum_{j=1}^{3} \frac{\sin \alpha_j}{\Delta y_j} \left(u\alpha_{j1} + v\alpha_{j2} + w\alpha_{j3} + \frac{\partial y_j}{\partial t} \right) \tag{C20}$$

$$\beta_j = \Delta t \sum_{\ell=1}^{3} \alpha_{\ell j} \frac{\sin \alpha_\ell}{\Delta y_\ell} \tag{C21}$$

Combining equations (C15) through (C21) gives

$$
\bar{D} = \begin{bmatrix}
g & 0 & 0 & 0 & 0 \\
0 & g & 0 & \gamma\beta_1 & -\gamma\beta_1 \\
0 & 0 & g & \gamma\beta_3 & -\gamma\beta_3 \\
0 & a^2\beta_1/2\gamma & & a^2\beta_3/2\gamma & 0 \\
0 & -a^2\beta_1/2\gamma & & -a^2\beta_3/2\gamma & g - a\beta_2
\end{bmatrix}
\tag{C22}
$$

A straightforward calculation now gives for the eigenvalues of $\bar{D}$

$$
S = \left(g, \; g, \; g, \; g + a\sqrt{\sum_{j=1}^{3} \beta_j^2}, \; g - a\sqrt{\sum_{j=1}^{3} \beta_j^2} \right)
\tag{C23}
$$

If the entries of G are uniformly bounded on an interval $0 < \Delta t < \tau$, and at most one eigenvalue in S has $|\lambda| = 1$, equation (C9) is sufficient for linearized stability (ref. C3). Since the entries of G are comprised of density, velocity, energy, and Jacobian terms, they should be bounded away from coordinate singularities; this is assumed to be the case. Then from equation (C23) we arrive at the condition

$$
\Delta t \left[\sum_{j=1}^{3} \frac{\left| u\alpha_{j1} + v\alpha_{j2} + w\alpha_{j3} + \dfrac{\partial y_j}{\partial t} \right|}{\Delta y_j} \right.
$$

$$
\left. + a\sqrt{\sum_{j,k=1}^{3} \left(\frac{\alpha_{jk}}{\Delta y_j}\right)^2 + 2 \sum_{\substack{j,k=1 \\ j<k}}^{3} \frac{\left| \alpha_{j1}\alpha_{k1} + \alpha_{j2}\alpha_{k2} + \alpha_{j3}\alpha_{k3} \right|}{\Delta y_j \, \Delta y_k}} \right] < 1
\tag{C24}
$$

For Cartesian coordinates, equation (C24) becomes the well-known

$$
\Delta t \left[\frac{|u|}{\Delta x_1} + \frac{|v|}{\Delta x_2} + \frac{|w|}{\Delta x_3} + a\sqrt{\frac{1}{\Delta x_1^2} + \frac{1}{\Delta x_2^2} + \frac{1}{\Delta x_3^2}} \right] < 1
\tag{C25}
$$

In comparing equations (C24) and (C25), we note

(1) $\frac{|u|}{\Delta x}$ has been replaced by $\frac{1}{\Delta y_j}\left|\frac{dy_j}{dt}\right|$; thus, stability depends upon the contravariant velocity components

(2) for an orthogonal transformation, the term under the square root in equation (C24) is $\sum\left(\frac{1}{\text{Mesh spacings}}\right)^2$, as in equation (C25)

For MacCormack's scheme, recall the special case of equation (C11). In this case, the preceding development holds, with D being replaced by D_m (eq. (C12)). One finds equation (C24) again necessary for stability.

For arbitrary phase, the computational intractability of G_m (eq. (C10)) makes it difficult to establish a general result or worst case. Computational experience seems to support the use of equation (C24) for MacCormack's scheme as well as for the more rigorously justified Brailovskaya case.

Artificial Viscosity Effects

From equations (C10) and (C11), it is clear that Brailovskaya's method is not dissipative. If $\sin \alpha_j = 0$ for all values of j or for any frequency if D has eigenvalues of 0 (in fluid dynamics, this will occur near stagnation or sonic points), then G has eigenvalues of 1. This is prevented by adding smoothing or damping terms to equation (C6). A fourth-order term often chosen in fluid mechanics is

$$-kI \sum_{\ell=1}^{n} \left[U^n_{j_1,\ldots,j_{\ell+2},\ldots,j_n} - 4U^n_{j_1,\ldots,j_{\ell+1},\ldots,j_n} + 6U^n_{j_1,\ldots,j_n} \right.$$
$$\left. - 4U^n_{j_1,\ldots,j_{\ell-1},\ldots,j_n} + U^n_{j_1,\ldots,j_{\ell-2},\ldots,j_n} \right] \tag{C26}$$

where k is the adjustable artificial viscosity coefficient. With this choice, equation (C10) becomes

$$G = I\Lambda - D^2 - iD \tag{C27}$$

where

$$\Lambda = 1 - 2k \sum_{j=1}^{n} (\cos 2\alpha_j - 4 \cos \alpha_j + 3) \tag{C28}$$

Equation (C9) now becomes

$$\left| (\Lambda - \lambda^2)^2 + \lambda^2 \right| < 1 \tag{C29}$$

This requires

$$\Lambda^2 < 1 \tag{C30}$$

Let λ denote the eigenvalues of D as before, with $\lambda_1 \Delta t = \lambda$. Then equation (C29) gives

$$\Delta t \left| \lambda_1 \right|_{max} < \sqrt{\frac{2\Lambda - 1 + (5 - 4\Lambda)^{1/2}}{2}} \tag{C31}$$

Our reasoning thus far is general: if equation (C26) is replaced by another damping term, equations (C27), (C29), (C30), and (C31) still hold, with equation (C28) modified appropriately. Equation (C30) restricts the choice of k. For a given k, equation (C31) then restricts our time step. For $k = 0$, equation (C31) reduces to equation (C9). Equations (C28) and (C30) give the requirement

$$0 < k < \frac{1}{8n} \tag{C32}$$

A restriction of the form of equation (C32) is known for other difference schemes (ref. C4). Additional restrictions of the form of equation (C31) do not appear to be widely recognized. Figure C1 shows $\Delta t \left| \lambda_1 \right|_{max}$ as a function of k for the choice (eq. (C26)) with $n = 2$ or 3.

APPENDIX C

References

C1. Brailovskaya, I. Yu.: A Difference Scheme for Numerical Solution of the Two-Dimensional, Nonstationary Navier-Stokes Equations for a Compressible Gas. Sov. Phys. - Doklady, vol. 10, no. 2, Aug. 1965, pp. 107-110.

C2. MacCormack, Robert W.: The Effect of Viscosity in Hypervelocity Impact Cratering. AIAA Paper No. 69-354, Apr.-May 1969.

C3. Richtmyer, Robert D.; and Morton, K. W.: Difference Methods for Initial-Value Problems, Second ed. Interscience Publ., c.1967.

C4. Barnwell, Richard W.: A Time-Dependent Method for Calculating Supersonic Blunt-Body Flow Fields With Sharp Corners and Embedded Shock Waves. NASA TN D-6031, 1970.
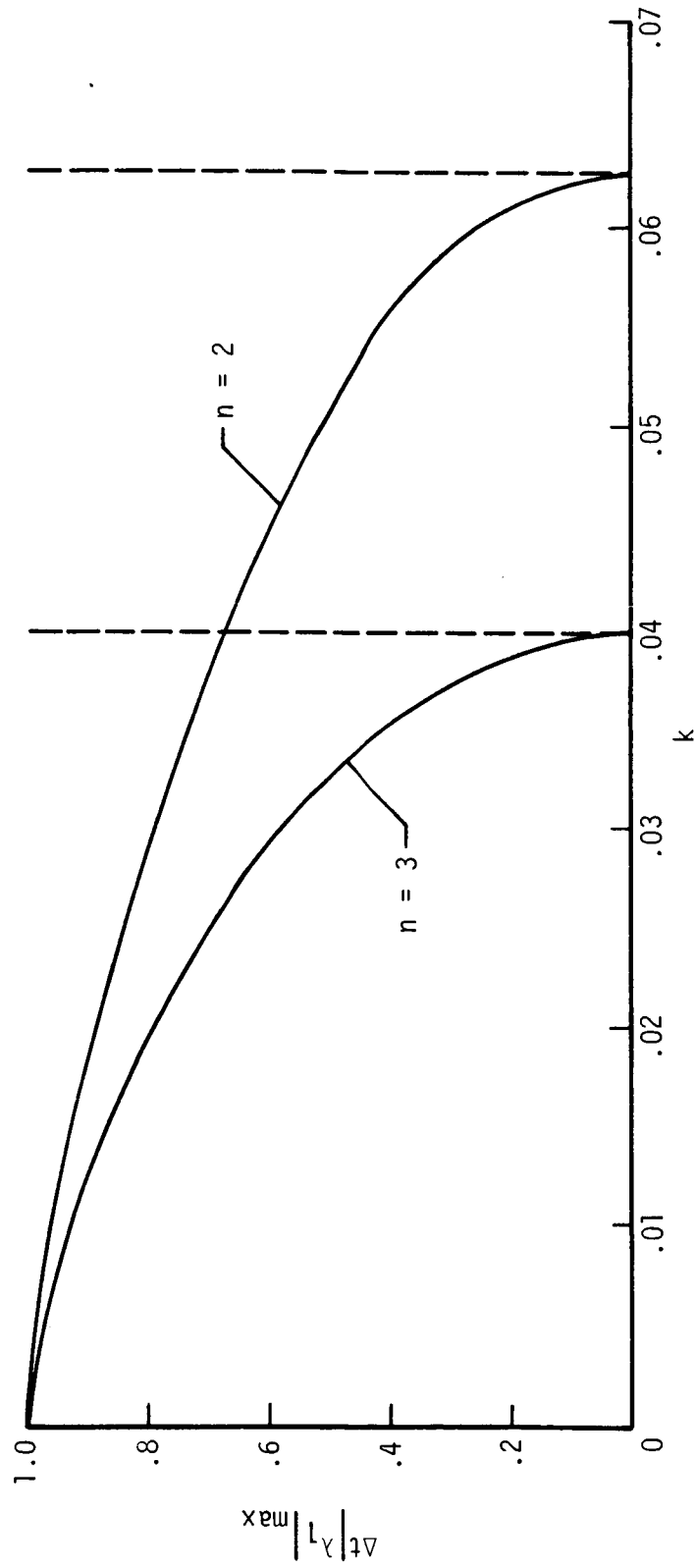
Figure C1.- Effect of artificial viscosity on time step.

APPENDIX D

CALCULATION OF PROPERTIES AT SHOCK WAVE

The shock velocity and other flow properties on the downstream side of the shock wave are calculated from the downstream pressure p_s by using a general three-dimensional extension of the axisymmetric method discussed in reference 24. The first step in the procedure is to resolve the velocity at the shock wave into an orthogonal shock-oriented system with components normal and tangent to the shock wave as illustrated in sketch A.
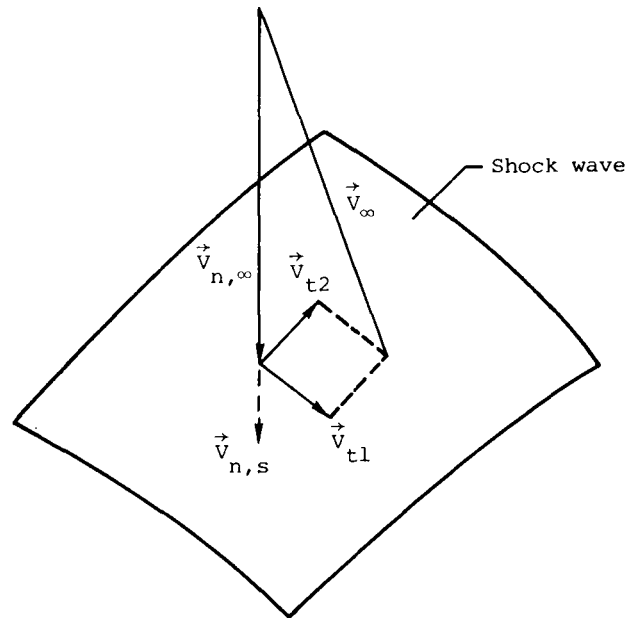
Sketch A

The next step is to compute the shock velocity and other flow properties at the shock (see sketch A) from the normal-shock-wave relations treating the downstream pressure p_s and the normal velocity component in the free stream as known quantities. The values of p_s used in this step of the procedure are obtained from the finite-difference solution of the flow-field equations at the shock. The final step is to resolve the velocity at the shock into the components in the coordinate system being used to make the flow computations. Since the details of the procedure are dependent on the coordinate system employed, the procedure will first be described for the spherical coordinate system used in the nose region and then for the cylindrical coordinate system used downstream.

Spherical Coordinate System

In spherical coordinates, the shock wave can be described by an equation of the form

$$F_s(\bar{r}, \theta, \bar{\phi}) = \bar{r} - \bar{r}_s(\theta, \bar{\phi}) = 0 \qquad (D1)$$

where $\bar{r}_s(\theta, \bar{\phi})$ is the radial distance to a discrete set of points which define the shock. The outer unit normal to the shock surface is given by the expression

$$\hat{n}_s = \nabla F_s \Big/ \left| \nabla F_s \right| \qquad (D2)$$

Thus for spherical coordinates, $\hat{n}_s$ becomes

$$\hat{n}_s = \left[\hat{e}_{\bar{r}} - \left(\frac{1}{\bar{r}_s} \frac{\partial \bar{r}_s}{\partial \theta} \right) \hat{e}_\theta - \left(\frac{1}{\bar{r}_s \sin\theta} \frac{\partial \bar{r}_s}{\partial \bar{\phi}} \right) \hat{e}_{\bar{\phi}} \right] \Big/ G_n \qquad (D3)$$

where

$$G_n = \sqrt{1 + \left(\frac{1}{\bar{r}_s} \frac{\partial \bar{r}_s}{\partial \theta} \right)^2 + \left(\frac{1}{\bar{r}_s \sin\theta} \frac{\partial \bar{r}_s}{\partial \bar{\phi}} \right)^2} \qquad (D4)$$

Now a unit vector $\hat{t}_{s1}$ is chosen such that it is tangent to the shock wave and the curve formed by the intersection of the shock wave and the plane $\bar{\phi}$ = Constant. Such a unit vector is given by the expression

$$\hat{t}_{s1} = \frac{\partial \bar{r}/\partial \theta}{\left| \partial \bar{r}/\partial \theta \right|} \qquad (D5)$$

where the vector $\bar{r}$ is defined as follows:

$$\bar{r} = \bar{r}_s(\theta, \bar{\phi}) \hat{e}_r \qquad (D6)$$

Thus,

$$\hat{t}_{s1} = \left[\left(\frac{\partial \bar{r}_s}{\partial \theta} \right) \hat{e}_r + \bar{r}_s \hat{e}_\theta \right] \bigg/ G_t \tag{D7}$$

where

$$G_t = \sqrt{ \left(\frac{\partial \bar{r}_s}{\partial \theta} \right)^2 + \bar{r}_s^{\,2} } \tag{D8}$$

Now a second unit vector $\hat{t}_{s2}$ tangent to the shock and perpendicular to both $\hat{n}_s$ and $\hat{t}_{s1}$ can be obtained from the vector cross product of $\hat{n}_s$ and $\hat{t}_{s1}$

$$\hat{t}_{s2} = \hat{n}_s \times \hat{t}_{s1} \tag{D9}$$

With equations (D3) and (D7), the following result is obtained for $\hat{t}_{s2}$

$$\hat{t}_{s2} = \left\{ \left(\frac{1}{\sin\theta} \frac{\partial \bar{r}_s}{\partial \bar{\phi}} \right) \hat{e}_{\bar{r}} - \left[\left(\frac{\partial \bar{r}_s}{\partial \theta} \right) \left(\frac{1}{\bar{r}_s} \frac{1}{\sin\theta} \frac{\partial \bar{r}_s}{\partial \bar{\phi}} \right) \right] \hat{e}_\theta \right.$$

$$\left. + \left[\bar{r}_s + \frac{1}{\bar{r}_s} \left(\frac{\partial \bar{r}_s}{\partial \theta} \right)^2 \right] \hat{e}_{\bar{\phi}} \right\} \bigg/ (G_n G_t) \tag{D10}$$

Now these three unit vectors $\hat{n}_s$, $\hat{t}_{s1}$, and $\hat{t}_{s2}$ defined by equations (D3), (D7), and (D10) can be written in the following short form

$$\hat{n}_s = N_{\bar{r}} \hat{e}_{\bar{r}} + N_\theta \hat{e}_\theta + N_{\bar{\phi}} \hat{e}_{\bar{\phi}} \tag{D11}$$

$$\hat{t}_{s1} = T_{1\bar{r}} \hat{e}_{\bar{r}} + T_{1\theta} \hat{e}_\theta + T_{1\bar{\phi}} \hat{e}_{\bar{\phi}} \tag{D12}$$

52

$$\hat{t}_{s2} = T_{2\bar{r}}\,\hat{e}_{\bar{r}} + T_{2\theta}\hat{e}_{\theta} + T_{2\phi}\,\hat{e}_{\bar{\phi}} \tag{D13}$$

where

$$N_{\bar{r}} = 1/G_n \tag{D14a}$$

$$N_{\theta} = -\left(\frac{1}{\bar{r}_s}\frac{\partial\bar{r}_s}{\partial\theta}\right)\bigg/G_n \tag{D14b}$$

$$N_{\bar{\phi}} = -\left(\frac{1}{\bar{r}_s\,\sin\,\theta}\frac{\partial\bar{r}_s}{\partial\bar{\phi}}\right)\bigg/G_n \tag{D14c}$$

$$T_{1\bar{r}} = \left(\frac{\partial\bar{r}_s}{\partial\theta}\right)\bigg/G_t \tag{D14d}$$

$$T_{1\theta} = \bar{r}_s/G_t \tag{D14e}$$

$$T_{1\bar{\phi}} = 0 \tag{D14f}$$

$$T_{2\bar{r}} = \left(\frac{1}{\sin\,\theta}\frac{\partial\bar{r}_s}{\partial\bar{\phi}}\right)\bigg/(G_n G_t) \tag{D14g}$$

$$T_{2\theta} = -\left(\frac{\partial\bar{r}_s}{\partial\theta}\right)\left(\frac{1}{\bar{r}_s\,\sin\,\theta}\frac{\partial\bar{r}_s}{\partial\bar{\phi}}\right)\bigg/(G_n G_t) \tag{D14h}$$

$$T_{2\bar{\phi}} = \left[\bar{r}_s + \frac{1}{\bar{r}_s}\left(\frac{\partial\bar{r}_s}{\partial\theta}\right)^2\right]\bigg/(G_n G_t) \tag{D14i}$$

53

Note that for the special case of $\theta = \pi$ and $\bar{\phi} = \pm\pi/2$, $N_{\bar{\phi}}$, $T_{2\bar{r}}$, $T_{2\theta}$, and G_n reduce to the following limiting forms:

$$
\left.
\begin{array}{l}
N_{\bar{\phi}} = T_{2\bar{r}} = T_{2\theta} = 0 \\[2em]
G_n = \sqrt{1 + \left(\dfrac{1}{\bar{r}_s} \dfrac{\partial \bar{r}_s}{\partial \theta}\right)^2}
\end{array}
\right\}
\qquad (\theta = \pi \text{ and } \bar{\phi} = \pm\pi/2)
\qquad\qquad \text{(D15)}
$$

The free-stream velocity in spherical coordinates is

$$
\vec{V}_\infty = V_{\bar{r},\infty}\,\hat{e}_{\bar{r}} + V_{\theta,\infty}\,\hat{e}_\theta + V_{\bar{\phi},\infty}\,\hat{e}_{\bar{\phi}}
\qquad\qquad \text{(D16)}
$$

where

$$
V_{\bar{r},\infty} = \left|\vec{V}_\infty\right|(\sin\alpha \sin\theta \sin\bar{\phi} + \cos\alpha \cos\theta)
\qquad\qquad \text{(D17a)}
$$

$$
V_{\theta,\infty} = \left|\vec{V}_\infty\right|(\sin\alpha \cos\theta \sin\bar{\phi} - \cos\alpha \sin\theta)
\qquad\qquad \text{(D17b)}
$$

$$
V_{\bar{\phi},\infty} = \left|\vec{V}_\infty\right| \sin\alpha \cos\bar{\phi}
\qquad\qquad \text{(D17c)}
$$

The free-stream velocity component normal to the shock wave $V_{n,\infty}$ is

$$
V_{n,\infty} = \vec{V}_\infty \cdot \hat{n}_s = N_{\bar{r}}\,V_{\bar{r},\infty} + N_\theta V_{\theta,\infty} + N_{\bar{\phi}}\,V_{\bar{\phi},\infty}
\qquad\qquad \text{(D18)}
$$

and the free-stream velocity components tangent to the shock wave $V_{t1,\infty}$ and $V_{t2,\infty}$ are

$$
V_{t1,\infty} = \vec{V}_\infty \cdot \hat{t}_{s1} = T_{1\bar{r}}\,V_{\bar{r},\infty} + T_{1\theta}V_{\theta,\infty} + T_{1\bar{\phi}}\,V_{\bar{\phi},\infty}
\qquad\qquad \text{(D19)}
$$

and

$$
V_{t2,\infty} = \vec{V}_\infty \cdot \hat{t}_{s2} = T_{2\bar{r}}\,V_{\bar{r},\infty} + T_{2\theta}V_{\theta,\infty} + T_{2\bar{\phi}}\,V_{\bar{\phi},\infty}
\qquad\qquad \text{(D20)}
$$

Although, the tangential components of velocity V_{t1} and V_{t2} are unchanged across the shock wave, the other properties illustrated in sketch B change and must be
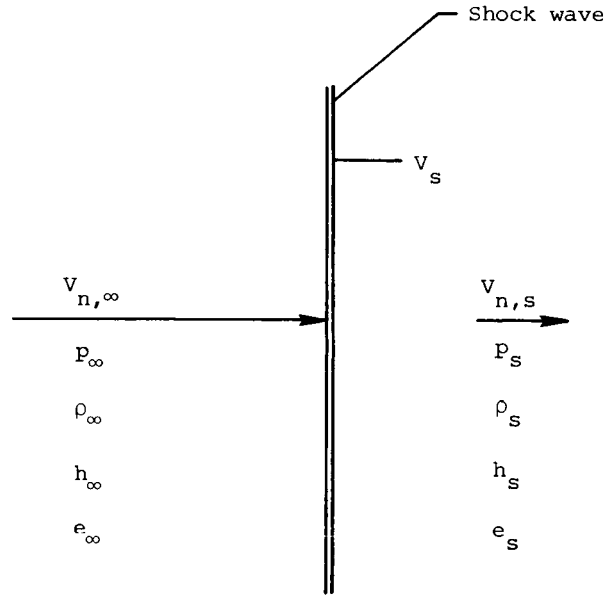
Sketch B

computed from the following normal-shock-wave relations for a moving shock:

$$\rho_\infty \left(V_{n,\infty} - V_s \right) = \rho_s \left(V_{n,s} - V_s \right) \tag{D21}$$

$$P_\infty + \rho_\infty \left(V_{n,\infty} - V_s \right)^2 = P_s + \rho_s \left(V_{n,s} - V_s \right)^2 \tag{D22}$$

$$h_\infty + \frac{\left(V_{n,\infty} - V_s \right)^2}{2} = h_s + \frac{\left(V_{n,s} - V_s \right)^2}{2} \tag{D23}$$

55

or, since $\rho_\infty = 1$, equations (D21) and (D22) become

$$\left(V_{n,\infty} - V_s\right) = \rho_s\left(V_{n,s} - V_s\right) \tag{D24}$$

$$P_\infty + \left(V_{n,\infty} - V_s\right)^2 = P_s + \rho_s\left(V_{n,s} - V_s\right)^2 \tag{D25}$$

Now, rearranging equation (D25) results in the following equation:

$$P_s - P_\infty = \left(V_{n,\infty} - V_s\right)^2\left[1 - \rho_s\frac{\left(V_{n,s} - V_s\right)^2}{\left(V_{n,\infty} - V_s\right)^2}\right] \tag{D26}$$

Combining this equation with equation (D24) and solving for $\left(V_{n,\infty} - V_s\right)^2$ gives the following equation:

$$\left(V_{n,\infty} - V_s\right)^2 = \frac{P_s - P_\infty}{1 - 1/\rho_s} \tag{D27}$$

Similarly, equation (D23) becomes

$$h_s = h_\infty + \frac{1}{2}\left(V_{n,\infty} - V_s\right)^2\left[1 - \left(\frac{1}{\rho_s}\right)^2\right] \tag{D28}$$

Equations (D27) and (D28) can be combined with an equation of state in the form

$$p = \rho\kappa h \tag{D29}$$

to yield the following result:

$$\frac{1}{\rho_s} = \frac{2h_\infty + (P_s - P_\infty)}{(2P_s/\kappa) - (P_s - P_\infty)} \tag{D30}$$

where for an ideal gas

$$\kappa = \frac{p}{\rho h} = \frac{\gamma - 1}{\gamma} \tag{D31}$$

56

and for a real gas, κ is evaluated from p, ρ, and h at the previous time step

$$\kappa = \left(\frac{p}{\rho h}\right)^{t-\Delta t} \tag{D32}$$

Equation (D32) is a good approximation of the value of κ at the early time steps and it becomes more and more "exact" as the solution approaches convergence. This process eliminates the need to iterate the shock-wave relations by using the "real-gas subroutines" and, thus, speeds up the solution considerably. With equation (D30), equation (D27) can be solved to obtain the following equation for the shock velocity V_s:

$$V_s = V_{n,\infty} - \sqrt{\frac{p_s - p_\infty}{1 - 1/\rho_s}} \tag{D33}$$

Then use this result in equation (D24) to obtain $V_{n,s}$ as

$$V_{n,s} = \frac{1}{\rho_s}(V_{n,\infty} - V_s) + V_s \tag{D34}$$

The enthalpy h_s can then be computed from equation (D28) and e_s from the relation

$$e_s = h_s - \frac{p_s}{\rho_s} \tag{D35}$$

The free-stream velocity components in the spherical coordinates $V_{r,\infty}$, $V_{\theta,\infty}$, and $V_{\phi,\infty}$ can be transformed to shock-oriented velocity components $V_{n,\infty}$, $V_{t1,\infty}$, and $V_{t2,\infty}$ by using the transformation matrix $\mathbf{A}$

$$\mathbf{A} = \begin{bmatrix} a_{11} & a_{12} & a_{13} \\ a_{21} & a_{22} & a_{23} \\ a_{31} & a_{32} & a_{33} \end{bmatrix} = \begin{bmatrix} T_{1\bar{r}} & T_{1\theta} & T_{1\bar{\phi}} \\ T_{2\bar{r}} & T_{2\theta} & T_{2\bar{\phi}} \\ N_{\bar{r}} & N_\theta & N_{\bar{\phi}} \end{bmatrix} \tag{D36}$$

as follows:

$$A \begin{bmatrix} v_{\bar{r},\infty} \\ v_{\theta,\infty} \\ v_{\bar{\phi},\infty} \end{bmatrix} = \begin{bmatrix} v_{t1,\infty} \\ v_{t2,\infty} \\ v_{n,\infty} \end{bmatrix} \tag{D37}$$

This same transformation matrix can be applied to conditions behind the shock wave; thus,

$$A \begin{bmatrix} u_{\bar{r},s} \\ u_{\theta,s} \\ u_{\bar{\phi},s} \end{bmatrix} = \begin{bmatrix} v_{t1,s} \\ v_{t2,s} \\ v_{n,s} \end{bmatrix} \tag{D38}$$

where

$$v_{t1,s} = v_{t1,\infty} \tag{D39a}$$

$$v_{t2,s} = v_{t2,\infty} \tag{D39b}$$

The spherical velocity components downstream of the shock wave can be determined from equation (D38) as follows:

$$\begin{bmatrix} u_{\bar{r},s} \\ u_{\theta,s} \\ u_{\bar{\phi},s} \end{bmatrix} = A^{-1} \begin{bmatrix} v_{t1,s} \\ v_{t2,s} \\ v_{n,s} \end{bmatrix} \tag{D40}$$

where A^{-1} is the inverse of the transformation matrix A. Now A^{-1} can be written in the general form

$$A^{-1} = \frac{1}{|A|}\, \text{Adj } A = \frac{1}{|A|}\begin{bmatrix} A_{11} & A_{21} & A_{31} \\ A_{12} & A_{22} & A_{32} \\ A_{13} & A_{23} & A_{33} \end{bmatrix} \tag{D41}$$

where $|A|$ is the determinant of the matrix A and A_{ij} is the cofactor of the element a_{ij}. For a spherical coordinate system we can write

$$|A| = T_{1\bar{r}}\left(T_{2\theta}N_{\bar{\phi}} - T_{2\bar{\phi}}N_\theta\right) - T_{1\theta}\left(T_{2\bar{r}}N_{\bar{\phi}} - T_{2\bar{\phi}}N_{\bar{r}}\right) \tag{D42}$$

and

$$A_{11} = T_{2\theta}N_{\bar{\phi}} - T_{2\bar{\phi}}N_\theta \tag{D43a}$$

$$A_{12} = -T_{2\bar{r}}N_{\bar{\phi}} + T_{2\bar{\phi}}N_{\bar{r}} \tag{D43b}$$

$$A_{13} = T_{2\bar{r}}N_\theta - T_{2\theta}N_{\bar{r}} \tag{D43c}$$

$$A_{21} = -T_{1\theta}N_{\bar{\phi}} \tag{D43d}$$

$$A_{22} = T_{1\bar{r}}N_{\bar{\phi}} \tag{D43e}$$

$$A_{23} = -T_{1\bar{r}}N_\theta + T_{1\theta}N_{\bar{r}} \tag{D43f}$$

$$A_{31} = T_{1\theta}T_{2\bar{\phi}} \tag{D43g}$$

$$A_{32} = -T_{1\bar{r}}T_{2\bar{\phi}} \tag{D43h}$$

$$A_{33} = T_{1\bar{r}}T_{2\theta} - T_{1\theta}T_{2\bar{r}} \tag{D43i}$$

Now from equations (D40) and (D41), the spherical velocity components downstream of the shock are obtained as follows:

$$u_{r,s}^- = \frac{1}{|A|}\left(A_{11}V_{t1,s} + A_{21}V_{t2,s} + A_{31}V_{n,s}\right) \tag{D44}$$

$$u_{\theta,s} = \frac{1}{|A|}\left(A_{12}V_{t1,s} + A_{22}V_{t2,s} + A_{32}V_{n,s}\right) \tag{D45}$$

$$u_{\phi,s}^- = \frac{1}{|A|}\left(A_{13}V_{t1,s} + A_{23}V_{t2,s} + A_{33}V_{n,s}\right) \tag{D46}$$

Cylindrical Coordinate System

In cylindrical coordinates, the shock wave can be described by an equation of the form

$$F_s(r,\phi,z) = r - r_s(\phi,z) \tag{D47}$$

In a procedure similar to that used with the spherical coordinate system, three unit vectors related to the shock wave are defined.

The first, $\hat{n}_s$, is the outer unit vector to the shock wave and is defined by

$$\hat{n}_s = N_r\hat{e}_r + N_\theta\hat{e}_\theta + N_\phi\hat{e}_\phi \tag{D48}$$

where

$$N_r = 1/G_n \tag{D49a}$$

$$N_\phi = -\left(\frac{1}{r_s}\frac{\partial r_s}{\partial \phi}\right)\Big/ G_n \tag{D49b}$$

$$N_z = -\left(\frac{\partial r_s}{\partial z}\right)\Big/ G_n \tag{D49c}$$

60

and

$$G_n = \sqrt{1 + \left(\frac{1}{r_s}\frac{\partial r_s}{\partial \phi}\right)^2 + \left(\frac{\partial r_s}{\partial z}\right)^2} \qquad \text{(D50)}$$

The second, $\hat{t}_{s1}$, is the unit vector tangent to the shock wave and the curve formed by the intersection of the shock and the plane $\phi = \text{Constant}$ and is defined by

$$\hat{t}_{s1} = T_{1r}\hat{e}_r + T_{1\phi}\hat{e}_\phi + T_{1z}\hat{e}_z \qquad \text{(D51)}$$

where

$$T_{1r} = \left(\frac{\partial r_s}{\partial z}\right)\Big/ G_t \qquad \text{(D52a)}$$

$$T_{1\phi} = 0 \qquad \text{(D52b)}$$

$$T_{1z} = 1/G_t \qquad \text{(D52c)}$$

and

$$G_t = \sqrt{\left(\frac{\partial r_s}{\partial z}\right)^2 + 1} \qquad \text{(D53)}$$

The third, $\hat{t}_{s2}$, is a unit vector perpendicular to both $\hat{n}_s$ and $\hat{t}_{s1}$ and is defined by

$$\hat{t}_{s2} = T_{2r}\hat{e}_r + T_{2\phi}\hat{e}_\phi + T_{2z}\hat{e}_z \qquad \text{(D54)}$$

where

$$T_{2r} = \left(\frac{1}{r_s}\frac{\partial r_s}{\partial \phi}\right)\Big/ (G_n G_t) \qquad \text{(D55a)}$$

$$T_{2\phi} = \left[1 + \left(\frac{\partial r_s}{\partial z}\right)^2\right] \Big/ (G_n G_t) \qquad (D55b)$$

$$T_{2z} = -\left(\frac{1}{r_s}\frac{\partial r_s}{\partial \phi}\right)\left(\frac{\partial r_s}{\partial z}\right) \Big/ (G_n G_t) \qquad (D55c)$$

The free-stream velocity in cylindrical coordinates is

$$\vec{V}_\infty = V_{r,\infty}\hat{e}_r + V_{\phi,\infty}\hat{e}_\phi + V_{z,\infty}\hat{e}_z \qquad (D56)$$

where

$$V_{r,\infty} = \left|\vec{V}_\infty\right| \sin \alpha \sin \phi \qquad (D57a)$$

$$V_{\phi,\infty} = \left|\vec{V}_\infty\right| \sin \alpha \cos \phi \qquad (D57b)$$

$$V_{z,\infty} = \left|\vec{V}_\infty\right| \cos \alpha \qquad (D57c)$$

The free-stream velocity component normal to the shock wave is given by

$$V_{n,\infty} = \vec{V}_\infty \cdot \hat{n}_s = N_r V_{r,\infty} + N_\phi V_{\phi,\infty} + N_z V_{z,\infty} \qquad (D58)$$

and the velocity components tangent to the shock wave are given by

$$V_{t1,\infty} = \vec{V}_\infty \cdot \hat{t}_{s1} = T_{1r} V_{r,\infty} + T_{1\phi} V_{\phi,\infty} + T_{1z} V_{z,\infty} \qquad (D59)$$

and

$$V_{t2,\infty} = \vec{V}_\infty \cdot \hat{t}_{s2} = T_{2r} V_{r,\infty} + T_{2\phi} V_{\phi,\infty} + T_{2z} V_{z,\infty} \qquad (D60)$$

Now the tangential components of velocity are unaffected by the shock wave; thus,

$$V_{t1,s} = V_{t1,\infty} \qquad (D61a)$$

$$V_{t2,s} = V_{t2,\infty} \qquad (D61b)$$

The velocity $V_{n,s}$ and other properties on the downstream side of the shock wave (sketch B) are computed by using equations (D23) through (D35) in exactly the same way as for the spherical coordinate system described previously.

Similarly, the cylindrical velocity components on the downstream side of the shock wave are computed from the equations

$$u_{r,s} = \frac{1}{|A|}\left(A_{11}V_{t1,s} + A_{21}V_{t2,s} + A_{31}V_{n,s}\right) \tag{D62}$$

$$u_{\phi,s} = \frac{1}{|A|}\left(A_{12}V_{t1,s} + A_{22}V_{t2,s} + A_{32}V_{n,s}\right) \tag{D63}$$

$$u_{z,s} = \frac{1}{|A|}\left(A_{13}V_{t1,s} + A_{23}V_{t2,s} + A_{33}V_{n,s}\right) \tag{D64}$$

where

$$|A| = T_{1r}\left(T_{2\phi}N_z - T_{2z}N_\phi\right) + T_{1z}\left(T_{2r}N_\phi - T_{2\phi}N_r\right) \tag{D65}$$

and

$$A_{11} = T_{2\phi}N_z - T_{2z}N_\phi \tag{D66a}$$

$$A_{12} = -T_{2r}N_z + T_{2z}N_r \tag{D66b}$$

$$A_{13} = T_{2r}N_\phi - T_{2\phi}N_r \tag{D66c}$$

$$A_{21} = T_{1z}N_\phi \tag{D66d}$$

$$A_{22} = T_{1r}N_z - T_{1z}N_r \tag{D66e}$$

$$A_{23} = -T_{1r}N_\phi \tag{D66f}$$

$$A_{31} = -T_{1z}T_{2\phi} \tag{D66g}$$

$$A_{32} = -T_{1r}T_{2z} + T_{1z}T_{2r} \tag{D66h}$$

$$A_{33} = T_{1r}T_{2\phi} \tag{D66i}$$

REFERENCES

1. Hamilton, H. Harris, II: Calculation of Laminar Heating Rates on Three-Dimensional Configurations Using the Axisymmetric Analogue. NASA TP-1698, 1980.

2. Moretti, Gino; and Bleich, Gary: Three-Dimensional Flow Around Blunt Bodies. AIAA J., vol. 5, no. 9, Sept. 1967, pp. 1557-1562.

3. Rizzi, Arthur W.; and Inouye, Mamoru: Time-Split Finite-Volume Method for Three-Dimensional Blunt-Body Flow. AIAA J., vol. 11, no. 11, Nov. 1973, pp. 1478-1485.

4. Hall, Darryl W.: Calculation of Inviscid Supersonic Flow Over Ablated Nosetips. AIAA Paper 79-0342, Jan. 1979.

5. Pulliam, Thomas H.; and Steger, Joseph L.: Implicit Finite-Difference Simulations of Three-Dimensional Compressible Flow. AIAA J., vol. 18, no. 2, Feb. 1980, pp. 159-167.

6. Marconi, F.; and Salas, M.: Computation of Three Dimensional Flows About Aircraft Configurations. Comput. & Fluids, vol. 1, no. 2, June 1973, pp. 185-195.

7. Marconi, Frank; Yaeger, Larry; and Hamilton, H. Harris: Computation of High-Speed Inviscid Flows About Real Configurations. Aerodynamic Analyses Requiring Advanced Computers - Part II, NASA SP-347, pp. 1411-1455.

8. Kutler, P.; Reinhardt, W. A.; and Warming, R. F.: Multishocked, Three-Dimensional Supersonic Flowfields With Real Gas Effects. AIAA J., vol. 11, no. 5, May 1973, pp. 657-664.

9. Rizzi, A. W.; Klazius, A.; and MacCormack, R. W.: A Generalized Hyperbolic Marching Technique for Three-Dimensional Supersonic Flow With Shocks. Proceedings of Fourth International Conference on Numerical Methods in Fluid Mechanics, Volume 35 of Lecture Notes in Physics, Robert D. Richtmyer, ed., Springer-Verlag, 1975, pp. 341-346.

10. Weilmuenster, K. James; and Howser, Lona M.: Solution of a Large Hydrodynamic Problem Using the STAR-100 Computer. NASA TM X-73904, 1976.

11. Weilmuenster, K. James; and Hamilton, H. Harris, II: A Method for Computation of Inviscid Three-Dimensional Flow Over Blunt Bodies Having Large Embedded Subsonic Regions. AIAA-81-1203, June 1981.

12. Weilmuenster, K. James; and Hamilton, H. Harris, II: A Comparison of Computed Space Shuttle Orbiter Surface Pressures With Flight Measurements. AIAA-82-0937, June 1982.

13. Vachris, Alfred F., Jr.; and Yaeger, Larry S.: QUICK-GEOMETRY - A Rapid Response Method for Mathematically Modeling Configuration Geometry. Applications of Computer Graphics in Engineering, NASA SP-390, 1975, pp. 49-73.

14. Helms, Vernon Talmadge, III: Flow Angle and Mass Flow Rate Measurements in the Leeside Flow Field of a Space Shuttle Configuration. M.S. Thesis, The George Washington Univ., Nov. 1977.

15. Lambiotte, Jules J., Jr.: Effect of Virtual Memory on Efficient Solution of Two Model Problems. NASA TM X-3512, 1977.

16. MacCormack, Robert W.: The Effect of Viscosity in Hypervelocity Impact Cratering. AIAA Paper No. 69-354, Apr.-May 1969.

17. Abbett, Michael J.: Boundary Condition Computational Procedures for Inviscid, Supersonic Steady Flow Field Calculations. Rept. 71-41 (Contract NAS2-6341), Aerotherm Corp., Nov. 30, 1971. (Available as NASA CR-114446.)

18. Kutler, Paul: Computation of Three-Dimensional, Inviscid Supersonic Flows. Progress in Numerical Fluid Dynamics, Volume 41 of Lecture Notes in Physics, H. J. Wirz, ed., Springer-Verlag, 1975, pp. 287-374.

19. Barnwell, Richard W.: A Time-Dependent Method for Calculating Supersonic Angle-of-Attack Flow About Axisymmetric Blunt Bodies With Sharp Shoulders and Smooth Nonaxisymmetric Blunt Bodies. NASA TN D-6283, 1971.

20. Tannehill, J. C.; and Mugge, P. H.: Improved Curve Fits for the Thermodynamic Properties of Equilibrium Air Suitable for Numerical Computation Using Time-Dependent or Shock-Capturing Methods. NASA CR-2470, 1974.

21. DeJarnette, Fred R.: Calculation of Inviscid Surface Streamlines and Heat Transfer on Shuttle Type Configurations. Pt. I.- Description of Basic Method. Contract No. NAS1-10277, North Carolina State Univ., 1971. (Available as NASA CR-111921.)

22. Seiff, Alvin: Recent Information on Hypersonic Flow Fields. Proceedings of the NASA-University Conference on the Science and Technology of Space Exploration, Volume 2, NASA SP-11, 1962, pp. 269-282. (Also available as NASA SP-24.)

23. Dye, W. H.; and Polek, T.: Results of Pressure Distribution Tests of a 0.010-Scale Space Shuttle Orbiter Model (61-0) in the NASA/ARC 3.5-Foot Hypersonic Wind Tunnel (Test OH38). NASA CR-144584, vols. 1-3, 1975.

24. Weilmuenster, K. James; and Hamilton, H. Harris, II: A Hybridized Method for Computing High-Reynolds-Number Hypersonic Flow About Blunt Bodies. NASA TP-1497, 1979.
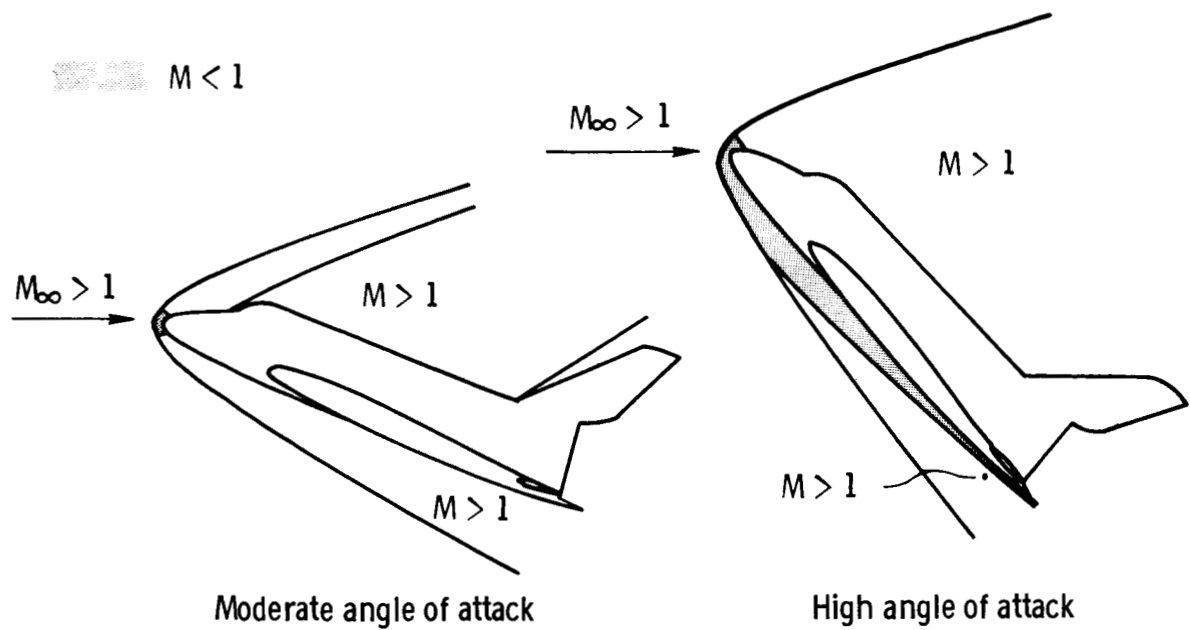
Figure 1.- External flow fields for super/hypersonic flight regime.
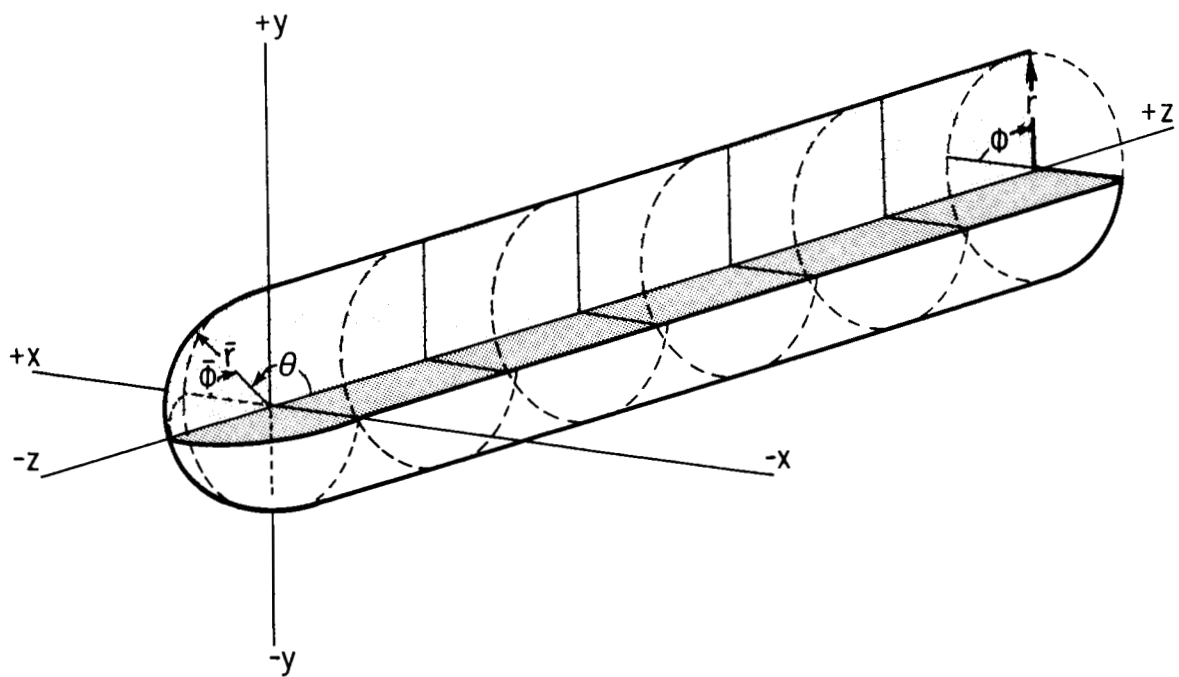
Figure 2.- Physical coordinate system.
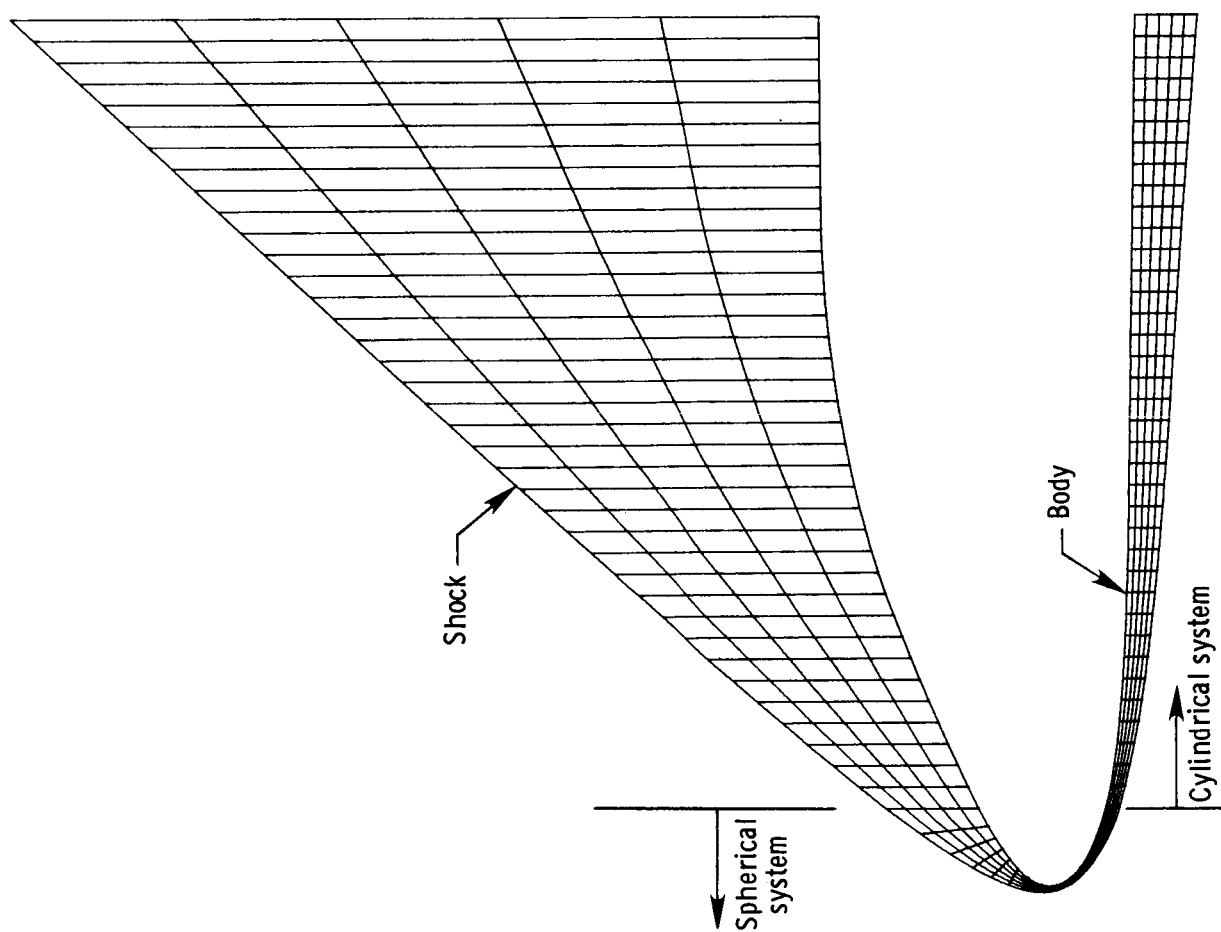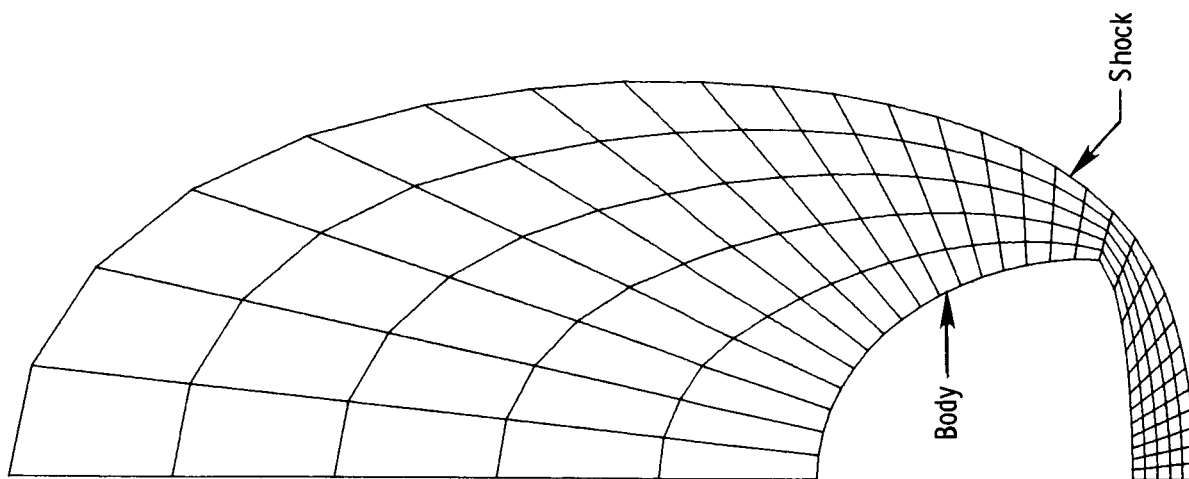
(b) Cross-flow plane.

(a) Symmetry plane.

Figure 3.- Physical grid.
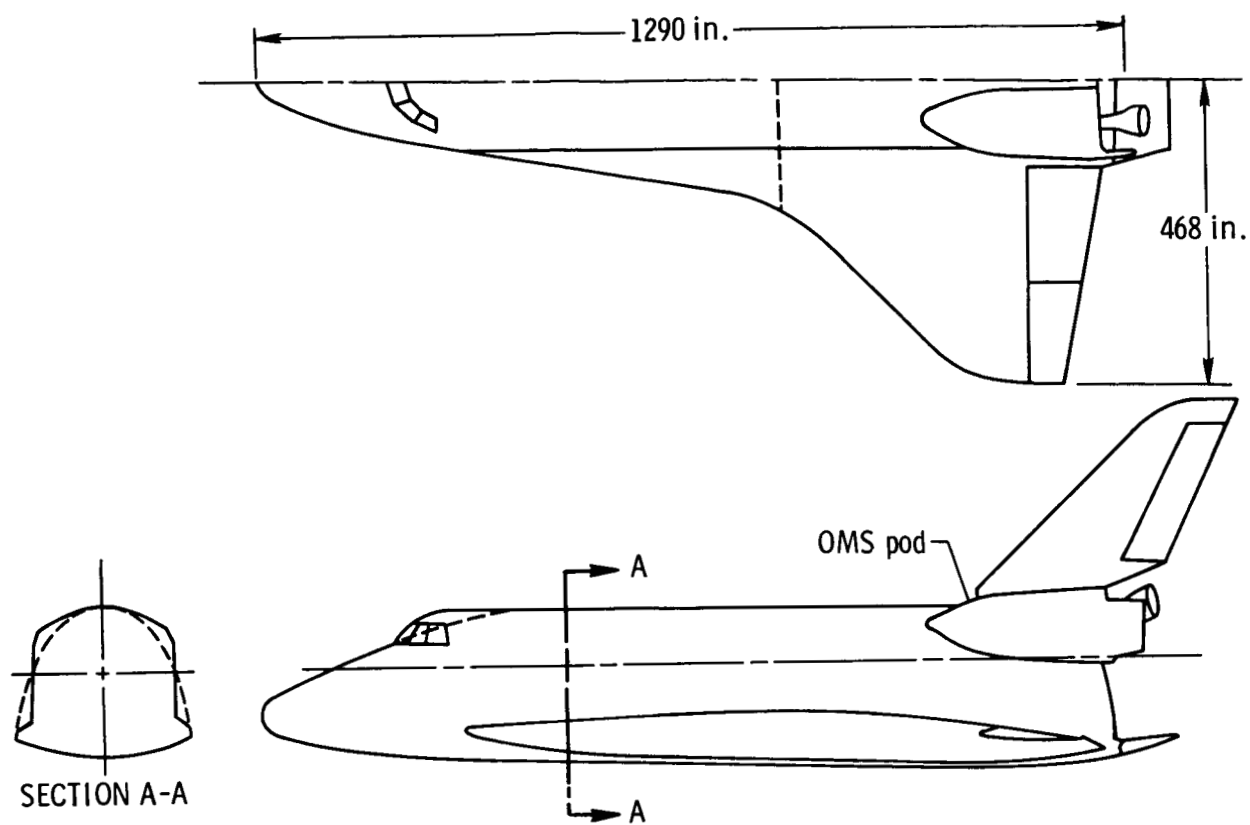
Figure 4.- Space Shuttle orbiter geometry.
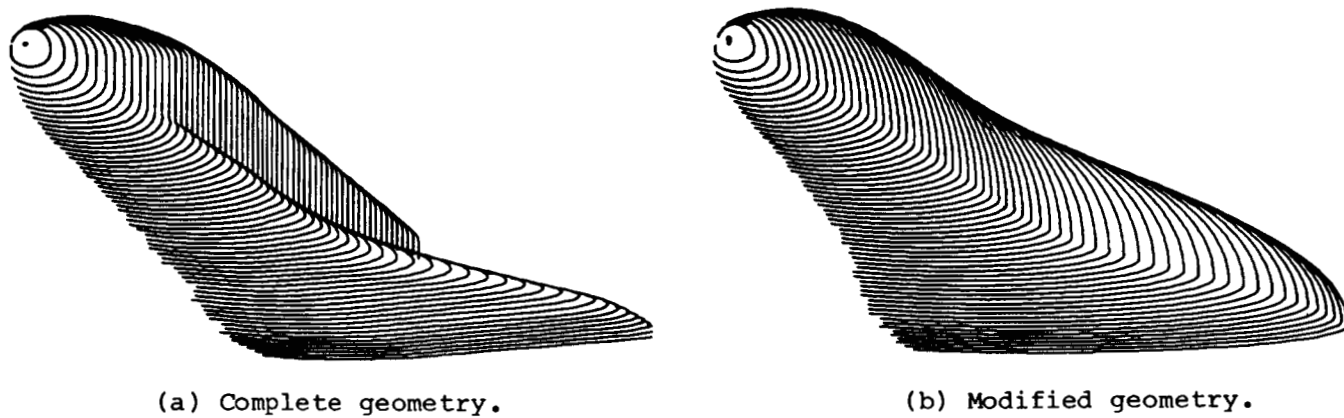
(a) Complete geometry.

(b) Modified geometry.

Figure 5.- QUICK geometry models.
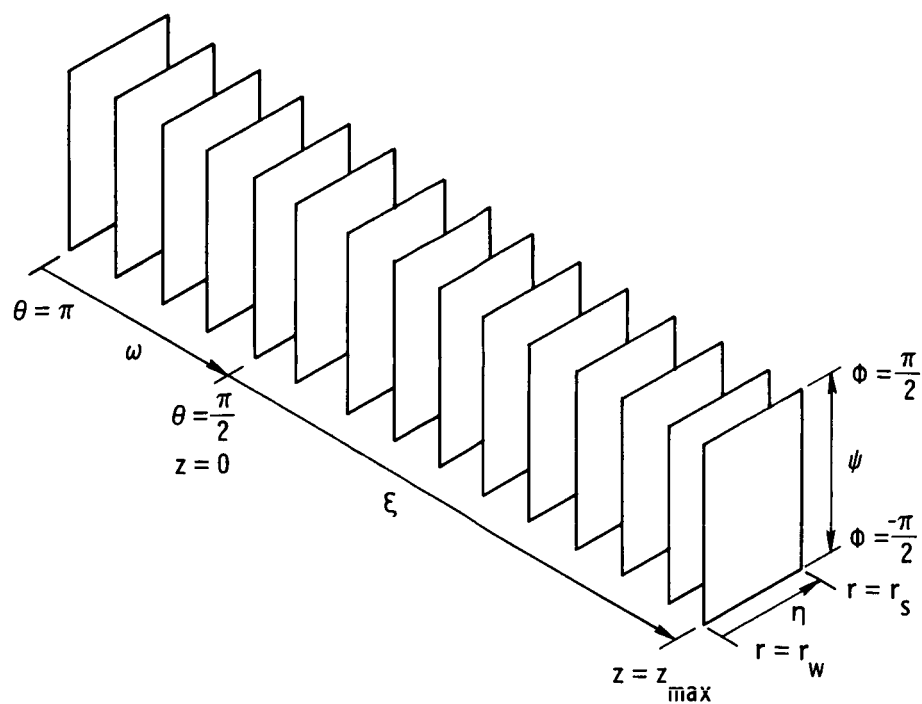
Figure 6.- Data-base configuration.
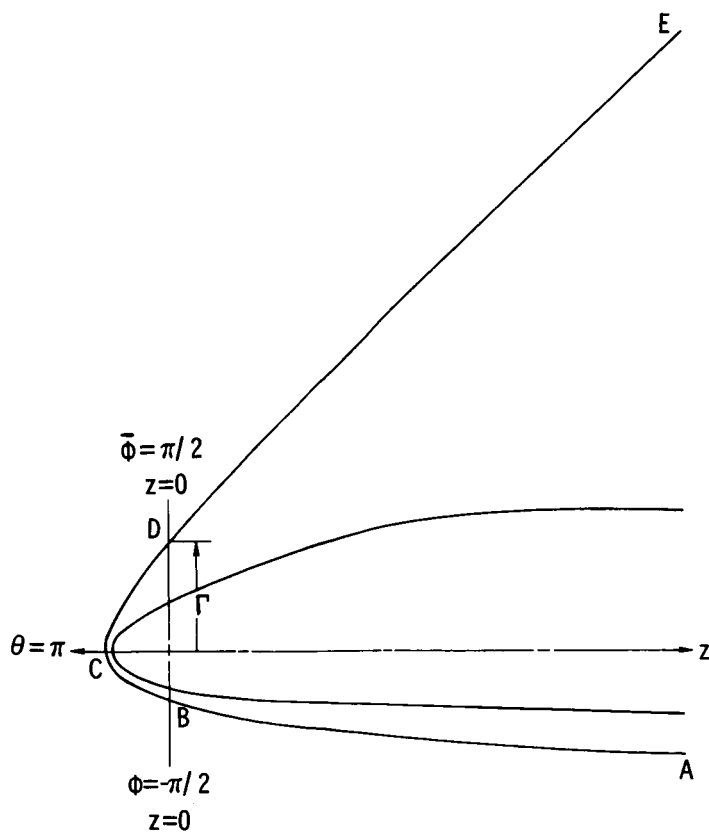
Figure 7.- Bow shock initializations. Symmetry plane.
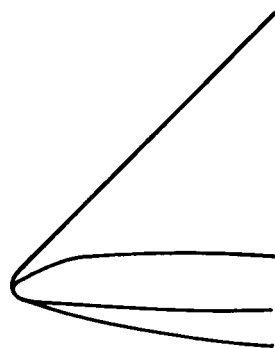
Profile view

Cross section at z = 50 in.
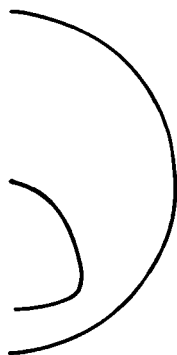
Cross section at z = 350 in.

Cross section at z = 650 in.

Figure 8.- Initial shock shapes. $M_\infty = 10.3$; $\alpha = 25°$.
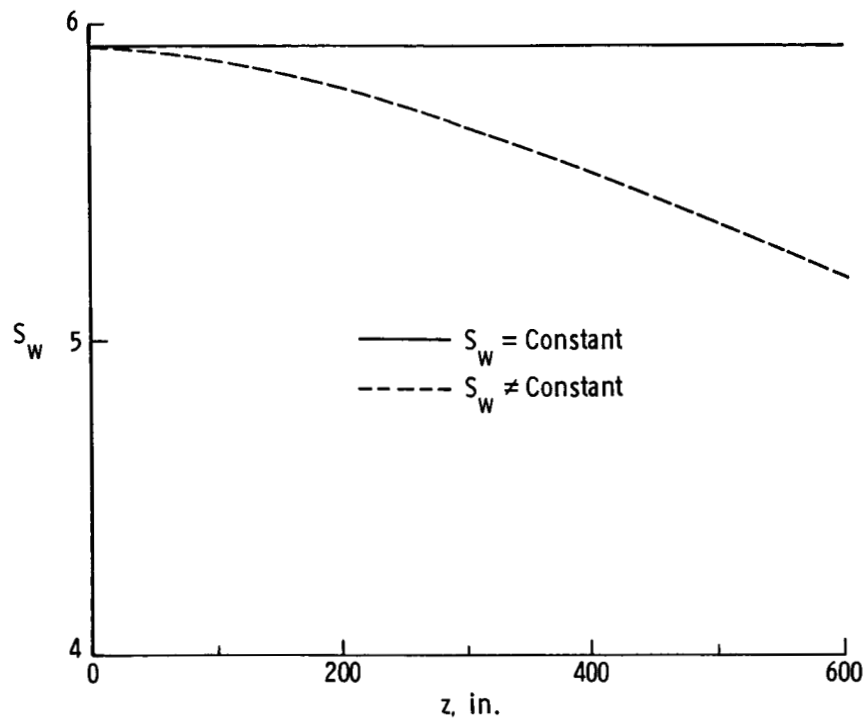
(a) Entropy distribution.
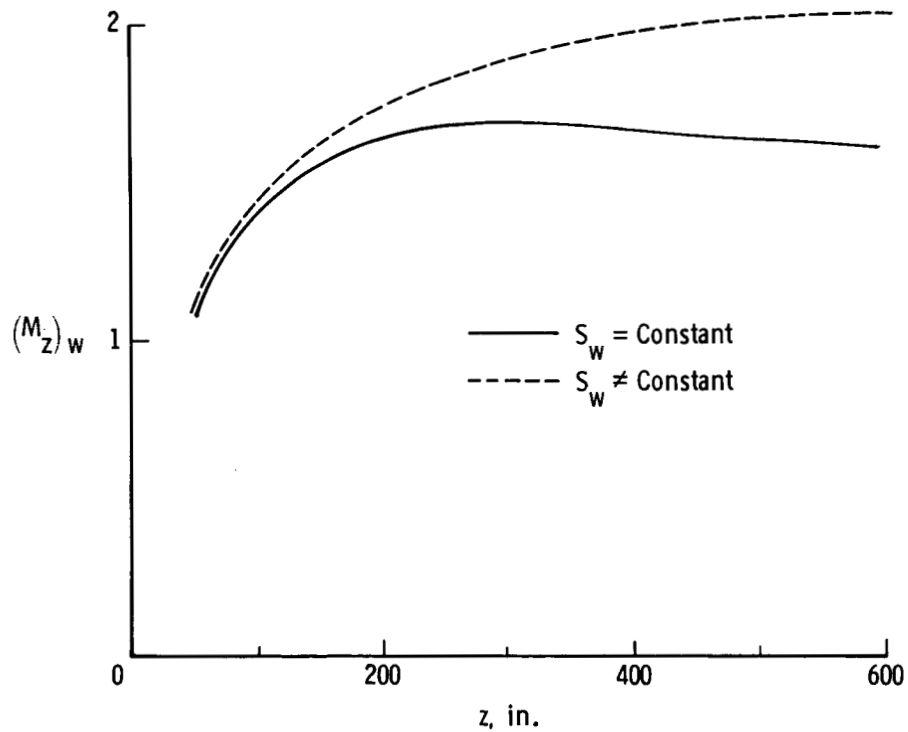
(b) Surface axial Mach number.

Figure 9.- Center-line surface distribution of flow variables as function of vehicle axial length for constant and variable entropy wall boundary conditions. $M_\infty = 10.3$; $\alpha = 25°$.
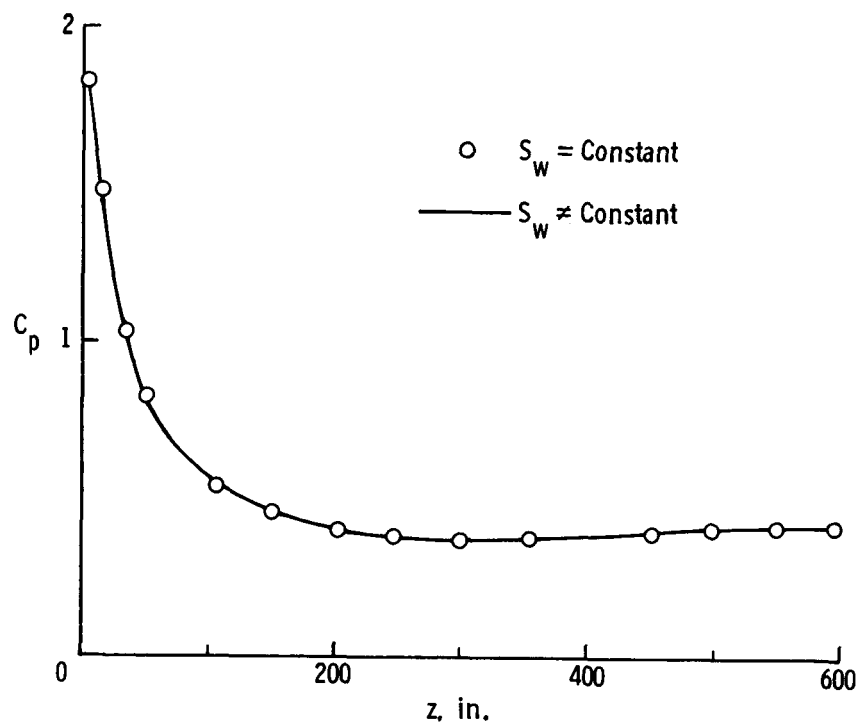
(c) Pressure coefficient.

Figure 9.- Concluded.
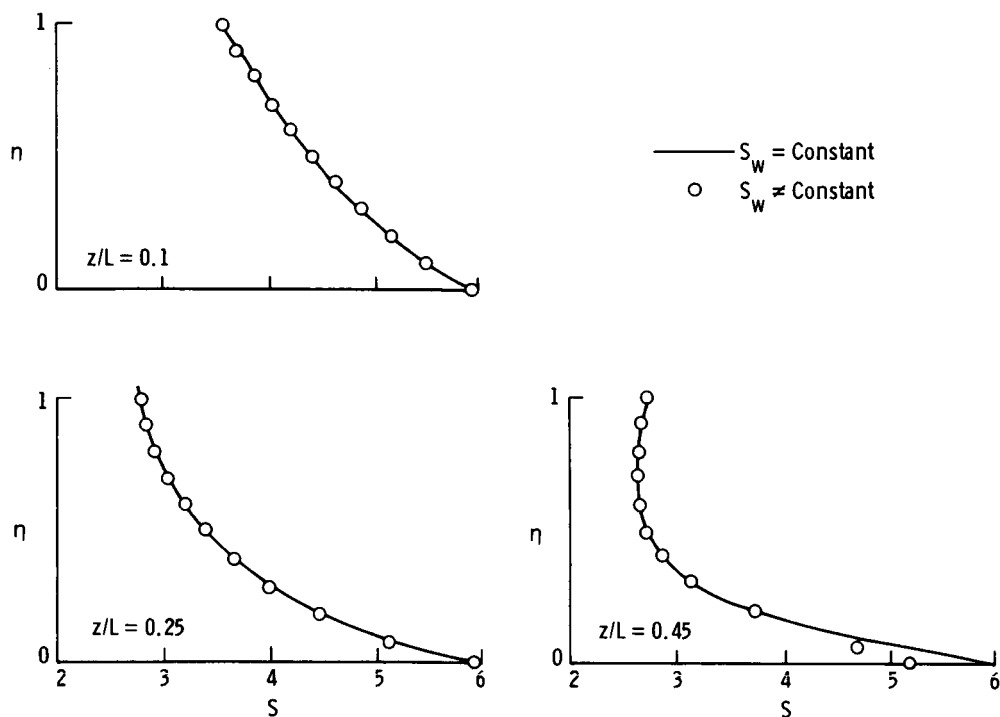
(a) Entropy distributions.
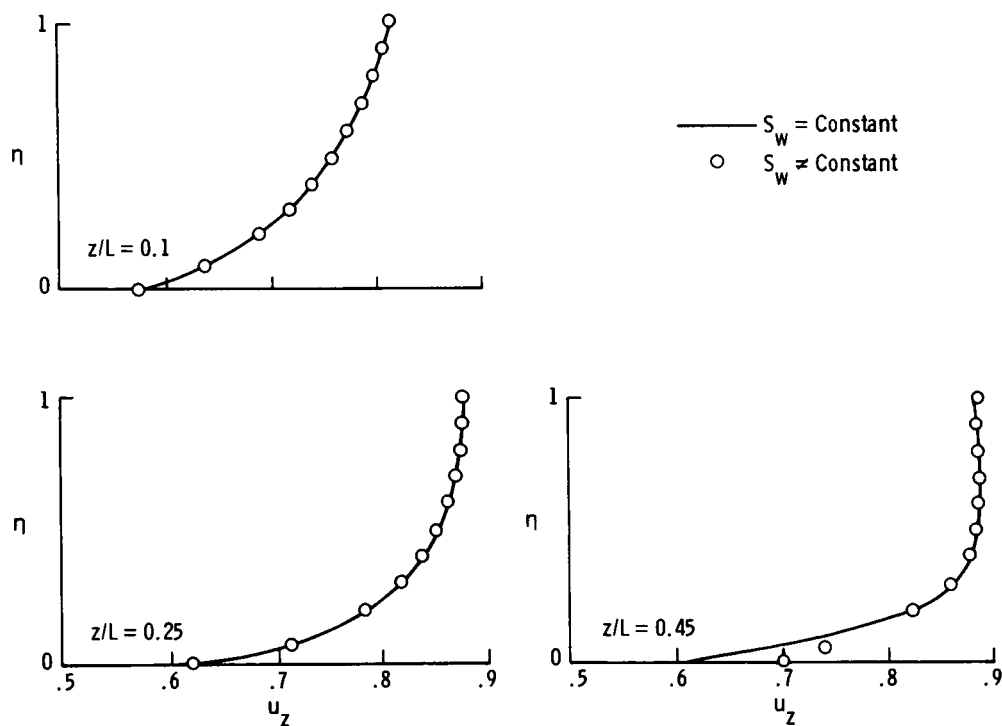
(b) Axial velocity distributions.

Figure 10.- Distribution of flow variables through shock layer in windward symmetry plane at axial locations z/L of 0.1, 0.25, and 0.45 for constant and variable entropy wall boundary conditions. $M_\infty = 10.3$; $\alpha = 25°$.
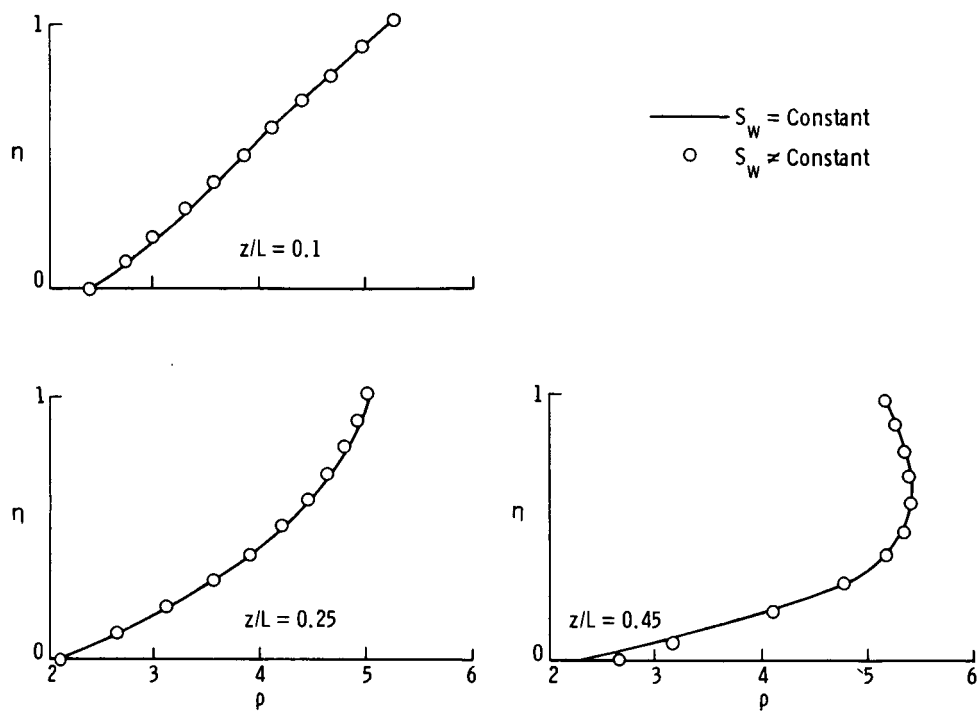
(c) Density distribution.
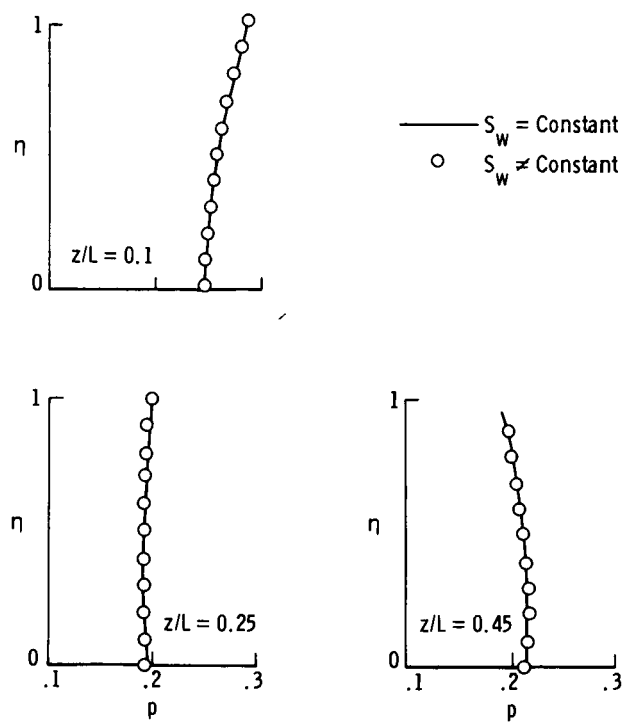
(d) Pressure distribution.

Figure 10.- Concluded.
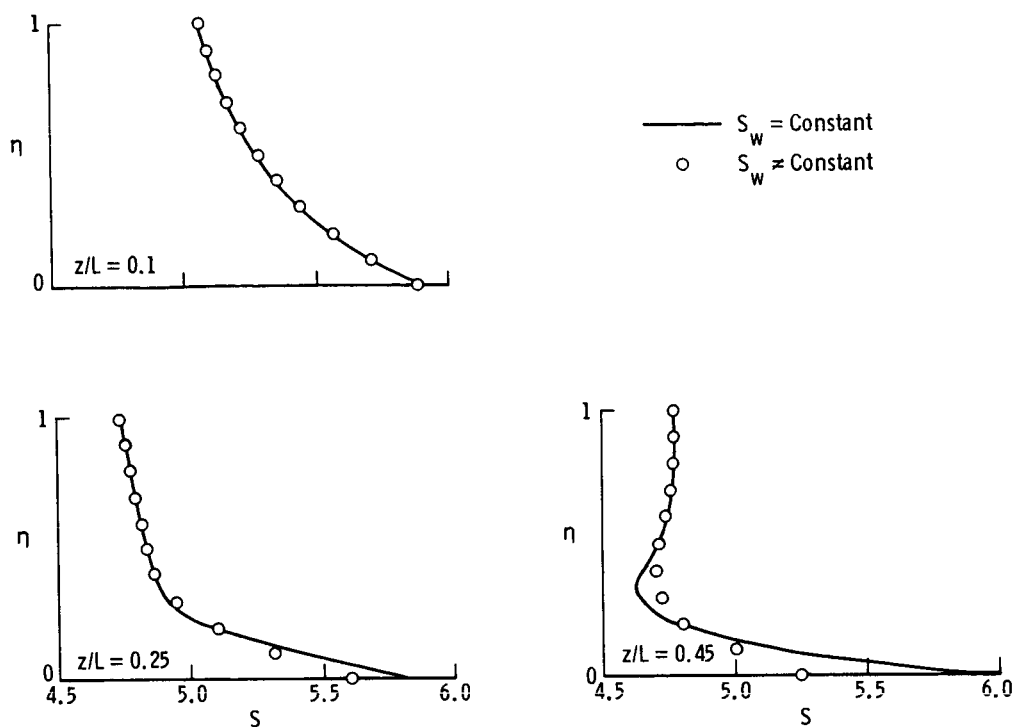
(a) Entropy distributions.
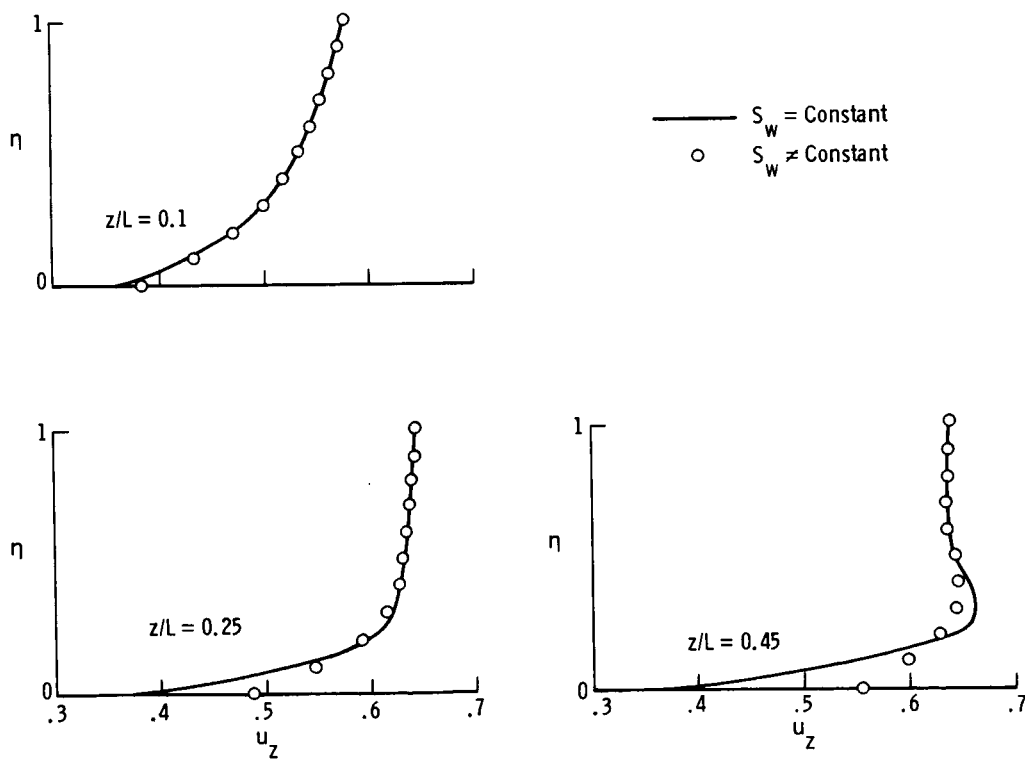
(b) Axial velocity distributions.

Figure 11.- Distribution of flow variables through shock layer in windward symmetry plane at axial locations z/L of 0.1, 0.25, and 0.45 for constant and variable wall boundary conditions. $M_\infty = 10.3$; $\alpha = 45°$.
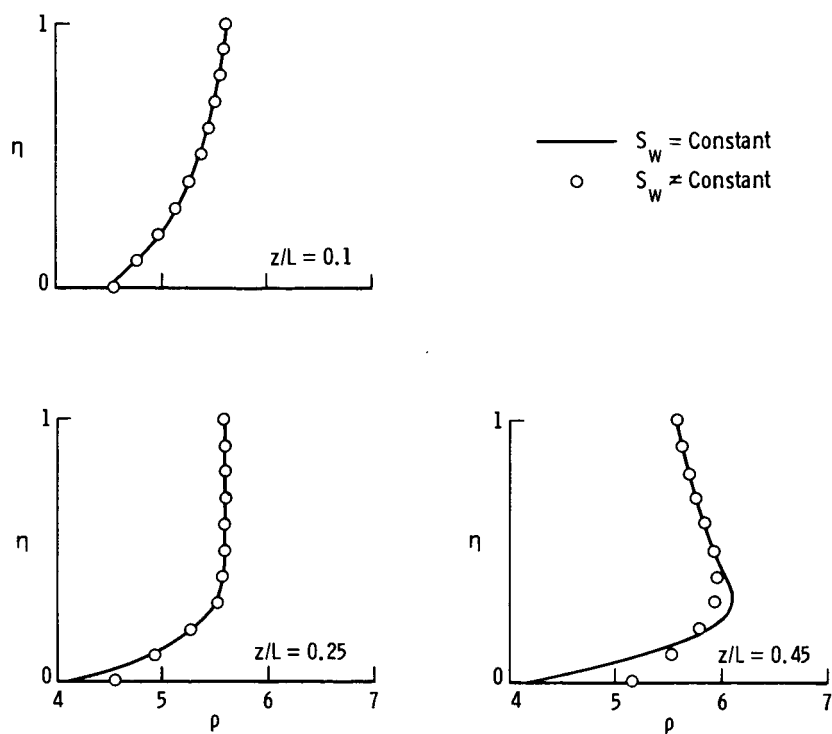
(c) Density distribution.
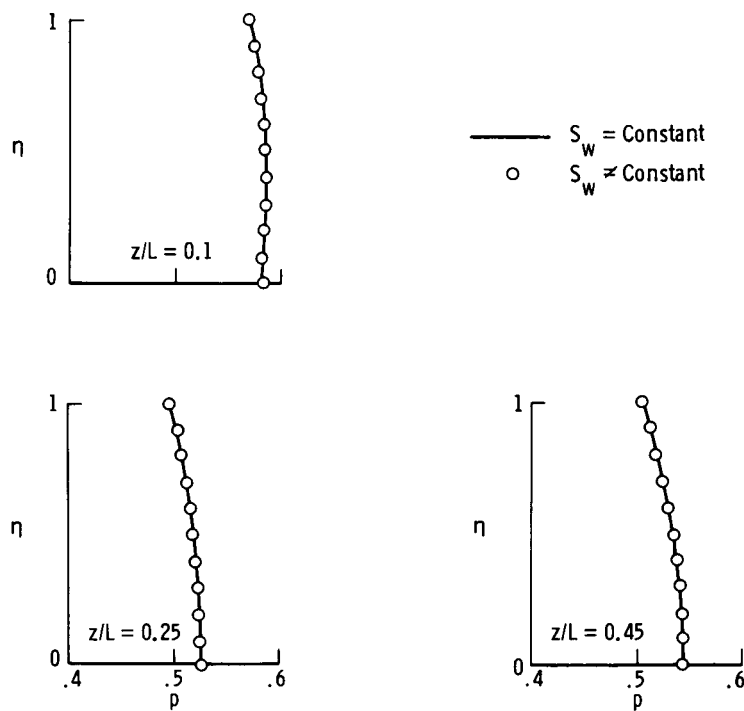
(d) Pressure distribution.

Figure 11.- Concluded.
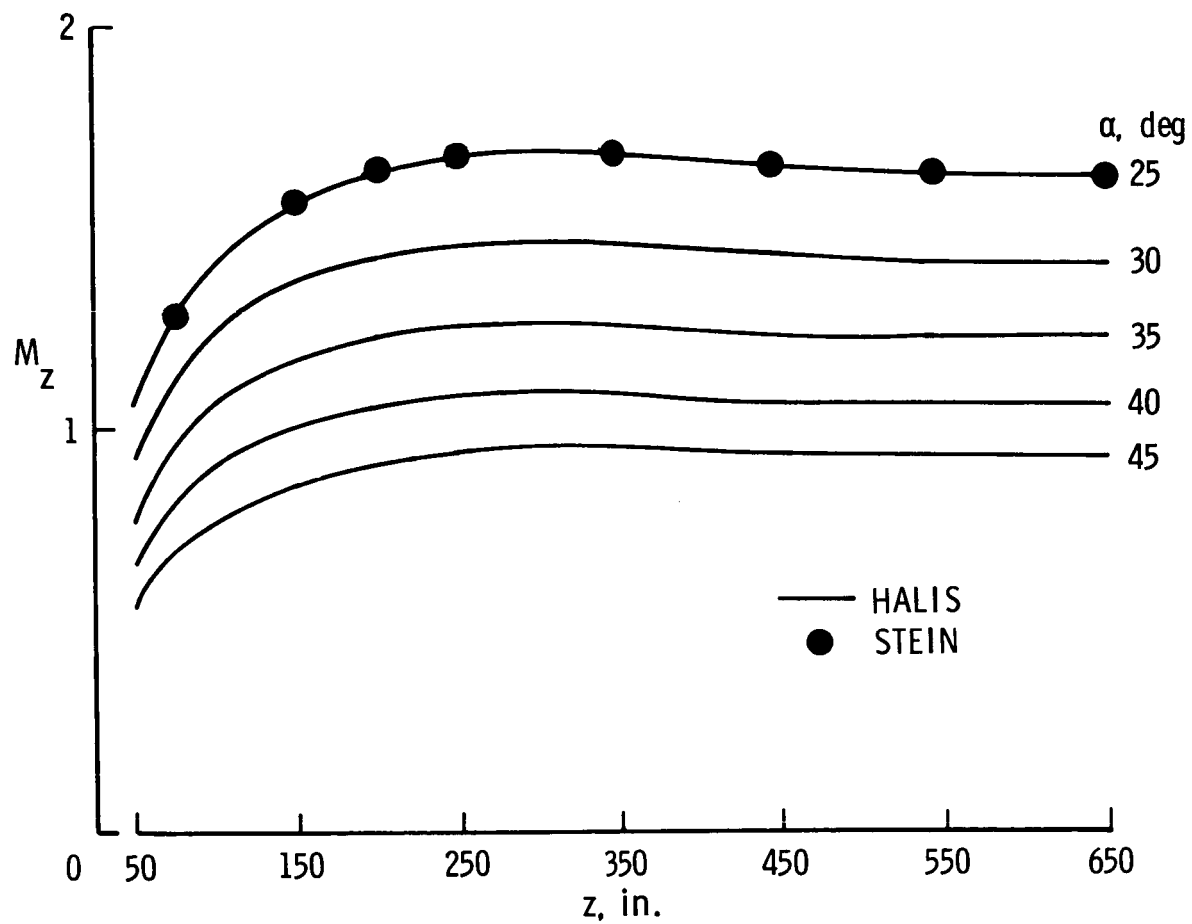
Figure 12.- Windward-surface center-line axial Mach number distribution. $M_\infty = 10.3$.
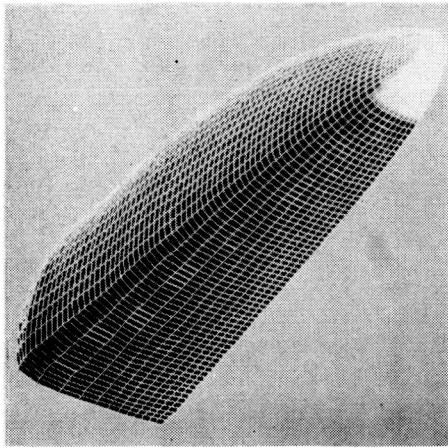
(a) $\alpha = 25°$.
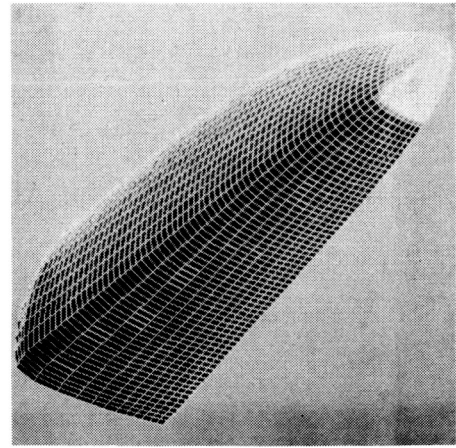
(b) $\alpha = 30°$.

(c) $\alpha = 35°$.

(d) $\alpha = 40°$.

(e) $\alpha = 42.5°$.

(f) $\alpha = 45°$.
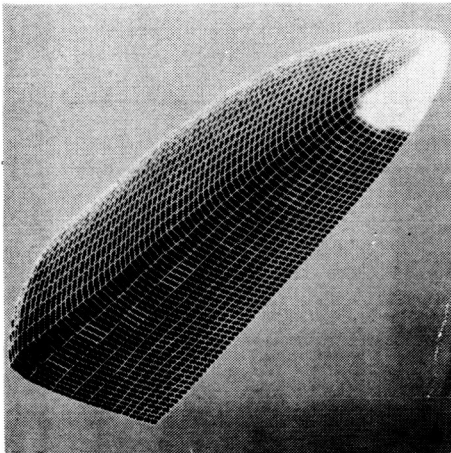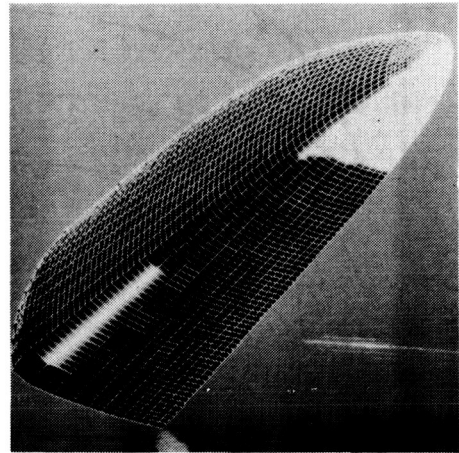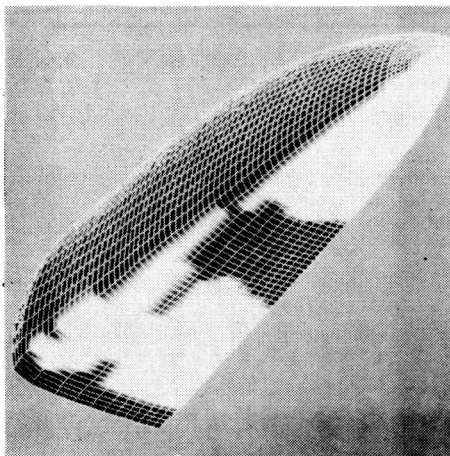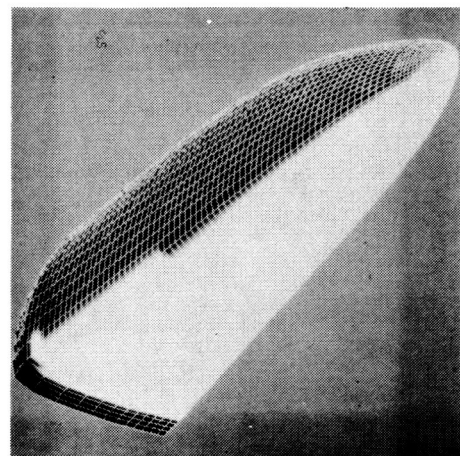
L-82-213

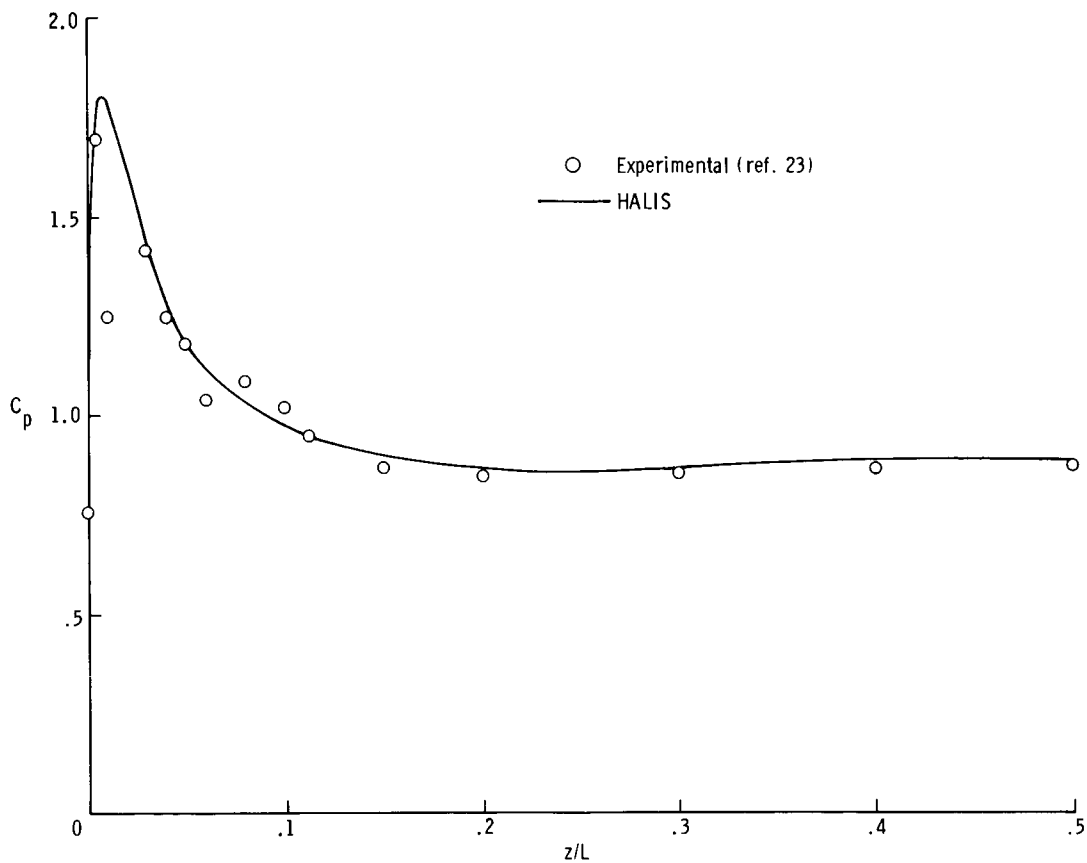Figure 13.- Surface axial Mach number distribution.
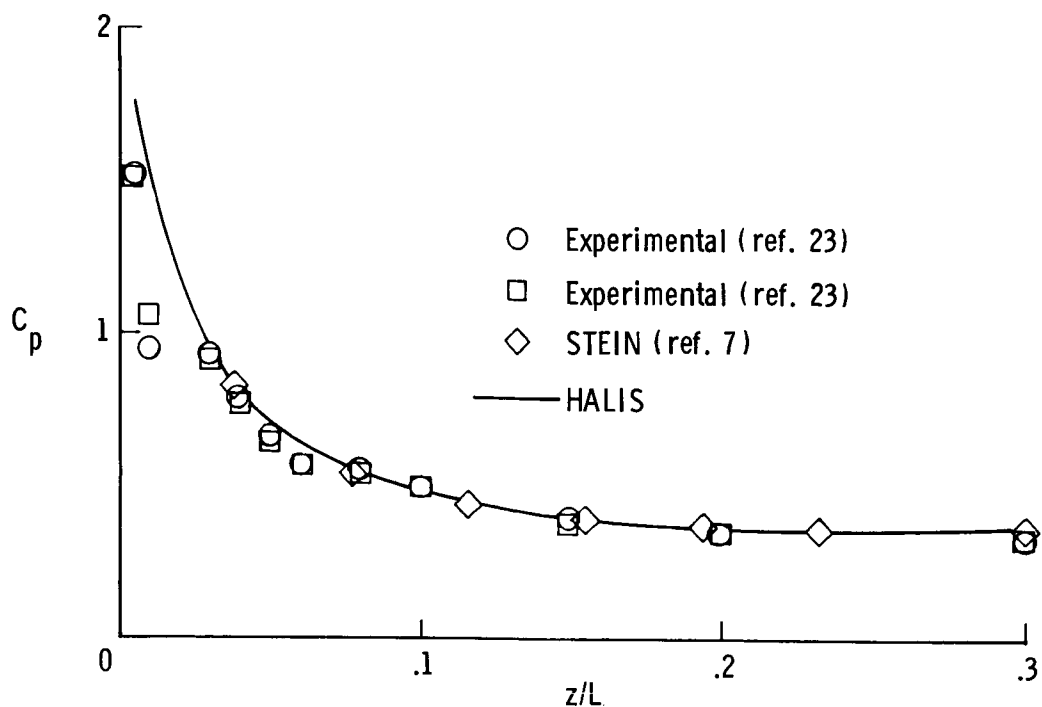
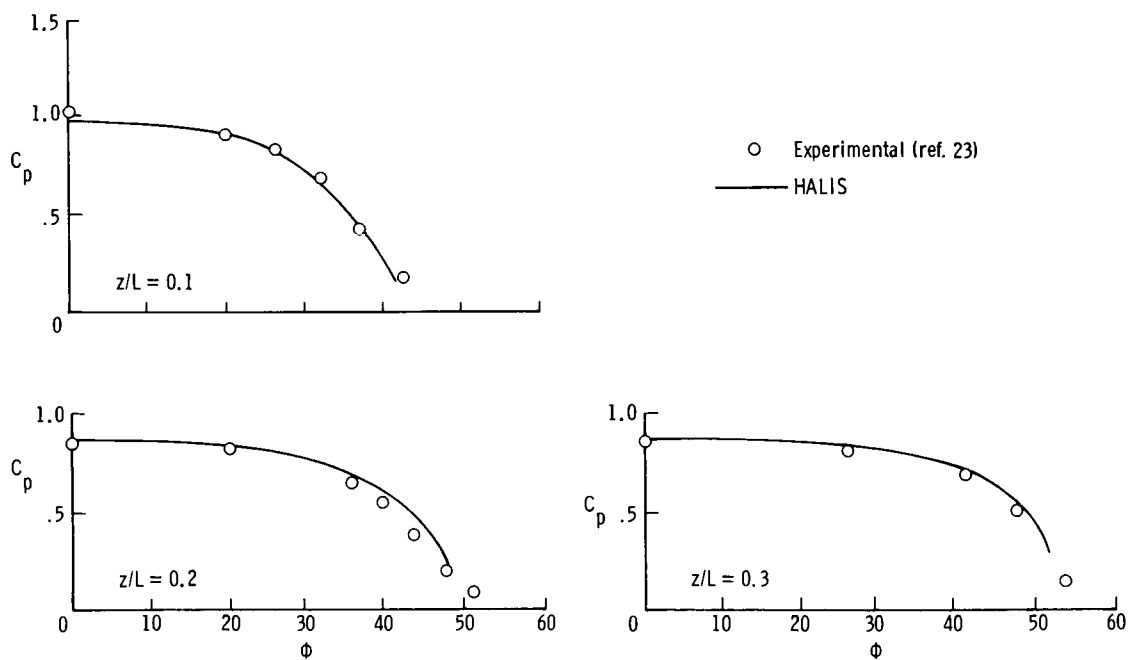(a) Windward center-line pressure coefficients.
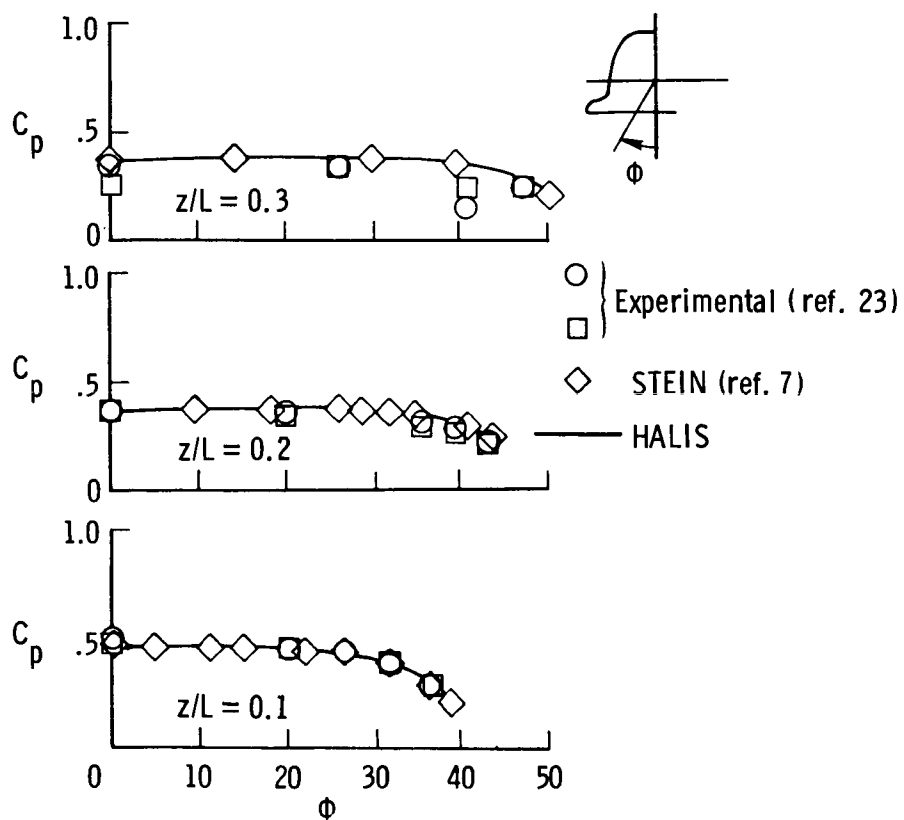
(b) Meridional pressure coefficients.

Figure 14.- Comparison of experimental and calculated pressure distributions at $M_\infty = 10.29$ and $\alpha = 25°$.
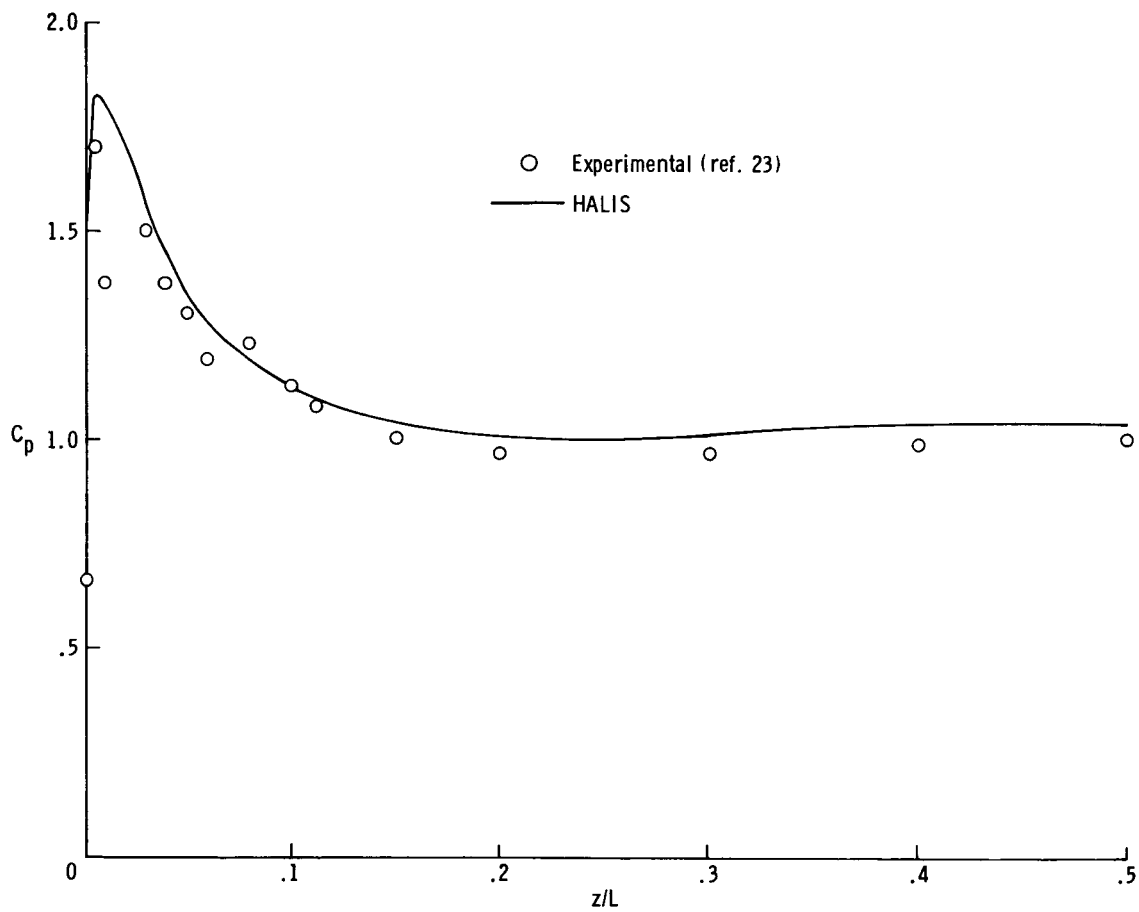
(a) Windward center-line pressure coefficients.

Figure 15.- Comparison of experimental and calculated pressure distributions at $M_\infty = 10.29$ and $\alpha = 30°$.
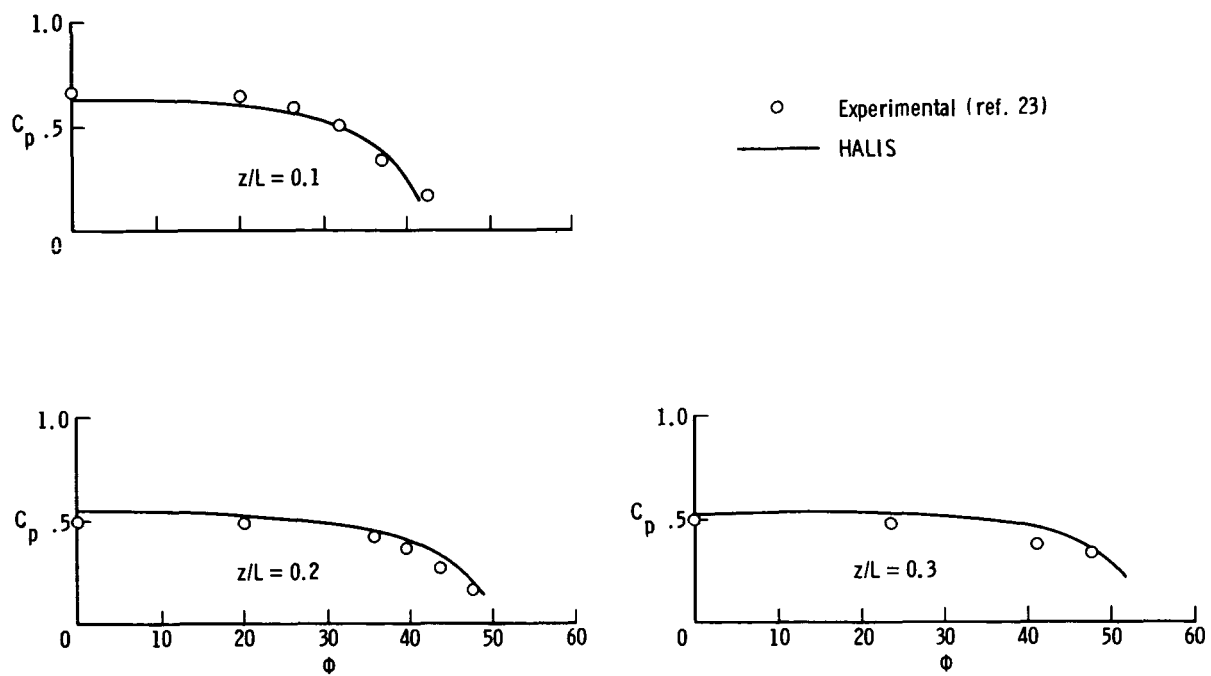
(b) Meridional pressure coefficients.
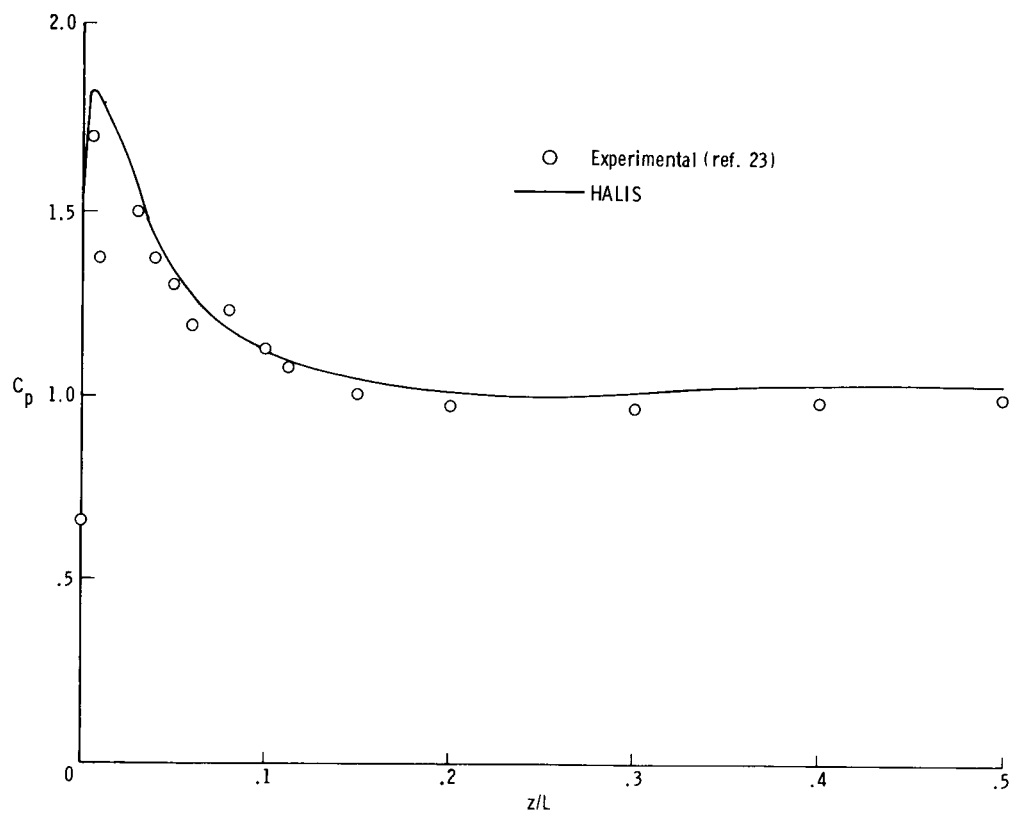
Figure 15.- Concluded.
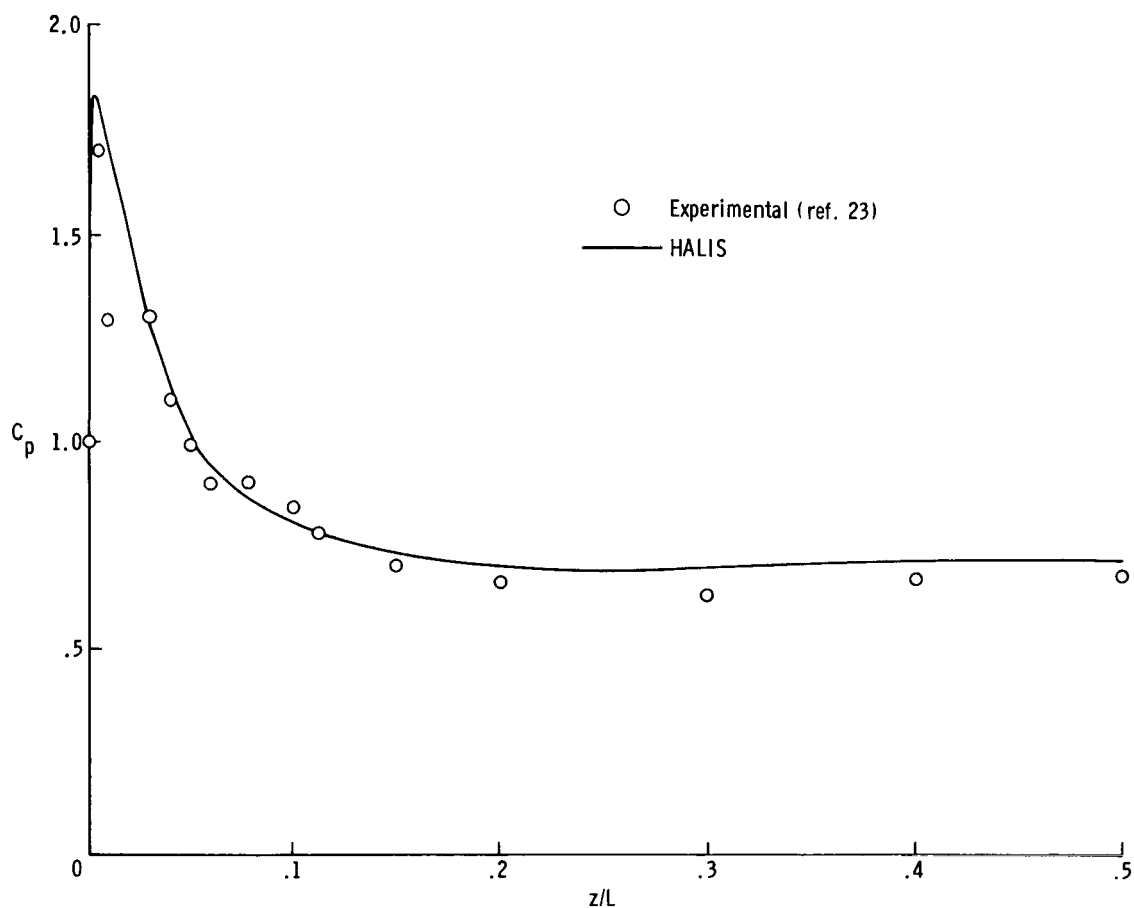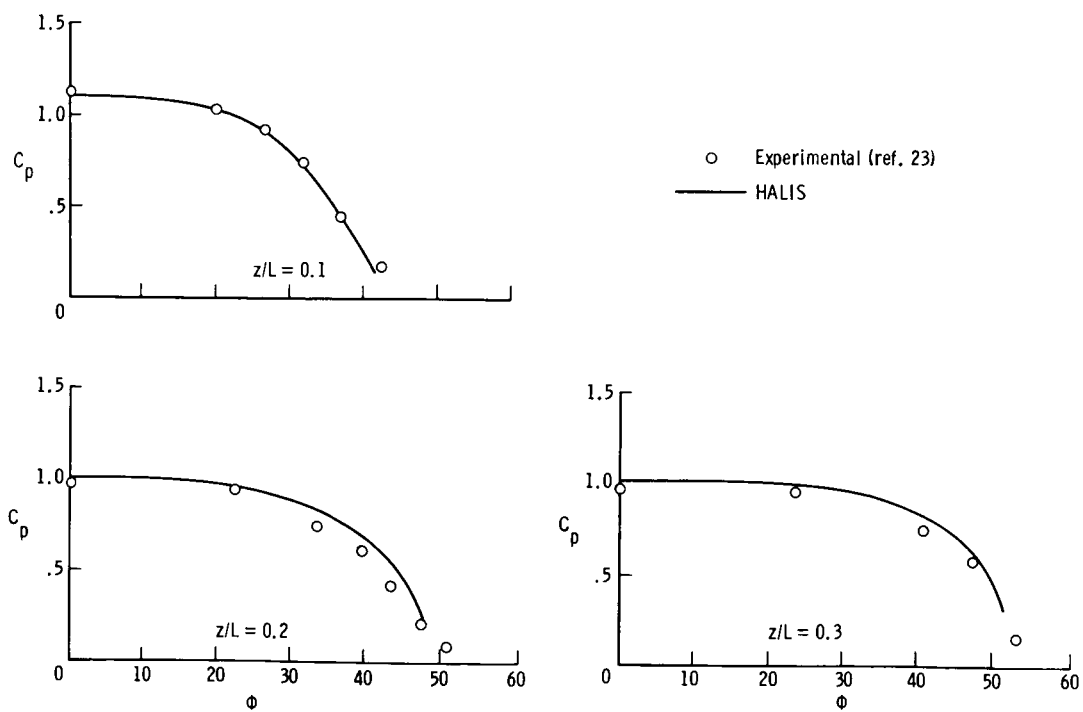
(a) Windward center-line pressure coefficients.
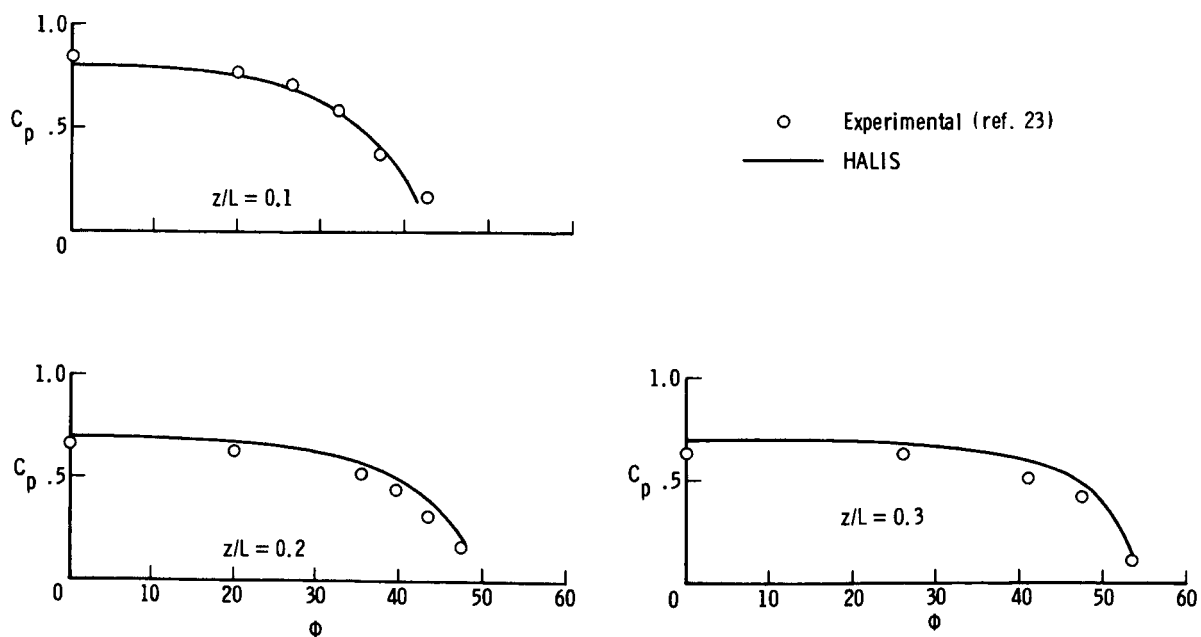
(b) Meridional pressure coefficients.

Figure 16.- Comparison of experimental and calculated pressure distributions at $M_\infty = 10.29$ and $\alpha = 35°$.

(a) Windward center-line pressure coefficients.

(b) Meridional pressure coefficients.

Figure 17.- Comparison of experimental and calculated pressure distributions at $M_\infty = 10.29$ and $\alpha = 40°$.

83

(a) Windward center-line pressure coefficients.

(b) Meridional pressure coefficients.

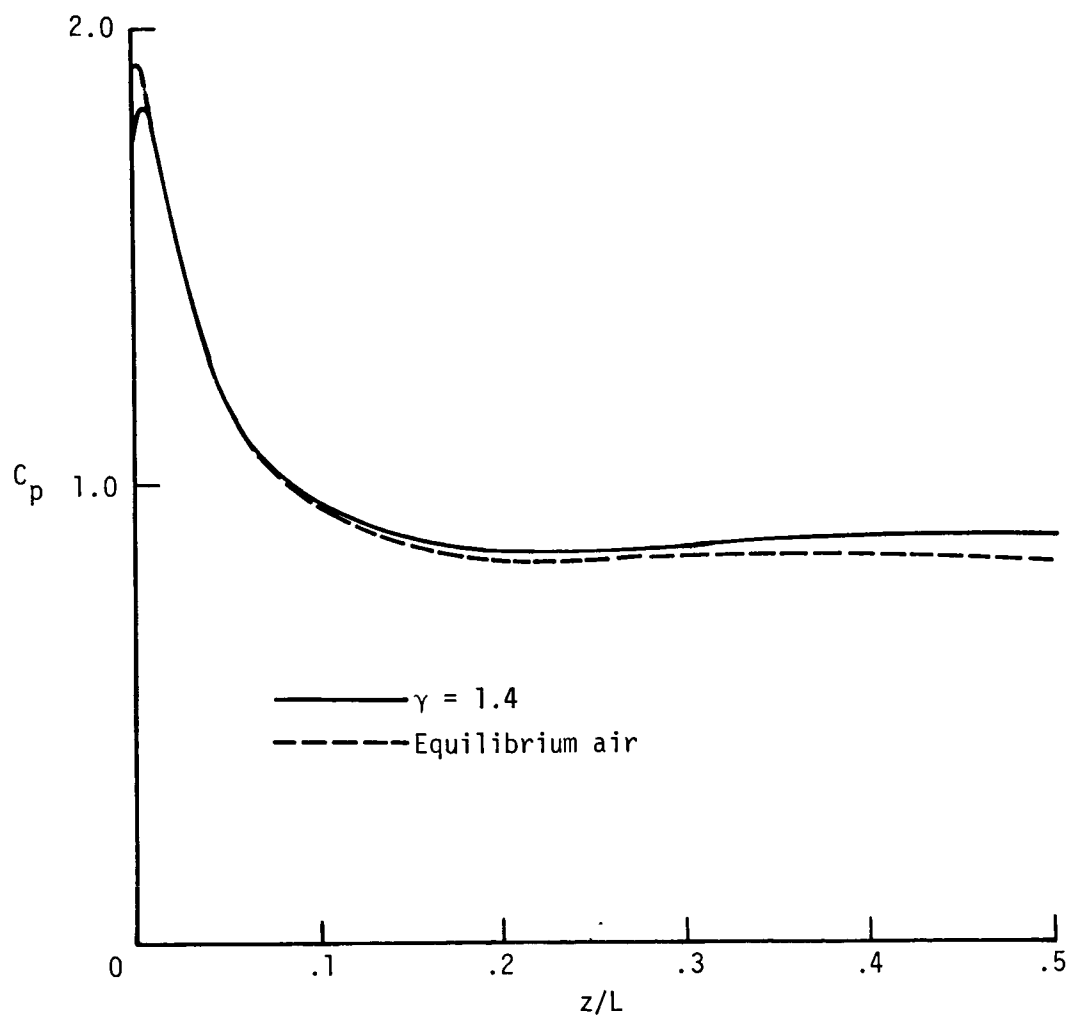Figure 18.- Comparison of experimental and calculated pressure distributions at $M_\infty = 10.29$ and $\alpha = 45°$.

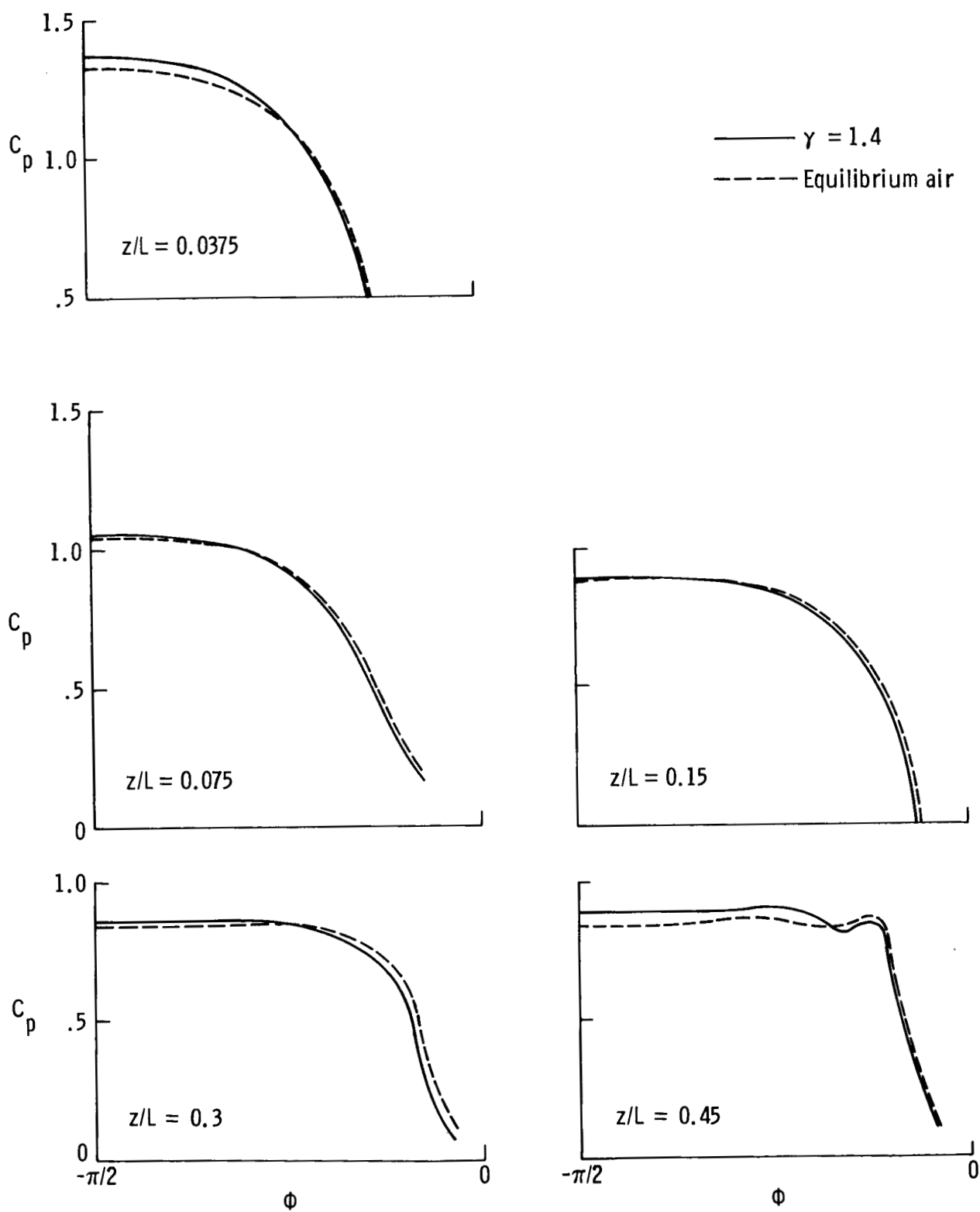Figure 19.- Windward center-line pressure coefficient distributions. $M_\infty = 18$; $\alpha = 40°$.

Figure 20.- Meridional pressure coefficient distributions. $M_\infty = 18$; $\alpha = 40°$.

1. Report No. NASA TP-2103	2. Government Accession No.	3. Recipient's Catalog No.
4. Title and Subtitle CALCULATIONS OF INVISCID FLOW OVER SHUTTLE-LIKE VEHICLES AT HIGH ANGLES OF ATTACK AND COMPARISONS WITH EXPERIMENTAL DATA		5. Report Date May 1983
		6. Performing Organization Code 506-51-13-03
7. Author(s) K. James Weilmuenster and H. Harris Hamilton II		8. Performing Organization Report No. L-15518
		10. Work Unit No.
9. Performing Organization Name and Address NASA Langley Research Center Hampton, VA 23665		11. Contract or Grant No.
		13. Type of Report and Period Covered Technical Paper
12. Sponsoring Agency Name and Address National Aeronautics and Space Administration Washington, DC 20546		
		14. Sponsoring Agency Code

15. Supplementary Notes

Appendix C by M. J. Hamilton, Sperry Systems Management, Hampton, Virginia.

16. Abstract

In this paper a computer code HALIS, designed to compute the three-dimensional flow about Shuttle-like configurations at angles of attack greater than 25°, has been described in detail. Results from HALIS have been compared where possible with an existing flow-field code; such comparisons have shown excellent agreement. Also, HALIS results have been compared with experimental pressure distributions on Shuttle models over a wide range of angle of attack. These comparisons have again been excellent. It has also been demonstrated that the HALIS code can incorporate equilibrium air chemistry in flow-field computations.

17. Key Words (Suggested by Author(s)) Computational fluid dynamics Supersonic flow High angle of attack Shuttle Three-dimensional inviscid flow	18. Distribution Statement Unclassified – Unlimited Subject Category 34

19. Security Classif. (of this report) Unclassified	20. Security Classif. (of this page) Unclassified	21. No. of Pages 89	22. Price A05